Integral-geometry morphological image analysis

Michielsen, K.F L; de Raedt, H.A.

Published in:
Physics Reports

DOI:
10.1016/S0370-1573(00)00106-X

Publication date:
2001

INTEGRAL-GEOMETRY MORPHOLOGICAL IMAGE ANALYSIS

K. MICHIELSEN[a], H. De RAEDT[b]

[a]Laboratory for Biophysical Chemistry, University of Groningen, Nijenborgh 4, 9747 AG Groningen, The Netherlands
[b]Institute for Theoretical Physics and Materials Science Centre, University of Groningen, Nijenborgh 4, 9747 AG Groningen, The Netherlands

ELSEVIER

AMSTERDAM – LONDON – NEW YORK – OXFORD – PARIS – SHANNON – TOKYO

ELSEVIER

Physics Reports 347 (2001) 461–538

PHYSICS REPORTS

www.elsevier.com/locate/physrep

Integral-geometry morphological image analysis

K. Michielsen[a], H. De Raedt[b,*]

[a]*Laboratory for Biophysical Chemistry, University of Groningen, Nijenborgh 4, 9747 AG Groningen, Netherlands*
[b]*Institute for Theoretical Physics and Materials Science Centre, University of Groningen, Nijenborgh 4, 9747 AG Groningen, Netherlands*

Received August 2000; editor: M.L. Klein

Contents

* Corresponding author. Tel.: + 31-50-363-4852; fax: + 31-50-363-4947.
E-mail addresses: kristel@phys.rug.nl (K. Michielsen), deraedt@phys.rug.nl (H. De Raedt).

PII: S0370-1573(00)00106-X

Abstract

This paper reviews a general method to characterize the morphology of two- and three-dimensional patterns in terms of geometrical and topological descriptors. Based on concepts of integral geometry, it involves the calculation of the Minkowski functionals of black-and-white images representing the patterns. The result of this approach is an objective, numerical characterization of a given pattern. We briefly review the basic elements of morphological image processing, a technique to transform images to patterns that are amenable to further morphological image analysis. The image processing technique is applied to electron microscope images of nano-ceramic particles and metal-oxide precipitates. The emphasis of this review is on the practical aspects of the integral-geometry-based morphological image analysis but we discuss its mathematical foundations as well. Applications to simple lattice structures, triply periodic minimal surfaces, and the Klein bottle serve to illustrate the basic steps of the approach. More advanced applications include random point sets, percolation and complex structures found in block copolymers.

PACS: 07.05.Pj

Keywords: Morphology; Euler characteristic; Integral geometry; Minkowski functionals; Electron microscopy; Mesostructures; Polymers; Morphological image processing

1. Introduction

Geometrical patterns are encountered in many different fields of science and technology [1,2]. Very often these patterns come in the form of pictures. In general, the purpose of image analysis is to find out what is in these pictures [3–6]. Describing this information in words is one extreme form of characterizing the image, another extreme form is to assign one or more numbers to the image. In this paper we only consider the latter.

In this paper, we will analyze two-dimensional (2D) and three-dimensional (3D) patterns by numerical represention of the corresponding images in terms of two-valued functions. Therefore, a numerical characterization of features in the image requires that the image has been digitized, i.e. that the image has been converted to numerical form [3–6]. This conversion may include additional digital image processing steps [3–6] to enhance the quality of the images. If the image contains color or gray-level information, the digitization process should include the mapping of the spatial and color/brightness information in the image onto a collection of black-and-white picture elements [3–6]. For simplicity, we will use the term *pixel* to refer to both 2D and 3D picture elements.

Numerical functions on the set of black-and-white images are called *image functionals* [7]. An image functional performs a measurement of certain properties or features in the image, such as the brightness, or location of objects, their surface, perimeter, size distribution, etc. An example of an image functional φ is the area of black pixels on a background of white pixels. If P_1 and P_2 are two patterns of black pixels we obviously have

$$\varphi(P_1 \cup P_2) = \varphi(P_1) + \varphi(P_2) - \varphi(P_1 \cap P_2) \; . \tag{1}$$

The last term in (1) compensates for the double counting of black pixels that are common to P_1 and P_2. Image functionals that share property (1) are called *additive*. Intuitively, it may seem obvious to require image functionals to be additive: In general, one would like to avoid counting a feature in an image more than once. However, in image analysis there is no fundamental reason to stick to additive image functionals. In fact, there is a large collection of non-additive image functionals that yield useful information on specific features of an image [3]. For instance, the two-point correlation function of the positions of the black pixels (i.e. the Fourier transform of the structure factor) is a non-additive functional but it certainly yields very useful information about the spatial distribution of the black pixels.

Morphology is a branch of biology dealing with the form and structure of animals and plants. The same word is used for the study of the geometry and topology of patterns. *Integral-geometry morphological image analysis* (MIA for short from now on) employs additive image functionals to assign numbers to the shape and connectivity of patterns formed by the pixels in the image. Integral geometry [8–10] provides the rigorous mathematical framework to define these image functionals. A fundamental theorem (discussed below) of integral geometry [8] states that under certain conditions, the number of different additive image functionals is equal to the dimension of the pattern plus one. Thus, in the case of a 2D (3D) image there are exactly 3 (4) of these functionals, called quermassintegrals or Minkowski functionals. For a given image the first step in MIA is to compute these functionals themselves. The second step is to study the behavior of the three or four numbers as a function of some control parameters, such as time, density, etc.

A remarkable feature of MIA is the big contrast between the simplicity of implemention and use and the level of sophistication of the mathematical theory. Indeed, as explained below, the

calculation of the image functionals merely amounts to the proper counting of, e.g. faces, edges and vertices of pixels. The application of MIA requires little computational effort. Another appealing feature of MIA is that the image functionals have a geometrically and topologically intuitive and hence perceptually clear interpretation: For 2D images they correspond to the area, boundary length, and connectivity number. The four functionals for 3D images are the volume, surface area, integral mean curvature and connectivity number.

This paper gives an overview of the various aspects of MIA, with an emphasis on the practical application. MIA has proven to be very useful to describe the morphology of porous media and complex fluids [11–14], the large-scale distribution of matter in the Universe [14–16], regional seismicity realizations [17], quantum motion in billiards [18], microemulsions [14,19], patterns in reaction–diffusion systems [14,20], spinodal decomposition kinetics [14,21,22], and the dewetting structure in liquid crystal and liquid metal films [23], and in polymer films [24]. In many cases additional information can be extracted from the pattern by making assumptions about size, shape and distribution of the objects. Usually, this involves making a probabilistic model of the pattern and comparing the Minkowski functionals of the model with those of the images. Applications of this stochastic-geometry approach to model natural phenomena can be found in [10].

The paper is structured as follows. Section 2 gives a brief introduction to MIA in practice (including examples of computer code), for those who want to start right away. Section 3 gives a brief introduction to morphological image processing (MIP), a digital image processing technique to enhance the quality of images while preserving the morphological content of the images as much as possible. In Section 4 we present some examples of MIP applied to scanning electron microscopy images of nano-ceramics. The mathematical framework on which MIA is based is reviewed in Section 5. In Section 6 we illustrate how MIA works in practice, using well-known point patterns and geometrical objects. Section 7 discusses the application of MIA to random point sets and percolation. In Section 8 we use MIA to analyze various structures found in block copolymers. A summary is given in Section 9.

2. Quick start

In this section we give a brief overview of MIA. Thereby we focus on the practical aspects. For the sake of brevity we omit most mathematical justification, references to relevant work, and discussions of examples. These can be found in the sections that follow. We only consider the analysis of black-and-white images. Extensions are discussed below.

In the next two subsections we describe a simple and efficient procedure to compute the image functionals for a given image. The following two subsections focus on the second step of MIA: The study of the dependence of these functionals on some control parameters. In the last subsection we give an alternative interpretation of the Minkowski functionals in terms of correlation functions of Ising spins.

2.1. Computation of the image functionals

Consider a 2D lattice filled with black pixels on a white background (see Fig. 1). For simplicity, we will assume that the pixels are squares and that the linear size of each square has been

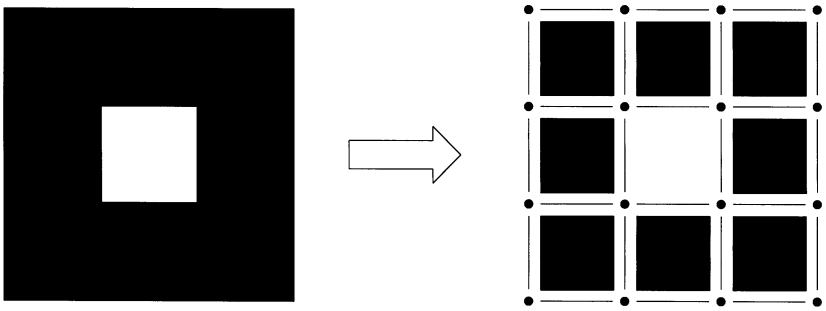

Fig. 1. Decomposition of the pixels of a two-dimensional black-and-white pattern (left) into squares, edges and vertices (right). For this example: number of squares $n_s = 8$, number of edges $n_e = 24$ and number of vertices $n_v = 16$.

normalized to one. We want to characterize the geometry and topology of the pattern formed by the black pixels. According to integral geometry, there are three additive image functionals, called Minkowski functionals, that describe the morphological content of this 2D pattern, namely the area A, the perimeter U and the Euler characteristic χ. The latter describes the connectivity (topology) of the pattern: In 2D χ equals the number of regions of connected black pixels minus the number of completely enclosed regions of white pixels. Two black pixels are "connected" if and only if they are nearest neighbors or next-nearest neighbors of each other or can be connected by a chain of black pixels that are nearest and/or next-nearest neighbors. Using this definition we find that the Euler characteristic of the pattern shown in Fig. 1 is zero.

Conceptually, the procedure (that easily extends to three dimensions) to compute these three numbers consists of two steps. First, we decompose each black pixel into 4 vertices, 4 edges and the interior of the pixel (see Fig. 1). Then we count the total number of squares n_s, edges n_e and vertices n_v and we compute the area A, perimeter U and Euler characteristic χ from

$$A = n_s, \quad U = -4n_s + 2n_e, \quad \chi = n_s - n_e + n_v \ . \tag{2}$$

For the example shown in Fig. 1 we find $A = 8$, $U = 16$ and $\chi = 0$.

For a 3D cubic lattice filled with black and white pixels (we do not distinguish between voxels and pixels) the four additive image functionals (Minkowski functionals) are the volume V, the surface area S, the mean breadth B (see Section 5), and the Euler characteristic χ. In 3D χ equals the number of regions of connected black pixels plus the number of completely enclosed regions of white pixels minus the number of tunnels, i.e. regions of white pixels piercing regions of connected black pixels. As in the 2D case, the first step in the calculation of these four numbers is to consider each black pixel as the union of 8 vertices, 12 edges, 6 faces and the interior of the cube. It can be shown that

$$V = n_c, \quad S = -6n_c + 2n_f, \quad 2B = 3n_c - 2n_f + n_e, \quad \chi = -n_c + n_f - n_e + n_v \ , \tag{3}$$

where n_c and n_f are the number of cubes and faces, respectively. Thus, as in the 2D case, the morphological characterization of a 3D pattern reduces to the counting of the elementary geometrical objects (vertices, edges, faces, cubes) that constitute the pattern.

2.2. Computer program

Technically, the only real "problem" with the procedure described above is to avoid counting, e.g. an edge or vertex more than once. However this problem is easily solved, as illustrated by the algorithm we will briefly discuss now.

In Appendix A we list a computer program to compute A, U and χ (V, S, B, χ) for a 2D (3D) black-and-white pattern. We discuss the 2D case only because the 3D program only differs in the details. Conceptually, what these programs do is to build up the whole image using vertices, edges, etc. In practice, this is accomplished by adding active (=black in the example above) pixels to an initially empty (=white in the example above) image (held in array tmp($\cdot$)) one by one. Just before adding the active pixel to the current image (in tmp($\cdot$)) subroutine "minko_2D_free" determines the change in A, U and χ that would result if this pixel is actually added to the current image. This change is calculated by first decomposing this square pixel as discussed above and then checking whether, e.g. an edge overlaps with an edge of another active pixel in the current image. Then the pixel is made active in the current image and the changes are added to the current values of A, U and χ. Inspection of "minko_2D_free" shows that all it does is check to see if the pixel-to-be-added has active nearest neighbors and/or next-nearest neighbors and count the number of edges and vertices accordingly. Clearly, the number of arithmetic operations required to compute A, U and χ (or V, S, B and χ) scales linearly with the number of black pixels of the image. Thus the numerical procedure is efficient.

Some applications, notably those where the patterns are the result of computer simulation, make use of periodic boundary conditions. There is no need to adapt the programs given in Appendix A to deal with this situation. One can embed the original image into a larger one, formed by surrounding the original image by one extra layer of pixels, the value of which is determined by making use of the periodic boundary conditions.

2.3. Point patterns

Many systems observed in nature may be modeled by point patterns. For example, a system of particles may be viewed as a collection of points defined by the position of the particles. These points are usually called the *germs* of the model [10,25]. In order to study the morphological properties of the set of points (degree of randomness, clustering, periodic ordering, etc.) it is useful to attach to the points discs (spheres) of radius r. Those discs (spheres) are called the *grains* of the model [10,25]. The study of the coverage of the image by the grains gives information about the distribution of the germs.

Mapping the point pattern onto a square (cubic) lattice yields a black-and-white picture. Black pixels represent the germs of the model. On the pixel lattice we can construct the grains of the model in two different ways. In the first method we consider the germs to be discs (spheres) of radius $r = 0$. We enlarge the discs (spheres) by making black all pixels that are positioned at a distance smaller or equal to $r > 0$ from the germs. The grains form discrete approximations to discs (spheres) in the Euclidean space. An example of this graining procedure in two dimensions is shown on the left-hand side of Fig. 2 for grains of radius $r = 3$. The right-hand side of Fig. 2 illustrates the second graining procedure (for $d = 2$), where we take the germs to be squares (cubes) of edge length $r = 1$ and the grains to be enlarged squares (cubes) of edge length $2r + 1, r > 0$. Note

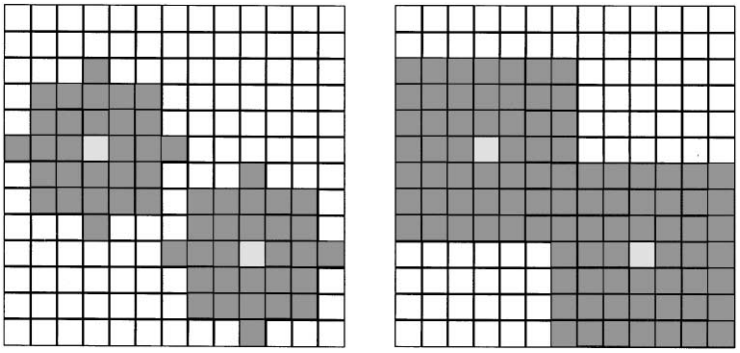

Fig. 2. Graining procedure of a point pattern in two dimensions. Left: the grains are discrete approximations to a sphere with radius three in the Euclidean space. Right: the grains are squares of edge length seven. The light grey pixels indicate the positions of the germs.

that the growing of the cubic grains leads to a faster complete coverage of the image than the growing of the circular grains. In the following, the cubic grains will be used for special cases only (see Section 7).

For this type of problem MIA consists of the calculation of the three (four) numbers A, U and χ (V, S, B and χ) as a function of the grain size r. A schematic representation of this procedure for the case of 2D point patterns is shown in Fig. 3.

2.4. Digitized and thresholded images

In general, the intensity (or gray level) in experimental images may be thought of as a continuous function of the position in the image. In order to analyze such images by computer we first have to digitize them [3–6]. The digitization process requires the mapping of the image on a grid and a quantization of the gray level. Usually, 2D (3D) images are partitioned into square (cubic) regions. Each square (cube) is centered at a lattice point, corresponding to a pixel. In general, the range of gray levels is divided into intervals and the gray level at any lattice point is required to take only one of these values.

The output of image analysis should be a description of the given picture. Thus, we have to define the various objects building up the picture, i.e. we need a method to distinguish objects from the background [3,6]. The simplest method of reducing gray-scale images to two-valued images or black-and-white pictures is to make use of a *threshold*. If the given picture $\mathscr{P}(\boldsymbol{x})$ with $\boldsymbol{x} \in \mathbb{R}^d$ has gray level range $[a, b]$, and q is any number between a and b, the result of thresholding $\mathscr{P}(\boldsymbol{x}, q)$ at q is the two-valued picture $\mathscr{P}(\boldsymbol{x}, q)$ defined by [3–6]

$$\mathscr{P}(\boldsymbol{x}, q) = \begin{cases} 1, & \mathscr{P}(\boldsymbol{x}) \geq q \ , \\ 0, & \mathscr{P}(\boldsymbol{x}) < q \ . \end{cases} \tag{4}$$

By definition if $\mathscr{P}(\boldsymbol{x}, q) = 0$, $\boldsymbol{x}$ is part of the background, and if $\mathscr{P}(\boldsymbol{x}, q) = 1$, $\boldsymbol{x}$ is part of an object. In practice not all thresholds q yield useful $\mathscr{P}(\boldsymbol{x}, q)$. If q is too large too many objects are classified as

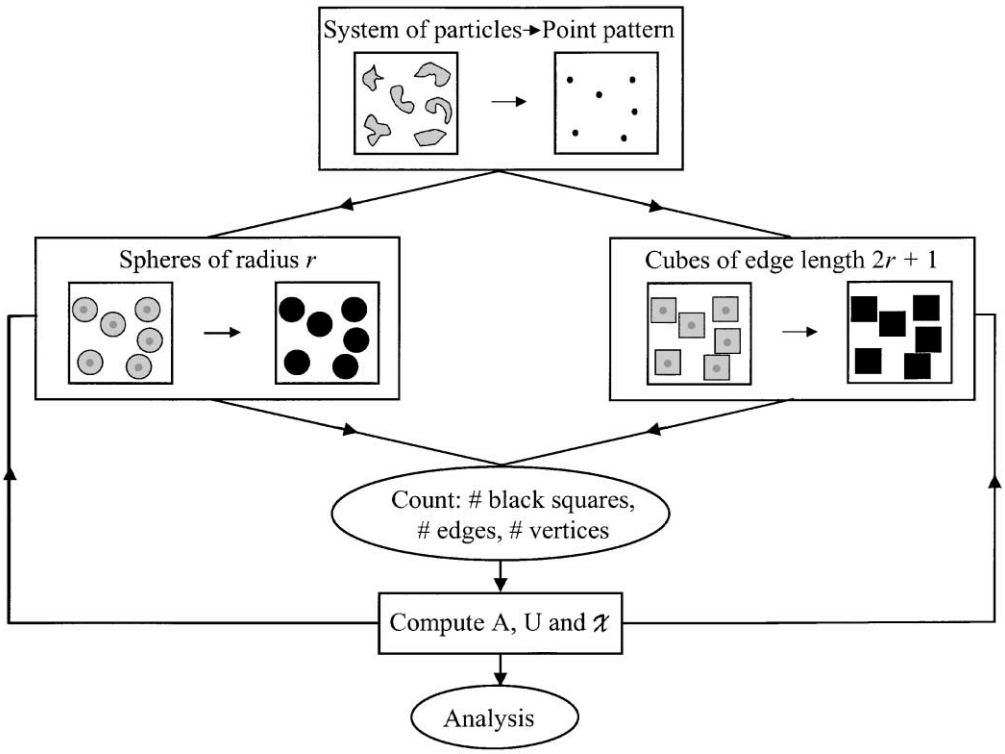

Fig. 3. Schematic representation of how to use MIA to analyze the morphological properties of (patterns that can be interpreted in terms of) 2D point patterns.

background or if q is too small the opposite happens. Other thresholding operations may also be considered [3–6].

For this type of problem MIA consists of the calculation of the three (four) numbers A, U and χ (V, S, B and χ) as a function of the threshold q. A schematic representation of this procedure for the case of 2D gray-scale images is shown in Fig. 4.

2.5. Minkowski functionals and Ising spins

It is instructive to represent black-and-white images as a set of Ising spins and to express the Minkowski functionals in these variables. This exercise is useful for two purposes. First, it shows that in certain cases, Minkowski functionals have a direct physical interpretation and second it gives insight into the kind of correlations of pixels the Minkowski functionals actually measure. We restrict ourselves to the 2D case, the extension to 3D is trivial.

The standard procedure to map a black-and-white picture onto a lattice of Ising spins is to assign a spin $\sigma_{i,j} = +1(-1)$ to the black (white) pixel at lattice position (i,j). Starting from the

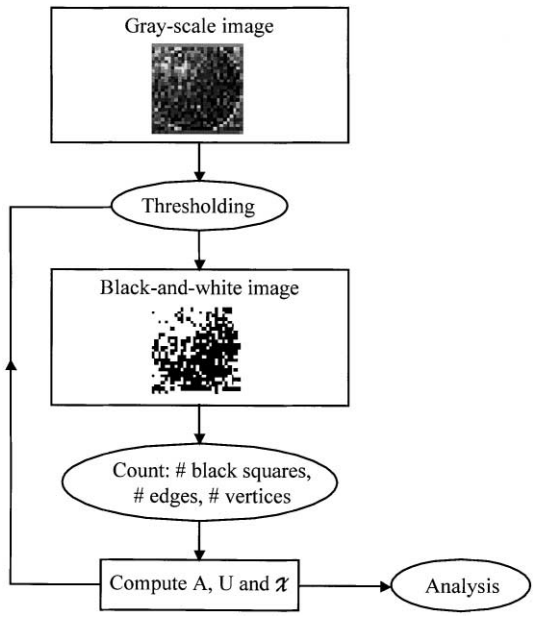

Fig. 4. Schematic representation of how to use MIA to analyze the morphological properties of 2D digitized images.

expressions given in Appendix B, a straightforward calculation gives

$$A = \frac{L_x L_y}{2} + \frac{1}{2}\sum_{i=1}^{L_x}\sum_{j=1}^{L_y}\sigma_{i,j}\ , \tag{5a}$$

$$U = L_x L_y - \frac{1}{2}\sum_{i=1}^{L_x}\sum_{j=1}^{L_y}\sigma_{i,j}(\sigma_{i+1,j}+\sigma_{i,j+1})\ , \tag{5b}$$

$$\begin{aligned}\chi = & -\frac{L_x L_y}{16} - \frac{1}{4}\sum_{i=1}^{L_x}\sum_{j=1}^{L_y}\sigma_{i,j} + \frac{1}{8}\sum_{i=1}^{L_x}\sum_{j=1}^{L_y}\sigma_{i,j}(\sigma_{i+1,j}+\sigma_{i,j+1})\\ & - \frac{1}{16}\sum_{i=1}^{L_x}\sum_{j=1}^{L_y}\sigma_{i,j}(\sigma_{i+1,j+1}+\sigma_{i+1,j-1})\\ & + \frac{1}{16}\sum_{i=1}^{L_x}\sum_{j=1}^{L_y}\sigma_{i,j}(\sigma_{i+1,j}+\sigma_{i,j+1})\sigma_{i+1,j+1}\\ & + \frac{1}{16}\sum_{i=1}^{L_x}\sum_{j=1}^{L_y}\sigma_{i,j+1}\sigma_{i+1,j}(\sigma_{i,j}+\sigma_{i+1,j+1})\\ & - \frac{1}{16}\sum_{i=1}^{L_x}\sum_{j=1}^{L_y}\sigma_{i,j}\sigma_{i+1,j}\sigma_{i+1,j+1}\sigma_{i,j+1}\ ,\end{aligned} \tag{5c}$$

where (L_x, L_y) denote the number of lattice sites in the (x, y)-direction. Readers familiar with the Ising model recognize immediately that up to irrelevant constants, the area A and perimeter U correspond to the magnetization and energy of the Ising model with nearest-neighbor

interactions. The Euler characteristic is a weighted sum of all possible correlations of up to four neighboring spins. Furthermore, it is clear that the Minkowski functionals (A, U and χ) and the two-spin correlation function (or structure factor)

$$S(k,l) = \frac{1}{L_x L_y} \sum_{i=1}^{L_x} \sum_{j=1}^{L_y} \sigma_{i,j}\sigma_{i+k,j+l} \tag{6}$$

perform different, hence complementary measurements on the configuration of spins (or pixels).

3. Morphological image processing

In the preceding section we took for granted that the digitized images are free of noise and other artifacts that may affect the geometry and topology of the structures of interest. Such perfect images are easily generated by computer and are very useful for the development of theoretical concepts and models (see e.g. Sections 6 and 7). Unfortunately, as we all know, genuine pictures or patterns obtained from computer simulations (e.g. a polymer solution, see Section 8) are all but perfect. Therefore, some form of image processing may be necessary before attempting to make measurements of the features in the image.

Digital image processing is very important for many industrial, medical and scientific applications. There is a vast amount of literature on this subject so we can only cite a few books here [3–6]. There is also a huge number of different processing steps and methods. The type of measurements that will be performed on the image is an important factor in making a selection of the most appropriate processing steps.

In morphological image analysis the geometric and topological content of the image are of prime importance and this should be reflected in the operations that are used to enhance the image quality. The morphological image processing (MIP) technique reviewed below is well adapted for this purpose. This is because MIP and MIA are based on the same mathematical concepts (see below). Most importantly it is flexible, fast and easy to use. Pioneering work in this field was carried out by Matheron [25] and Serra [26]. We have found the book of Giardina and Dougherty [7] a very valuable source of information and inspiration. Most of the material of Sections 3.1–3.3 can be found in [7], albeit in different form. We have chosen to present the material in the same order as MIP is actually performed: From a gray scale to a black-and-white image. The emphasis is on the practical application, much less on the mathematical foundations which are given in [7,25,26].

3.1. Preliminaries

In this section we introduce the basic concepts of MIP. We start by giving a more precise definition of an image. For simplicity, we will discuss MIP of 2D images only. Extension to 3D is trivial, also in practice. As usual a 2D image will be represented by an $L_x \times L_y$ array $I(i,j)$ of gray values, intensities represented by integers, L_x (L_y) is the number of pixels in the x (y) direction. We will see below that some operations may refer to pixels that are out of bounds of this array, meaning that they refer to pixels that are not defined. It is convenient to assign the value minus

infinity to such pixels [7]. Hence, we will write $I(i,j) = -\infty$ whenever the pixel at (i,j) (within or outside the bounds of the array) is undefined.

The structuring element or template is a key concept in MIP. A template is a predetermined geometrical structure, hence also an image, such as a square, a disc or star. Consistency of notation would suggest the use of the symbol $T(i,j)$ to denote the image corresponding to the template T but we will not do so. Instead we define a *template* by specifying the displacement $\langle k,l\rangle_T$ relative to its origin $(0,0)$ together with the value $T(k,l)$. The *size of a template* is defined as $\max\{|k|,|l|\}$. A template cannot contain pixels that are undefined. Some examples of templates are shown in Fig. 5. Very often templates are chosen to be symmetric (with respect to the symmetry operations of a square lattice). In essence MIP is the study of how a template (or several templates) fit into an image [7,25,26]. A template represents the viewer's a priori knowledge or expectation about the morphological content of the image.

Finally, we need a definition of an object. For reasons of consistency with the integral geometry approach discussed below an *object* is defined as a collection of pixels that satisfy the following criteria: (i) they all have the same intensity, and (ii) they are nearest neighbors or next-nearest neighbors of each other or can be connected by a chain of pixels that are nearest and/or next-nearest neighbors.

It may seem strange that it is necessary to include next-nearest neighbors in counting objects but in fact it is not. This can already be seen by looking at a very simple example: A pattern that consists of two squares that touch each other at the vertex yield an Euler characteristic of one (one connected component), since $n_s = 2$, $n_e = 8$ and $n_v = 7$ (see (1)). Clearly, there are no holes in this pattern. Hence the number of objects must be equal to the Euler characteristic (recall, for 2D patterns the Euler characteristic is equal to the number of connected components, i.e. objects, minus the number of holes, see Section 2). The only way to get a consistent procedure of counting objects and computing the Euler characteristic is to include next-nearest neighbors.

3.2. Gray-scale images

We now have all the ingredients to define the two basic MIP operations: Dilation and erosion of an image. *Dilation* $\mathscr{D}$ transforms an input image $I(i,j)$ as follows:

$$\mathscr{D}(I,T)(i,j) \equiv \max_{\langle k,l\rangle_T} [I(i-k,j-l) + T(k,l)] \,. \tag{7}$$

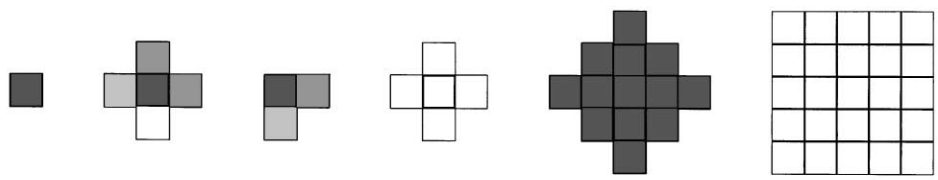

Fig. 5. Some examples of templates used in MIP. As in most practical image processing work we adopt the convention that the intensity is digitized in the range $[0,255]$. Template (1): $T(0,0) = 64$; (2): $T(0,0) = 64$, $T(1,0) = 128$, $T(0,1) = 128$, $T(-1,0) = 192$, $T(0,-1) = 255$; (3): $T(0,0) = 64$, $T(1,0) = 128$, $T(0,-1) = 192$; (4): $T(0,0) = T(1,0) = T(0,1) = T(-1,0) = T(0,-1) = 255$; (5): $T(0,0) = \cdots = T(1,-1) = 110$; (6): $T(0,0) = \cdots = T(2,-2) = 255$.

Erosion $\mathscr{E}$ uses the minimum instead of the maximum:

$$\mathscr{E}(I,T)(i,j) \equiv \min_{\langle k,l\rangle_T} [I(i+k,j+l) - T(k,l)] \,. \tag{8}$$

The maximum and minimum are to be taken over all values of displacement $\langle k,l\rangle_T$ of the template T. In general for some (i,j), $(i-k,j-l)$ may well go out of the bounds of array $I(i,j)$, a situation we already anticipated for by setting $I(i,j) = -\infty$ whenever (i,j) is out of bounds. A similar argument applies to erosion: If one of the pixels $I(i+k,j+l) = -\infty$, in the output image the pixel at position (i,j) will be undefined too. Usually undefined pixels are displayed in background color (black on a display, white on paper).

In Fig. 6 we show some illustrative examples of $\mathscr{D}$ and $\mathscr{E}$. We used three different templates to perform dilate $\mathscr{D}$ and erode $\mathscr{E}$ on a rather schematic picture of a rabbit. The original image is shown in the top left panel of Fig. 6($\mathscr{D}$ and $\mathscr{E}$). The top right image of Fig. 6($\mathscr{D}$) is obtained by replacing a pixel by its most intense nearest neighbor. This has the effect of transforming gray pixels at the boundaries of the gray objects into white pixels. The same happens to black pixels touching white and gray objects, hence the rabbit gets inflated a little. The bottom left panel of Fig. 6($\mathscr{D}$) shows the effect of changing the intensity during the process of dilation. In this case we use $\mathscr{D}$ to remove all the gray objects of the rabbit, increase the size of the rabbit and change the background color. The bottom right panel of Fig. 6($\mathscr{D}$) shows the result of using a square (5×5) template. Apparently, this template is so large that $\mathscr{D}$ replaces all gray objects by white ones, except for the legs of the rabbit, which get severely distorted. If our intention was to extract certain features from the original image of the rabbit, using the large square template obviously is not the right thing to do. Indeed, as

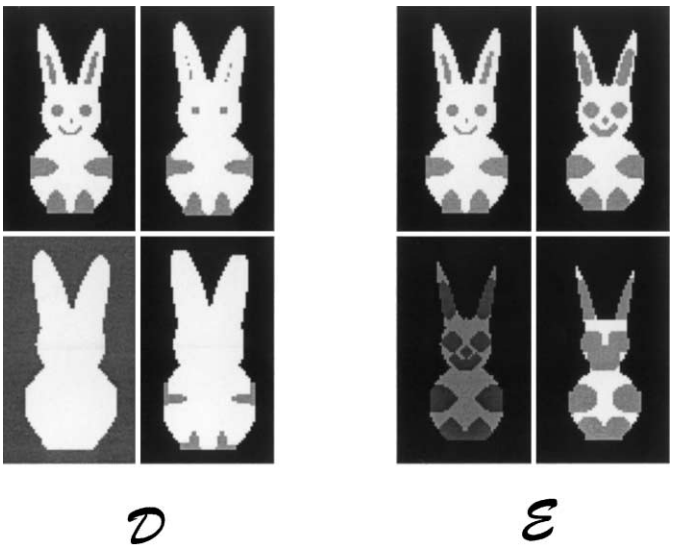

Fig. 6. Illustration of Dilate $\mathscr{D}$ and Erode $\mathscr{E}$ of a gray-scale image (top left panel). Top right: star-shaped template of size 1; bottom left: star-shaped template of size 2; bottom right: square-shaped template of size 2. The values of the templates is zero in all cases.

mentioned earlier, the choice of the template is directly linked to the viewers expectation about the morphological content of the image.

A similar sequence of images, obtained by employing $\mathscr{E}$ instead of $\mathscr{D}$, is shown in Fig. 6($\mathscr{E}$). Not surprisingly, the "min" operation generally reduces the number of non-black pixels, i.e. the rabbit shrinks. However $\mathscr{E}$ can increase the area of gray objects too. The top-right image shows that $\mathscr{E}$ tends to emphasize internal structures: Eyes, inner ears, legs and other features became larger. The "star" template of size 2 (see Fig. 5 (5)) reduces the gray level of all defined pixels (viewed on a computer screen "black" and "undefined" are synonymous). Also, it reduces the number of dark-gray objects. As in the case of $\mathscr{D}$, using an oversized square template (bottom right panel) yields a fairly distorted image of the rabbit.

The basic morphological operations $\mathscr{D}$ and $\mathscr{E}$ can be used to construct other operations that perform more complicated filtering operations. There are two other operations called Open ($\mathscr{O}$) and Close ($\mathscr{C}$) that play a central role in MIP [7]. *Open* and *Close* are defined as

$$\mathscr{O}(I,T) \equiv \mathscr{D}(\mathscr{E}(I,T),T) \tag{9}$$

and

$$\mathscr{C}(I,T) \equiv -\mathscr{O}(-I,-T)\,, \tag{10}$$

where $-I \equiv -I(i,j)$ and $-T \equiv -T(k,l)$. Open and Close have all the mathematical properties that are required for MIP [7]. In particular, $\mathscr{O}$ and $\mathscr{C}$ are idempotent, i.e. $\mathscr{O}(\mathscr{O}(I,T),T) = \mathscr{O}(I,T)$ and $\mathscr{C}(\mathscr{C}(I,T),T) = \mathscr{C}(I,T)$, implying that in practice it does not help to "open" or "close" an image twice or more using the same template.

In Fig. 7 we illustrate the effect of $\mathscr{O}$ and $\mathscr{C}$, again using the image of the rabbit as an example. Open and Close act as filters, the exact result of the filtering operation depending on the template. Open $\mathscr{O}$ generally rounds corners from the inside of the objects (see the legs of the rabbit in Fig. 7($\mathscr{O}$)

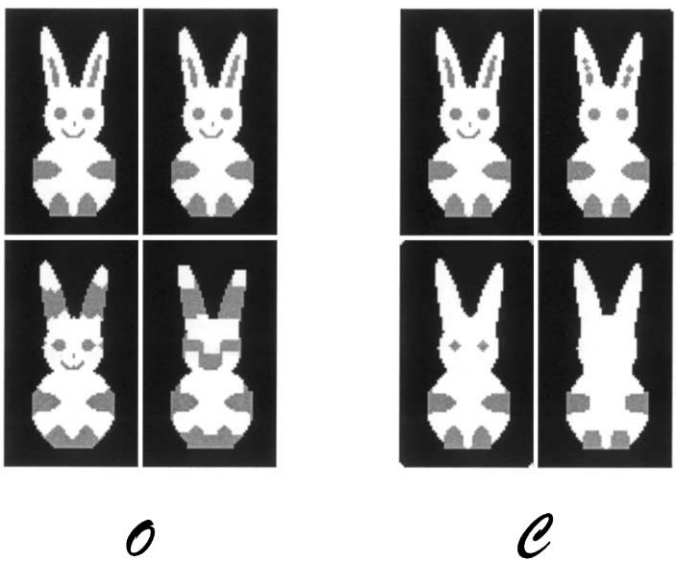

Fig. 7. Illustration of Open $\mathscr{O}$ and Close $\mathscr{C}$ of a gray-scale image (top left panel), using the same templates as in Fig. 6.

for example). Close $\mathscr{C}$, on the other hand, smooths from the outside. Objects that do not fit the template are removed from the image (see Fig. 7($\mathscr{C}$)).

It is instructive to compare, e.g. $\mathscr{E}$ and $\mathscr{C}$ (top right panel of Figs. 6($\mathscr{E}$) and 7($\mathscr{C}$)). We see that $\mathscr{E}$ generally increases the size of the gray features whereas $\mathscr{C}$ removes the small gray features but leaves other gray objects intact. This is most clearly seen by comparing the bottom right panel of Figs. 6($\mathscr{E}$) and 7($\mathscr{C}$) that show the results of $\mathscr{E}$ and $\mathscr{C}$ using the square template. Whereas $\mathscr{C}$ does not change the overall image very much, $\mathscr{E}$ makes the rabbit look like a cat. Our experience is that in practice $\mathscr{O}$ and $\mathscr{C}$ are more useful than $\mathscr{D}$ and $\mathscr{E}$.

3.3. Black-and-white images

Obviously, a black-and-white image $BW \equiv BW(i,j)$ may be considered as special case of the gray-scale images treated earlier. As such a discussion of black-and-white MIP may seem superflucious. However, in practice, it is often necessary to perform MIP on the gray-scale image, convert it to black-and-white, and carry out some further MIP on the black-and-white image before the image can be used as input for MIA. Therefore, it is worthwhile to discuss MIP on black-and-white images in more detail.

On a computer display a black pixel may be considered as being undefined [7]. Instead of assigning undefined pixels the value $-\infty$, in this case it is more convenient to assign to a black pixel the traditional value of zero. A white pixel takes the value one. Hence, a black-and-white image BW is represented by an array of Boolean variables $BW(i,j)$. In analogy with gray-scale MIP the four basic operations dilate $\mathscr{D}$, erode $\mathscr{E}$, open $\mathscr{O}$ and close $\mathscr{C}$ are defined by

$$\mathscr{D}(BW,T)(i,j) \equiv \bigcup_{\langle k,l\rangle_T} BW(i-k,j-l)\,, \tag{11a}$$

$$\mathscr{E}(BW,T)(i,j) \equiv \bigcap_{\langle k,l\rangle_T} BW(i+k,j+l)\,, \tag{11b}$$

$$\mathscr{O}(BW,T) \equiv \mathscr{D}(\mathscr{E}(BW,T),T)\,, \tag{11c}$$

$$\mathscr{C}(BW,T) \equiv \mathscr{E}(\mathscr{D}(BW,-T),-T)\,, \tag{11d}$$

respectively. Operations (11a)–(11c) are Boolean versions of (7), (8) and (9), respectively, but this is not the case for pair (10) and (11d) [7]. Operations (11a) and (11b) are digital versions of set-theoretic operators known as Minkowski addition and subtraction [7]. The latter are basic concepts in point-set geometry and integral geometry [8]. This correspondence suggests that MIP and MIA are closely related and indeed they are [7].

The collection of images shown in Figs. 8 and 9 serve to illustrate the effect of these four operations on the thresholded image of the rabbit (top left panel). The threshold is chosen such that the gray pixels are converted to black ones. The examples shown would suggest that MIP of gray-scale images followed by thresholding yields pictures that are almost identical to the corresponding morphological imaging processed black-and-white images. As a matter of fact comparison of the bottom left panel of Figs. 6($\mathscr{D}$) and 8($\mathscr{D}$) already shows that interchanging the order in which thresholding and MIP are performed changes the output. Indeed after MIP of the black-and-white image, some of the internal features remain visible, notably legs and eyes. In

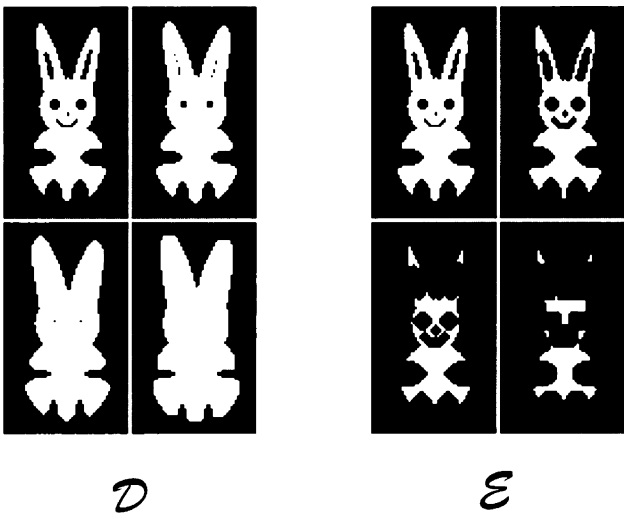

Fig. 8. Illustration of Dilate $\mathscr{D}$ and Erode $\mathscr{E}$ of a black-and-white image (top left panel), using the same templates as in Fig. 6.

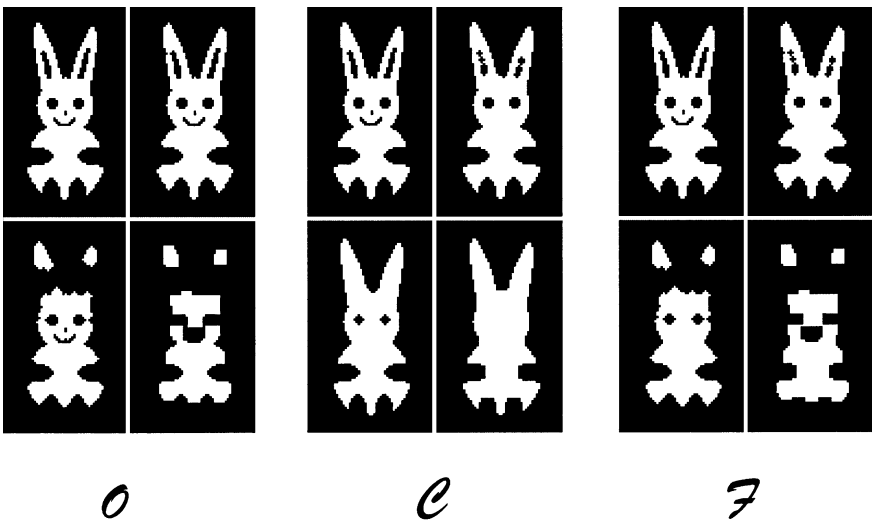

Fig. 9. Illustration of Open $\mathscr{O}$, Close $\mathscr{C}$ and Filter $\mathscr{F}$ of a black-and-white image (top left panel), using the same templates as in Fig. 6.

contrast MIP of the gray-scale image yields a completely smoothed image of the rabbit. For the input image of the rabbit used in the examples, interchanging thresholding and Erode (or Open or Close) yields the same output image. In general, this will not be the case unless the images have a very simple gray-scale structure, as the ones considered here.

As a final example of MIP we consider a more complicated filter $\mathscr{F}$ defined as [7]

$$\mathscr{F}(BW, T) \equiv \mathscr{C}(\mathscr{O}(BW, T), T) \, . \tag{12}$$

Also this filter is effective in removing small noisy structures (small with respect to the template T), and leaves larger objects intact, whereas $\mathcal{O}$ has the tendency to tear objects apart (see bottom right panel of Fig. 9($\mathcal{O}$)) and $\mathcal{C}$ has the opposite effect. Filter $\mathcal{F}$ may give a more satisfactory output image in some cases.

3.4. Miscellaneous operations

Averaging an image using a template can sometimes help to remove artifacts. In our notation this operation reads

$$I'(i,j) = \frac{1}{\#T} \sum_{\langle k,l \rangle_T} I(i+k, j+l) \,, \tag{13}$$

where $\#T$ denotes the number of elements of template T. As before, in computing this average, we use the template to express our a priori knowledge or expectation about the shape and size of the objects in the image.

Often it is useful to enhance the contrast of a gray-scale image. Again we can use a template to perform this task. For each pixel in the image $I(i,j)$ we determine $M(i,j) \equiv \max_{\langle k,l \rangle_T} I(i+k, j+l)$ and $m(i,j) \equiv \min_{\langle k,l \rangle_T} I(i+k, j+l)$ and then replace each pixel in the image by invoking the rule:

$$I'(i,j) = \begin{cases} m & \text{if } I(i,j) - m < M - I(i,j) \,, \\ M & \text{if } I(i,j) - m > M - I(i,j) \,. \end{cases} \tag{14}$$

Note that the value of the template does not play any role in this operation.

3.5. Mapping gray-scale to black-and-white images

Excluding applications of MIA that use the threshold as a control parameter (see Section 2.4), in many situations it may be expedient to reduce the number of different gray values in an image. For instance, to determine the number of objects in a gray-scale image, we will have to group pixels according to their gray value. Fluctuations in the gray values due to noise and other experimental limitations may prevent us from making the correct identification if we use the full resolution of gray values (typically 256 values). Clearly, a procedure that reduces the number of gray-scale levels may be very useful.

Thus, we would like to have a procedure to map the original gray-scale image onto another one with only a small number N of distinct gray levels (e.g. $N = 2, 4$). A simple approach would be to use histogram equalization to optimize the dynamic range of the gray levels, followed by thresholding to classify pixels as either background or objects [3,4]. Clearly, it is much better to use a scheme that computes a nearly optimal distribution of the N gray levels from the original image itself. The method we will describe next performs very well in practice. It is a gray-scale version of a scheme that is used to determine nearly optimal color pallets [27].

The first step of the algorithm consists of making a histogram of the gray-scale image. This we can easily do at full gray-scale resolution. Let us consider the case of a reduction by a factor of two (i.e. $N = 128$). We want to group gray levels but keep the image quality as high as possible. Which gray level should we remove first? A natural choice would be to select from the histogram the gray

level k with the lowest count, say $0 \leq k \leq 255$. Then we merge the bins $2[k/2]$ and $2[k/2]+1$ ($[k/2] = k/2$ if k is even, $[k/2] = (k-1)/2$ if k is odd). This we do by adding the count of bin $2[k/2]+1$ to the count of bin $2[k/2]$ and then clearing bin $2[k/2]+1$. This process of merging bins is repeated until we have 128 empty bins (which could be rather exceptional) and we can stop the whole procedure or until we conclude that all posibilities to merge two bins have been exhausted. In the latter case we repeat the procedure by grouping the bins $4[k/4]$, $4[k/4]+2$ (note that in the previous step the counts in bins $4[k/4]+1$ and $4[k/4]+3$ have been set to zero). Thereby care has to be taken to group the same four bins only once, a technical but crucial point. Again we repeat this process, always working with groups of four bins, until the number of bins with a count larger than zero is 128 (in which case the procedure terminates) or we keep restarting the grouping of bins using increments of $8, 16, \ldots$ and so on. Clearly, this procedure terminates as soon as the number of distinct gray levels becomes equal to the desired number of gray levels. Then it is a straightforward matter to assign new gray-scale values to the pixels of the original image. Although there is some ambiguity in chosing the strategy for grouping bins, experience has shown that the procedure outlined here yields very satisfactory gray-scale images, and can be used to automatically reduce a gray-scale image to a black-and-white picture.

4. Scanning electron microscope images of nano-ceramics

As an example of an application of MIP we consider the problem of identifying objects in scanning electron microscope (SEM) images of nano-ceramic materials. These materials may exhibit physical properties such as ductility, toughness and hardness of both metals and ceramics and are useful for a number of technological applications that demand good mechanical behavior and good resistance against the degrading effects of high temperature, corrosive environments, etc. These materials can be manufactured by different techniques, for instance by covering a surface by layers of nano-sized ceramic particles. The mechanical and other properties of these materials depend on the morphology, the microstructure and the initial stress due to the use of dissimilar materials. Different preparation techniques and additional (heat) treatments often yield materials that have different morphologies [28–30].

The changes in the morphology during the sintering process can be monitored by means of high-resolution low-voltage scanning electron microscopy (HRSEM) [31]. In Fig. 10 we show two SEM images of SiO_2 particles on a substrate of fused silica, before (top panel) and after (bottom panel) a heat treatment [31,32]. From Fig. 10 it is clear that the latter causes particles to aggregate. Although their size does not seem to change much, the voids get larger. A more quantitative analysis of such images requires the identification of objects (i.e. particles) in the image. MIP is well suited for this purpose.

At the right-hand side of Fig. 10 we depict the images obtained by MIP. The fluctuations in the intensity (i.e. gray value) within what our eyes would consider to be one particle can be rather large. This experimental artifact can be removed from the image by means of $\mathcal{O}$ (open) and contrast enhancement operations, both using as a template a disc with a radius of 10 pixels. The size of the template reflects our rough guess about the size of the objects. Then we use the algorithm described in Section 3.5 to map the gray-scale image onto a black-and-white picture. The final step consists of removing some minor artifacts of the size of one pixel by means of a $\mathcal{C}$ (close) operation. For this

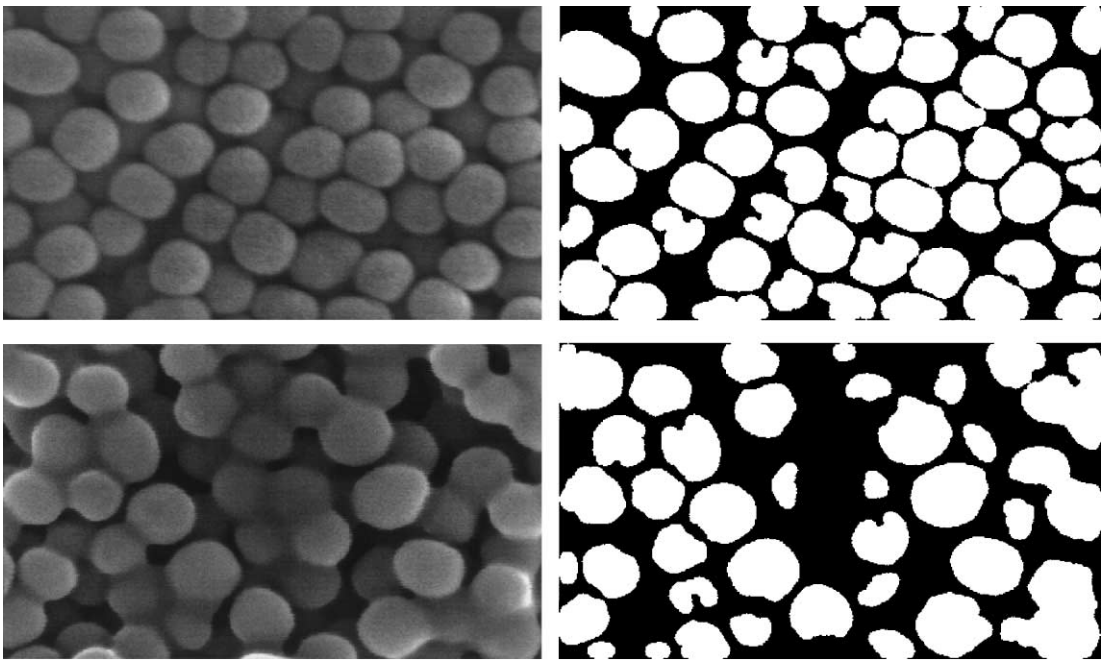

Fig. 10. Electron microscope micrographs of silica at two stages of the sintering process before (left) and after (right) MIP.

purpose we use a single pixel as a template. Clearly the quality of these black-and-white pictures is sufficiently good for further analysis of the particle size, distribution etc.

In Fig. 11 we present SEM images of another material, TiO_2 on the same substrate. Depending on the heat treatment grains of TiO_2 grow in size, leading to the mosaic-like coverages shown in Fig. 11 [31,33]. Also in this case gray-scale $\mathcal{O}$ and contrast-enhancement operations are used to remove noisy features from the image. Here the template is a 4-pixel-radius disc, smaller than in the previous example, but consistent with our expectation that the images of individual grains are smaller. Then the images are converted to black-and-white pictures, using the same procedure as the one described above. Also in this case the final pictures are of sufficient quality so that objects can easily be identified and analyzed.

As a final example we consider a rather different type of system, namely small Mn_3O_4 precipitates in Ag observed by high-resolution transmission electron microscopy (HRTEM). The top-left panel of Fig. 12 shows a high-resolution picture of a small part of the sample shown in the bottom-left panel. From the former we would like to extract information about the geometrical properties of the individual grains, from the latter we want to learn how the particles are distributed over the surface. It is somehow remarkable that the same MIP procedure can be used for both, apparently quite different, tasks. The top-left image has very low contrast. Moreover, due to experimental conditions, the averaged intensity at the left-hand side of the image differs significantly from the one at the right-hand side. After correcting for this artifact, repeated averaging and contrast enhancement operations with a 15-pixel-radius template followed by the standard of mapping to black-and-white yields the image shown in the top-right panel of Fig. 12. The bottom-left image is processed in the same manner, except that instead of a 15 pixel-size disc we use

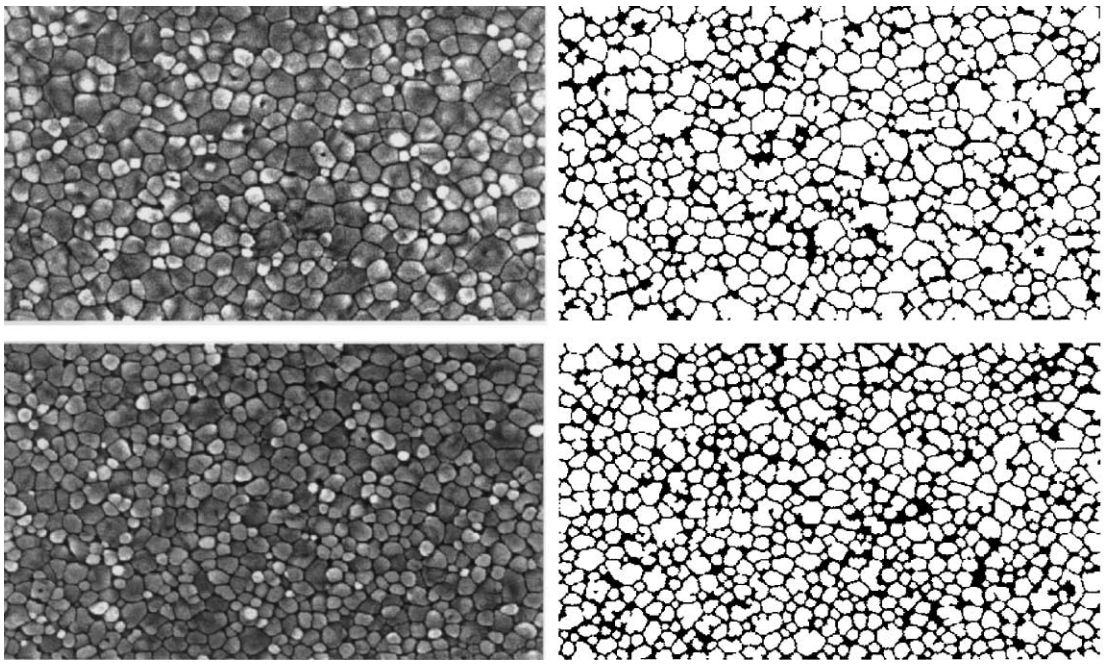

Fig. 11. Electron microscope micrographs of zirconia at two stages of the sintering process before (left) and after (right) MIP.

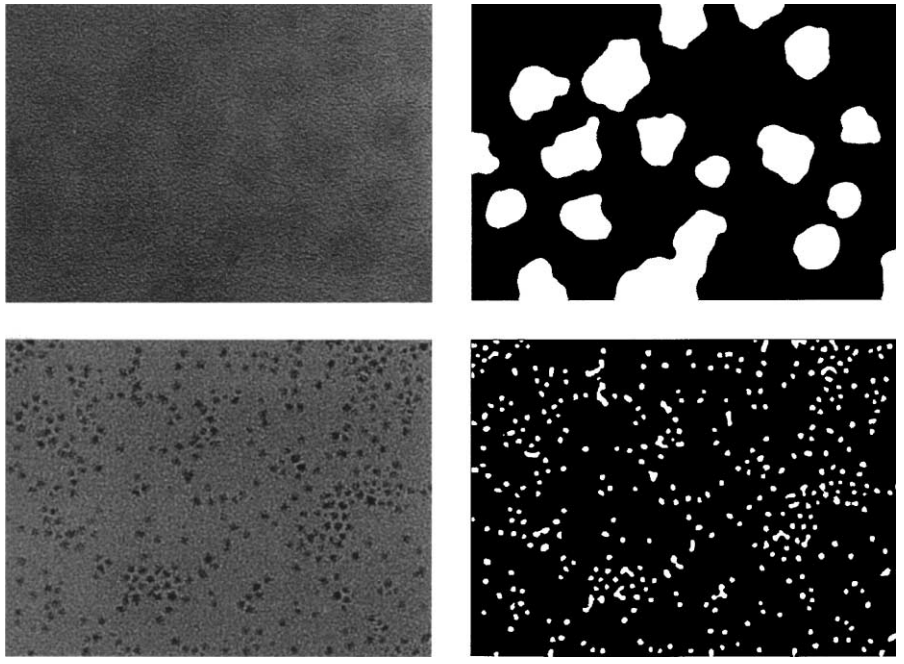

Fig. 12. High-resolution electron microscope image of Mn_3O_4 precipitates before (left) and after (right) MIP.

a radius of 4 pixels and we added a $\mathscr{D}$ (Dilate) step to remove some sharp edges from the objects. Physically, relevant information about the particle size and spatial distribution is easily extracted from these pictures.

The examples discussed above illustrate that MIP is a flexible and powerful tool for enhancing image quality and object identification, without destroying the morphological content of the image. Of course, depending on the type of image technique used, additional non-morphological image processing steps may be required to produce patterns that are suitable for morphological image analysis. As the emphasis of this paper is on image analysis rather than on image processing an in-depth discussion of the latter is outside the scope of the paper and we refer the reader to standard treatises on the subject [3–6]. We now review the theory that provides a rigorous framework for the quantitative characterization of the morphological properties of black-and-white images.

5. Integral geometry

In this section we present the mathematics that lies at the heart of integral-geometry-based morphological image analysis. The reader who is not interested in the mathematics can skip this section and resort to Section 2.

5.1. Preliminaries

Consider the set of points of a line L of length a embedded in one-dimensional (1D) Euclidian space. We take a similar line of length $2r$ and put the center of this line at each point of the line L. How does the union of all these points look like? Obviously, it is another line that is longer than L. The sets L (black line) and L_r (union of black and light gray lines), the result of this operation, are shown in Fig. 13. The length l of L_r is given by

$$l(L_r) = a + 2r = l(L) + 2r \ . \tag{15}$$

The set L_r is called the parallel set of L at a distance r.

The one-dimensional case easily extends to two and three dimensions. We consider a circular disk D of radius a, a square Q of edge length a and a equilateral triangle T of side length a embedded in the 2D space. Now, we use a disc of radius r and perform the same operation as we did for the 1D case: We put the center of the disc of radius r at each point of D (or Q or T) and consider the union of all points. The resulting parallel sets at a distance r are shown in Fig. 13. The area A of D_r, Q_r and T_r is given by

$$A(D_r) = \pi a^2 + 2\pi ar + \pi r^2 \ , \tag{16a}$$

$$A(Q_r) = a^2 + 4ar + \pi r^2 \ , \tag{16b}$$

$$A(T_r) = \frac{\sqrt{3}}{4}a^2 + 3ar + \pi r^2 \ . \tag{16c}$$

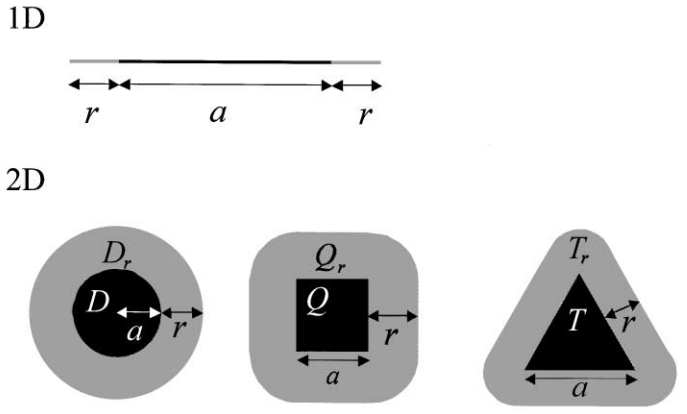

Fig. 13. Parallel sets K_r (union of black and grey area) at a distance r of the sets K (black area). Top: parallel set of a line segment L of length a embedded in one dimension; bottom: parallel set of a circular disk D of radius a, a square Q of edge length a and an equilateral triangle T of side length a embedded in the two-dimensional space.

Formulae (16) suggest that there may be a general relationship between the area of the original set and its parallel set at a distance r. It is not difficult to see that the areas of the three parallel sets can be written as

$$A(K_r) = A(K) + U(K)r + \pi r^2 \,, \tag{17}$$

where $U(K)$ denotes the boundary length (or perimeter) of the geometrical object K. The similarity between the construction of the parallel sets and the dilation of an image by means of a template of "radius" r is not an accident: Dilation on a black-and-white image (see Section 3.3) is a digital equivalent of building the parallel set in Euclidian space [7]. This again shows that MIA and MIP have common roots.

As a last example we consider a cube C of edge length a embedded in 3D space. A simple calculation shows that the volume V of the parallel set C_r can be written as

$$V(C_r) = a^3 + 6a^2r + 3a\pi r^2 + \frac{4\pi}{3}r^3 \,. \tag{18}$$

Again, under certain restrictions on the shape of the 3D object K, (18) suggests the generalization

$$V(K_r) = V(K) + S(K)r + 2\pi B(K)r^2 + \frac{4\pi}{3}r^3 \,, \tag{19}$$

where $S(K)$ is the surface area and $B(K)$ is the mean breadth.

What is the point of all this? The examples presented above suggest that for a sufficiently simple geometrical object, the change in the volume (area) can be computed from the original volume, area, and mean breadth (area and perimeter), as long as we inflate or deflate the object without changing its topology. This is the key to the morphological characterization of sets of points in Euclidian space. Obviously, sets of pixels can be analyzed using these concepts too but in order to

be useful in practice, there should be no constraints on the shape of the objects. The purpose of the next two subsections is to discuss the generalization of the above concept to objects of arbitrary shape.

5.2. Convex sets and Minkowski functionals

The simple geometrical bodies used in the previous subsection are special in the sense that the set of points making up the body is convex. In fact, the general relations alluded to above only hold for convex bodies. Convex bodies play an important role in integral geometry. Therefore, we will first review some of their basic properties. A collection of points K in the d-dimensional Euclidean space $\mathbb{R}^d$ is called a *convex set* if for every pair of points in K, the entire line segment joining them also lies in K. A convex set with nonempty interior is called a *convex body*. A single point $\boldsymbol{x}\in\mathbb{R}^d$ is also a convex set and convex body. We will only consider convex sets that are bounded and closed, i.e. that are *compact*. The class of all compact convex sets is denoted by $\mathbb{K}$.

The *parallel set* K_r of a compact convex set $K\in\mathbb{K}$ at a distance r is the union of all closed balls of radius r, the centers of which are points of K [9]. The operation of taking a parallel set preserves the properties of convexity and compactness, i.e. $K_r\in\mathbb{K}$ [10]. Clearly the notion of a parallel set, introduced in the previous subsection, agrees with this definition.

The general expression for the volume $v^{(d)}$ of the parallel body K_r at a distance r of a convex body K, is given by the Steiner formula [8]

$$v^{(d)}(K_r)=\sum_{\nu=0}^{d}\binom{d}{\nu}W_\nu^{(d)}(K)r^\nu\,, \tag{20}$$

where the $W_\nu^{(d)}(K)$ are called *quermassintegrals* or *Minkowski functionals* and are given by

$$W_0^{(1)}(K)=l(K),\quad W_1^{(1)}(K)=2,\quad d=1\,, \tag{21a}$$

$$W_0^{(2)}(K)=A(K),\quad W_1^{(2)}(K)=\tfrac{1}{2}U(K),\quad W_2^{(2)}(K)=\pi,\quad d=2\,, \tag{21b}$$

$$W_0^{(3)}(K)=V(K),\quad W_1^{(3)}(K)=\tfrac{1}{3}S(K),\quad W_2^{(3)}(K)=\frac{2\pi}{3}B(K)\,,$$

$$W_3^{(3)}(K)=\frac{4\pi}{3},\quad d=3\,. \tag{21c}$$

Clearly (21) generalizes the results for the simple examples given above and confirms that the Minkowski functionals have an intuitively clear meaning. It can be shown [8] that the Minkowski functionals are

- *Motion invariant*: A functional is *motion invariant* if $\varphi(gK)=\varphi(K)$ for $K\in\mathbb{K}$ and $g\in\mathscr{G}$. Here $\mathscr{G}$ denotes the group of all translations and rotations in $\mathbb{R}^d$. If we think of φ as an image functional, this condition assures that the result of the measurement φ does not depend on the choice of the coordinate system.
- *C-additive*: A functional is *C-additive* if $\varphi(K_1\cup K_2)=\varphi(K_1)+\varphi(K_2)-\varphi(K_1\cap K_2)$ for $K_1,K_2\in\mathbb{K}$ and $K_1\cup K_2\in\mathbb{K}$. The notion of *C-additive* (means additive on the set $\mathbb{K}$) is not just

a technical one because the union of two convex sets is not necessarily convex, although the intersection is.

- *Continuity*: φ is *continuous* if $\lim_{l\to\infty}\varphi(K_l)=\varphi(K)$ whenever $\{K_l\}$ is a sequence of compact sets such that $\lim_{l\to\infty}K_l=K$ in the Hausdorff metric [7]. Intuitively, this continuity property of φ means that whenever the compact convex sets K_l approach the compact convex set K, also $\varphi(K_l)$ approaches $\varphi(K)$. This is a rather technical condition that is satified when we limit ourselves to sets of pixels.

A fundamental result in integral geometry is the completeness of the family of Minkowski functionals. A theorem by Hadwiger [8] states that every motion invariant, C-additive and continuous functional φ over $\mathbb{K}$ can be written as

$$\varphi(K)=\sum_{\nu=0}^{d}a_\nu W_\nu^{(d)}(K) \tag{22}$$

with suitable coefficients $a_\nu\in\mathbb{R}$. In other words, the $d+1$ Minkowski functionals form a complete system of morphological measures on the set of convex bodies [8].

What is the relevance of the above to image functionals? In the Introduction we mentioned that MIA uses additive image functionals. Of course, we prefer to use motion invariant, additive image functionals. However, there is no reason why an image should be a convex set, so if we could replace "C-additive" by "additive" then Hadwiger's theorem would tell us that there are no more, no less than $d+1$ different additive image functionals. This would be a nice result because it implies that we would have to switch to non-additive or coordinate-system-dependent image functionals to find additional non-morphological structure in the image. However, the extension of Hadwiger's theorem to additive instead of C-additive image functionals requires further consideration.

5.3. Convex rings and additive image functionals

The results of the previous subsection can be generalized to a much more general class of objects by considering the *convex ring* [8] $\mathscr{R}$, the class of all subsets A of $\mathbb{R}^d$ which can be expressed as finite unions of compact convex sets

$$A=\bigcup_{i=1}^{l}K_i;\quad K_i\in\mathbb{K}\ . \tag{23}$$

If A_1 and A_2 both belong to $\mathscr{R}$ then so do $A_1\cup A_2$ and $A_1\cap A_2$. As before, an additive functional φ has the property $\varphi(A_1\cup A_2)=\varphi(A_1)+\varphi(A_2)-\varphi(A_1\cap A_2)$. Motion invariance of φ on $\mathscr{R}$ is defined as for φ on $\mathbb{K}$. Obviously, an image is an instance of the convex ring $\mathscr{R}$, the pixels being the convex sets and elements of $\mathbb{K}$.

Fundamental to the extension from $\mathbb{K}$ to $\mathscr{R}$ is the *Euler characteristic* or *connectivity number* χ defined as [8]

$$\chi(K)=\begin{cases}1, & K\neq\emptyset\ ,\\ 0, & K=\emptyset\end{cases} \tag{24}$$

for all $K \in \mathbb{K}$. The Euler characteristic is an additive, motion invariant functional on $\mathscr{R}$ [8]. For an element A of the convex ring $\mathscr{R}$, the use of the property of additivity of χ yields

$$\chi(A) = \chi\left(\bigcup_{i=1}^{l} K_i\right) = \sum_i \chi(K_i) - \sum_{i<j} \chi(K_i \cap K_j) + \cdots + (-1)^{l+1}\chi(K_1 \cap \cdots \cap K_l) \,. \tag{25}$$

The value of $\chi(A)$ is independent of the representation of A as a finite union of compact convex sets [8]. Note that all sets appearing on the r.h.s. of (25) are convex so that we can use (24) to compute the numerical (integer) value of $\chi(A)$.

The Euler characteristic can be used to define the Minkowski functionals for all elements of the convex ring $A \in \mathscr{R}$ [8]. Recalling that a single point $\boldsymbol{x} \in \mathbb{R}^d$ is a convex set, we can write the characteristic function of the set A as $I_A(\boldsymbol{x}) = \chi(A \cap \boldsymbol{x})$. Then the volume of A is given by $W_0^{(d)}(A) = \int_{\mathscr{G}} I_A(g\boldsymbol{x})\,\mathrm{d}g$. Here $\mathrm{d}g$ denotes the motion-invariant kinematical density [8,9] and the integration is over all elements of $\mathscr{G}$ [8,9]. The expression of the volume suggests the following definition [8] of the Minkowski functionals on $\mathscr{R}$:

$$\begin{aligned} W_\nu^{(d)}(A) &= \int_{\mathscr{G}} \chi(A \cap gE_\nu)\,\mathrm{d}g \quad \nu = 0, \ldots, d-1 \,, \\ W_d^{(d)}(A) &= \omega_d \chi(A) \quad \omega_d = \pi^{d/2}/\Gamma(1 + d/2) \,, \end{aligned} \tag{26}$$

where E_ν is a ν-dimensional plane in $\mathbb{R}^d$. The normalization is chosen such that for a d-dimensional ball $B_d(r)$ with radius r, $W_\nu^{(d)}(B_d(r)) = \omega_d r^{d-\nu}$ where ω_d denotes the volume of the unit ball ($\omega_0 = 1$, $\omega_1 = 2$, $\omega_2 = \pi$, $\omega_3 = 4\pi/3$) [14].

The Minkowski functionals inherit from χ the property of additivity

$$\begin{aligned} W_\nu^{(d)}(A) = W_\nu^{(d)}\left(\bigcup_{i=1}^{l} K_i\right) &= \sum_i W_\nu^{(d)}(K_i) - \sum_{i<j} W_\nu^{(d)}(K_i \cap K_j) + \cdots \\ &\quad + (-1)^{(l+1)} W_\nu^{(d)}(K_1 \cap \cdots \cap K_l) \end{aligned} \tag{27}$$

and motion invariance. Hadwiger [8] has shown that representation (22) is also valid for elements of the convex ring $\mathscr{R}$. The $d+1$ Minkowski functionals form a complete system of additive functionals on the set of objects that are unions of a finite number of convex bodies [8].

In the translation of these abstract mathematical results to MIA it is essential to keep in mind the conditions under which the mentioned theorems hold. Fortunately, in practice, this is easy to do. The crucial step is to decompose the image into a union of convex sets so that we can use the theoretical results that hold on the convex ring. We address this issue in Section 5.5.

For completeness and also because we make use of it in Section 7, we state one more important result in integral geometry, the so-called kinematic formulae. These are very useful tools in stereology and stochastic geometry [8,9,25]. They play a key role in deriving averages of Minkowski functionals (see Appendix D for an example). Hadwiger's principal kinematic formulae read [8]

$$\int_{\mathscr{G}} M_\nu^{(d)}(A \cap gB)\,\mathrm{d}g = \sum_{\mu=0}^{\nu} \binom{\nu}{\mu} M_{\nu-\mu}^{(d)}(B) M_\mu^{(d)}(A) \,, \tag{28a}$$

$$M_\nu^{(d)}(A) = \frac{\omega_{d-\nu}}{\omega_\nu \omega_d} W_\nu^{(d)}(A), \quad \nu = 0, \ldots, d \,. \tag{28b}$$

Using (21), (28b) and the fact that $\chi(K) = 1$ for $K \in \mathbb{K}$ we define the *normalized Minkowski functionals* as

$$M_0^{(1)}(K) = l(K), \quad M_1^{(1)}(K) = \tfrac{1}{2}\chi(K), \quad d = 1\ , \tag{29a}$$

$$M_0^{(2)}(K) = A(K), \quad M_1^{(2)}(K) = \frac{1}{2\pi}U(K)\ ,$$

$$M_2^{(2)}(K) = \frac{1}{\pi}\chi(K), \quad d = 2\ , \tag{29b}$$

$$M_0^{(3)}(K) = V(K), \quad M_1^{(3)}(K) = \tfrac{1}{8}S(K)\ ,$$

$$M_2^{(3)}(K) = \frac{1}{\pi}B(K), \quad M_3^{(3)}(K) = \frac{3}{4\pi}\chi(K), \quad d = 3 \tag{29c}$$

for all $K \in \mathbb{K}$.

5.4. Relation to topology and differential geometry

The Euler characteristic χ is identical to the one defined in algebraic topology [8]. For $d = 2$, $\chi(A)$ equals the number of connected components minus the number of holes. In three dimensions $\chi(A)$ is given by the number of connected components minus the number of tunnels plus the number of cavities. Some examples are shown in Fig. 14. The Euler characteristic describes A in a purely topological way, i.e. without reference to any kind of metric.

Very often one is interested in the topology of the surface ∂A of A [2,15]. The Euler characteristic of ∂A is directly related to that of A, namely $\chi(\partial A) = \chi(A)[1 - (-1)^n]$, where n is the dimension of the body A ($n \leq d$) [19].

The principal curvatures of a surface are useful quantities for the numerical characterization of the surface of a 3D body. They are defined as follows. Consider a point on the surface and the vector through this point, normal to the surface. A plane containing this normal vector intersects the surface. This intersection is a planar curve with a curvature called the normal curvature. Rotation of the plane about the normal produces various planar curves with different values of normal curvature. The extreme values of the normal curvatures are called the *principal curvatures* κ_1 and κ_2 of a surface. These two curvatures can be combined to give two useful measures of the curvature of a surface, namely the Gaussian and mean curvature defined as $G = \kappa_1\kappa_2$ and $H = (\kappa_1 + \kappa_2)/2$, respectively. The integral mean curvature H and integral Gaussian curvature G are given by

$$H(A) = \frac{1}{2}\int_{\partial A}\left(\frac{1}{R_1} + \frac{1}{R_2}\right)\mathrm{d}f \tag{30}$$

and

$$G(A) = \int_{\partial A}\frac{1}{R_1 R_2}\,\mathrm{d}f\ , \tag{31}$$

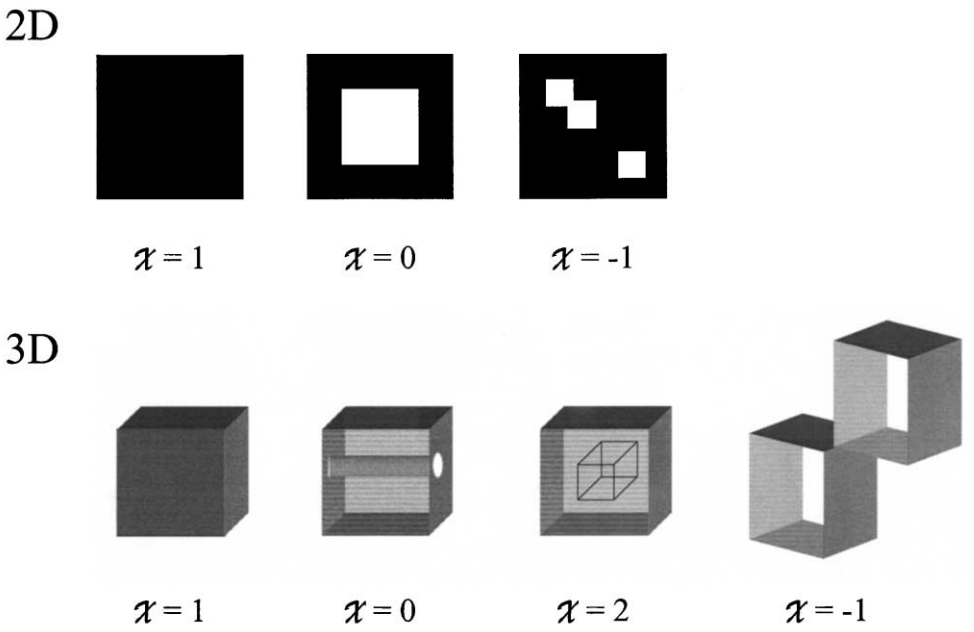

Fig. 14. Two- and three-dimensional figures with various connectivity numbers or Euler characteristics χ.

respectively. Here $R_1 = 1/\kappa_1$ and $R_2 = 1/\kappa_2$ are the principal radii of curvature of A and $\mathrm{d}f$ is the area element on A. For H and G to be well defined the boundary ∂A should be regular.

The mean breadth is proportional to the integral mean curvature:

$$H(A) = 2\pi B(A) \,. \tag{32}$$

The Euler characteristic of ∂A is closely related to the integral Gaussian curvature G and the genus g (number of handles):

$$G(A) = 2\pi\chi(\partial A), \quad \chi(\partial A) = 2(1 - g) \,. \tag{33}$$

Note that integral geometry imposes no regularity conditions on the boundary ∂A of the objects: $H(A)$ and $\chi(A)$ are always well defined.

5.5. Application to images

Each pixel in a 2D (3D) black-and-white image is a convex set. Therefore, such images may be considered as an element of the convex ring $\mathscr{R}$ and we can invoke integral geometry to build additive image functionals to measure features in the image. However, as mentioned before, some care has to be taken because the Minkowski functionals take known values on convex sets only.

The key to the practical application of integral geometry to images is the additivity of χ (see (25)): We can compute the Minkowski functionals of an image A by decomposing A into convex sets K_i. However, if we would take for $\{K_i\}$ all black pixels (assuming the background consists of white pixels), then we would have to compute all the intersections that appear in (25). Although this can be done, it is much more expedient to take a slightly different route.

First, we write each pixel K as the union of the disjoint collection of its interior body, interior faces (in 3D only), open edges and vertices [19]. We will denote the interior of a set A by $\check{A} = A \backslash \partial A$. The values of the Minkowski functionals of the open interior of an n-dimensional body $A \in \mathscr{R}$ embedded in $\mathbb{R}^d$ ($n \leq d$) are given by [19]

$$W_v^{(d)}(\check{A}) = (-1)^{d+n+v} W_v^{(d)}(A), \quad v = 0, \ldots, d \, . \tag{34}$$

By making use of the additivity of the Minkowski functionals (see (27)) and the fact that there is no overlap between open bodies on a lattice, the values of the Minkowski functionals on the whole pattern $\mathscr{P} = \mathscr{P}(\boldsymbol{x}, q)$ may be obtained from

$$W_v^{(d)}(\mathscr{P}) = \sum_m W_v^{(d)}(\check{N}_m) n_m(\mathscr{P}), \quad v = 0, \ldots, d \, , \tag{35}$$

where $n_m(\mathscr{P})$ denotes the number of the open bodies $\check{N}_m$ of type m present in $\mathscr{P}$. On a square and cubic lattice there are $d+1$ open bodies $\check{N}_m$: $\check{N}_0$ corresponds to a vertex, $\check{N}_1$ to an open line segment, $\check{N}_2$ to an open square on both the 2D square and the 3D cubic lattice, and $\check{N}_3$ to an open cube on the 3D cubic lattice. The values of the Minkowski functionals for the building blocks $\check{N}_m$ of a 2D square and a 3D cubic lattice are given in Tables 1 and 2, respectively. Their derivation is given in Appendix C. The procedure to calculate $n_m(\mathscr{P})$ is described in Appendix B. This completes the construction of the method to compute the $d+1$ additive image functionals for a d-dimensional lattice filled with black and white pixels. In essence the method boils down to the simple procedure of counting vertices, edges, etc., as described in Section 2.

We illustrate the procedure to compute the Minkowski functionals by considering the 2D checkerboard pattern with an even number L_0 of cells, of edge length one, in each direction. We consider free and periodic boundary conditions (see Fig. 15). The left picture in Fig. 15 shows the 4×4 checkerboard lattice with free boundary conditions, i.e. the pattern is completely surrounded by white pixels. The right picture shows the same pattern but with periodic boundary conditions. For the $L_0 \times L_0$ checkerboard $\mathscr{P}_{\mathrm{F}}$ with free boundary conditions we find $n_0(\mathscr{P}_{\mathrm{F}}) = (L_0+1)^2 - 2$, $n_1(\mathscr{P}_{\mathrm{F}}) = 2L_0^2$, $n_2(\mathscr{P}_{\mathrm{F}}) = L_0^2/2$ and hence $A(\mathscr{P}_{\mathrm{F}}) = L_0^2/2$, $U(\mathscr{P}_{\mathrm{F}}) = 2L_0^2$ and $\chi(\mathscr{P}_{\mathrm{F}}) = L_0^2/2 - (L_0-1)^2$. Note that this value of χ corresponds to the value we find if we calculate χ as the number of connected components minus the number of holes, since the number of connected components (black structure) equals one and the number of holes equals $(L_0/2-1)(L_0-2)$. For the $L_0 \times L_0$ checkerboard $\mathscr{P}_{\mathrm{P}}$ with periodic boundary conditions we find

Table 1
Minkowski functionals $W_v^{(2)}(v = 0, \ldots, d = 2)$ for the open bodies $\check{N}_m$, the basic building blocks of a two-dimensional square lattice. $\check{Q}$: open square of edge length a; $\check{L}$: open edge of length a; $\check{P}$: vertex. A denotes the covered area, U the perimeter and χ the Euler characteristic

m	$\check{N}_m$	$W_0^{(2)} = A$	$W_1^{(2)} = U/2$	$W_2^{(2)} = \pi\chi$
0	$\check{P}$	0	0	π
1	$\check{L}$	0	a	$-\pi$
2	$\check{Q}$	a^2	$-2a$	π

Table 2
Minkowski functionals $W_\nu^{(3)}(\nu = 0, \ldots, d = 3)$ for the open bodies $\breve{N}_m$, the basic building blocks of a three-dimensional cubic lattice. $\breve{C}$: open cube of edge length a; $\breve{Q}$: open square of edge length a; $\breve{L}$: open edge of length a; $\breve{P}$: vertex. V denotes the covered volume, S the surface area, B the mean breadth and χ the Euler characteristic

m	$\breve{N}_m$	$W_0^{(3)} = V$	$W_1^{(3)} = S/3$	$W_2^{(3)} = 2\pi B/3$	$W_3^{(3)} = 4\pi\chi/3$
0	$\breve{P}$	0	0	0	$4\pi/3$
1	$\breve{L}$	0	0	$\pi a/3$	$-4\pi/3$
2	$\breve{Q}$	0	$2a^2/3$	$-2\pi a/3$	$4\pi/3$
3	$\breve{C}$	a^3	$-2a^2$	πa	$-4\pi/3$

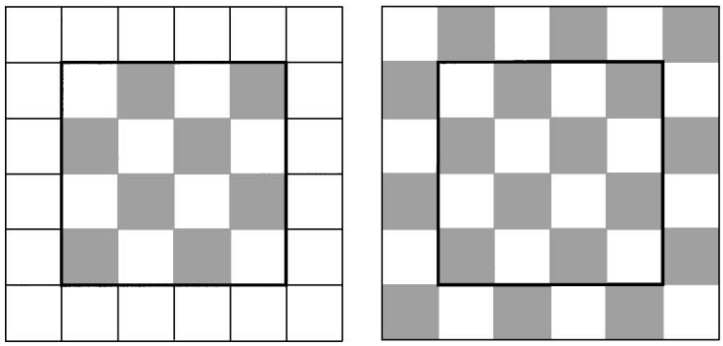

Fig. 15. 4×4 checkerboard pattern. The black line denotes the boundary. Left: free boundaries; right: periodic boundaries.

$n_0(\mathscr{P}_\mathrm{P}) = L_0^2$, $n_1(\mathscr{P}_\mathrm{P}) = 2L_0^2$, $n_2(\mathscr{P}_\mathrm{P}) = L_0^2/2$ which yields $A(\mathscr{P}_\mathrm{P}) = L_0^2/2$, $U(\mathscr{P}_\mathrm{P}) = 2L_0^2$ and $\chi(\mathscr{P}_\mathrm{P}) = -L_0^2/2$. Note that $\chi(\mathscr{P}_\mathrm{P})/L_0^2 = \lim_{L_0 \to \infty} \chi(\mathscr{P}_\mathrm{F})/L_0^2 = -1/2$.

5.6. Reducing digitization errors

The Minkowski functionals computed on the lattice of pixels, will be called *digital Minkowski functionals*. They yield approximate values of the Minkowski functionals of these objects in Euclidean space. By digitizing the 2D (3D) image we have introduced square (cubic) distortions in the objects, causing a directional bias. For example, digitizing a 2D (3D) image transforms a smooth contour (surface) to a more stepwise contour (surface). The more complicated the image the better the digital approximations are likely to become since the parts of the stepwise boundary or surface will exhibit each orientation more often. The most problematic structures may be isotropic ones. We will not treat the problems of digitization to large extent but will only give a simple method to obtain a better approximation to the Euclidean perimeter and area (covered area and volume) in two (three) dimensions.

There are several methods to correct for the systematic error, caused by digitization of the image [3,26]. A correction to the digital Minkowski functionals that leads to a better approximation of the area and perimeter in 2D (volume and covered area in 3D) can be made by explicitly taking into account the number of "steps" $n_\mathrm{S}(\mathscr{P})$ in the pattern $\mathscr{P} = \mathscr{P}(\boldsymbol{x}, q)$. In 2D (3D) patterns, "steps" are

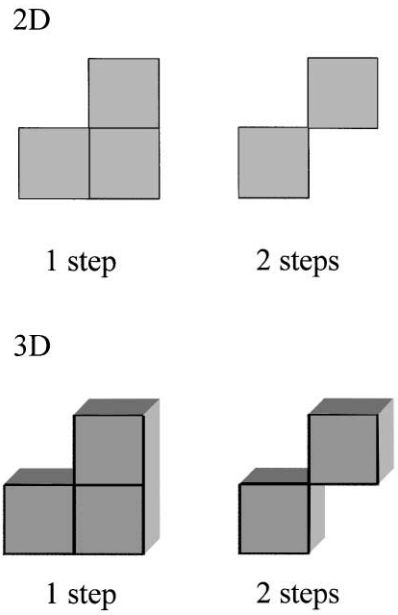

Fig. 16. Steps as defined on a 2D (3D) square (cubic) lattice.

defined by two pixels that share only one vertex (edge). Examples of steps are shown in Fig. 16. The corrected digital Minkowski functionals corresponding to the perimeter and area (covered area and volume) in 2D (3D), may be written as

$$W'^{(d)}_{\nu}(\mathscr{P}) = W^{(d)}_{\nu}(\mathscr{P}) - C^{(d)}_{\nu} n_{\mathrm{S}}(\mathscr{P}), \quad \nu = 0, 1 \ , \tag{36}$$

where $W^{(d)}_{\nu}(\mathscr{P})$ is given by (35) and $C^{(d)}_{\nu}$ denotes a correction factor. On a square and cubic lattice $C^{(2)}_0 = C^{(3)}_0 = 1$, $C^{(2)}_1 = (2 - \sqrt{2})/2$ and $C^{(3)}_1 = (2 - \sqrt{2})/3$. The procedure to calculate $n_{\mathrm{S}}(\mathscr{P})$ is described in Appendix C.

As an illustration we use this correction procedure to calculate the area and perimeter for the triangle shown in Fig. 17a. The Euclidean perimeter and area are 20.35 cm and 16.47 cm^2, respectively. As usual, we first digitize the image of the triangle by mapping the triangle on square grids. Some results for various grid spacings are shown in Figs. 17b–d. The digitization transforms the straight and smooth boundaries of the triangle to more stepwise boundaries. Using the procedure outlined in Section 2 we calculate the digital perimeter and area of the objects in Figs. 17b–d. Then by making use of (36), we compute the corrected digital perimeter and area. The results are summarized in Table 3.

As seen from Table 3 the values of the digital perimeter and area obtained using (35) are always larger than their Euclidean counterparts. Reducing the grid spacing does not lead to a fast convergence of the values of the digital perimeter and area to the values of the Euclidean ones. If we compute the digital perimeter and area using (36) the values are still larger than the Euclidean ones but the improvement is substantial.

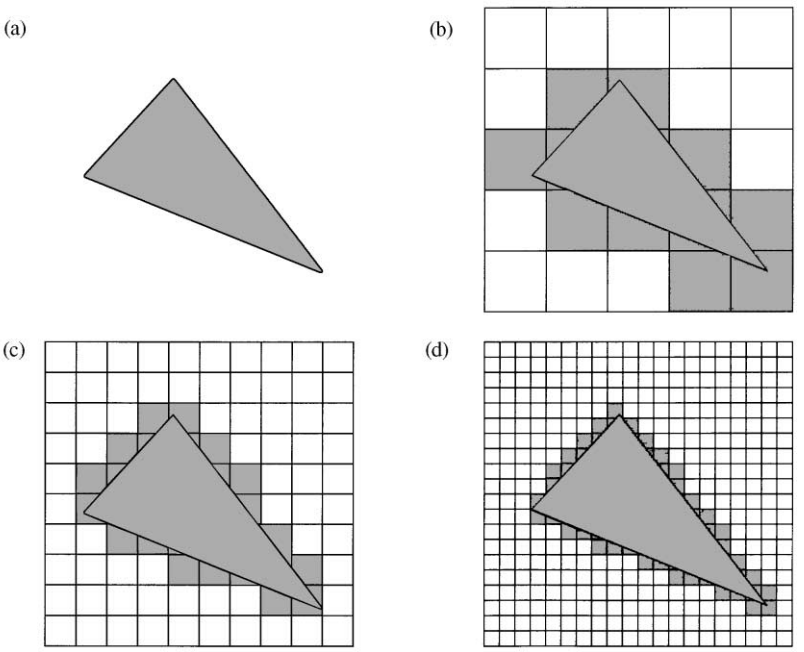

Fig. 17. Digitization process for a triangle. Triangle in Euclidean space (a); triangle mapped on a square grid with grid spacing 2 (b); 1 (c) and 1/2 (d).

Table 3
Digital and corrected digital perimeter and area of the objects shown in Figs. 17b–d. L_0 denotes the grid spacing and U, A (U', A') denotes the digital (corrected digital) perimeter and area, respectively. The Euclidean perimeter and area are 20.35 cm and 16.47 cm^2, respectively

Fig. 17	L_0	U (cm)	A (cm^2)	U' (cm)	A' (cm^2)
(b)	2	36.00	48.00	33.07	28.00
(c)	1	30.00	31.00	27.36	22.00
(d)	1/2	30.00	23.50	26.92	18.25

5.7. Normalization of image functionals

In the following sections, we calculate Minkowski functionals for 2D (3D) for a variety of square (cubic) lattice systems. For practical purposes it is convenient to introduce the following quantities:

$$\tilde{A} = A/L^2, \quad \tilde{U} = U/LN^{1/2}, \quad \tilde{\chi} = \chi/N, \quad d = 2 \tag{37a}$$

and

$$\tilde{V} = V/L^3, \quad \tilde{S} = S/L^2N^{1/3}, \quad \tilde{B} = 2B/LN^{2/3}, \quad \tilde{\chi} = \chi/N, \quad d = 3\,, \tag{37b}$$

where L denotes the linear size of the square (cube) and N denotes the number of germs.

In the case of 2D (3D) periodic structures the structures may be divided into equivalent regions bounded by a square (cubic) unit cell of space. Let us assume that the 2D (3D) periodic structure of total area L^2 (volume L^3) is composed of several unit cells of typical length scale L_0. Then the Euler characteristic χ of the whole system is given by

$$\chi = \bar{\chi}\left(\frac{L}{L_0}\right)^d \equiv \bar{\chi}M \,, \tag{38}$$

where $M \equiv (L/L_0)^d$ denotes the number of unit cells. The other morphological quantities of the whole system may be written as

$$A = \bar{A}L_0^2 M, \quad U = \bar{U}L_0 M, \quad d = 2 \,, \tag{39a}$$

$$V = \bar{V}L_0^3 M, \quad S = \bar{S}L_0^2 M, \quad B = 2\bar{B}L_0 M, \quad d = 3 \,. \tag{39b}$$

The quantities $\bar{A}$, $\bar{U}$, $\bar{V}$, $\bar{S}$, $\bar{B}$ and $\bar{\chi}$ characterize the structure within one elementary unit of the periodic structure.

6. Illustrative examples

We first apply MIA to simple cubic, face-centered cubic and body-centered cubic lattice structures with and without imperfections. We use the method described in Section 2.3 to analyze these point patterns. In Sections 6.2 and 6.3 we employ the method described in Section 2.4 to compute the value of the Minkowski functionals of some complex 3D surfaces, namely some triply periodic minimal surfaces and the Klein bottle.

6.1. Regular lattices

The face-centered cubic (FCC) and body-centered cubic (BCC) lattices are of great importance, since an enormous variety of solids and several complex fluids [34] crystallize in these forms. The simple cubic (SC) form, however, is relatively rare. The SC lattice may be generated from the following set of primitive vectors:

$$\boldsymbol{a}_1 = L_0(1,0,0), \quad \boldsymbol{a}_2 = L_0(0,1,0), \quad \boldsymbol{a}_3 = L_0(0,0,1) \,, \tag{40}$$

where L_0 denotes the lattice constant. A symmetric set of primitive vectors for the FCC cubic lattice is

$$\boldsymbol{a}_1 = \frac{L_0}{2}(0,1,1), \quad \boldsymbol{a}_2 = \frac{L_0}{2}(1,0,1), \quad \boldsymbol{a}_3 = \frac{L_0}{2}(1,1,0) \tag{41}$$

and for the BCC cubic lattice is

$$\boldsymbol{a}_1 = \frac{L_0}{2}(1,1,-1), \quad \boldsymbol{a}_2 = \frac{L_0}{2}(1,-1,1), \quad \boldsymbol{a}_3 = \frac{L_0}{2}(-1,1,1) \,. \tag{42}$$

To compute the Minkowski functionals for the SC, FCC, and BCC lattices we place them on a cubic lattice with lattice constant one, making use of (40)–(42), and we put one black pixel at each

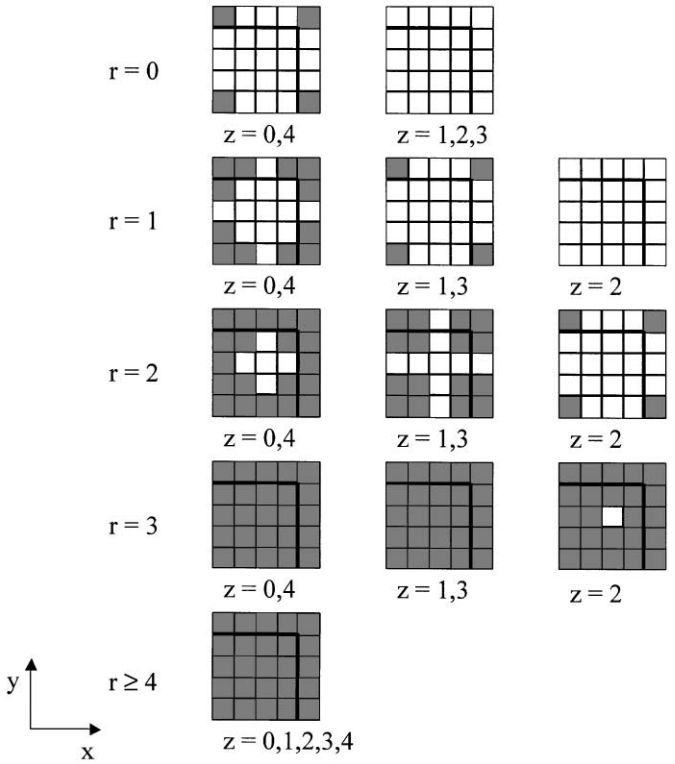

Fig. 18. Graining procedure for the SC lattice with periodic boundary conditions and $L_0 = 4$. The thick solid line indicates the dimensions of the unit cell.

point of the SC, FCC or BCC lattice, respectively. By making use of the procedure described in Section 2.3 we transform the resulting point pattern into a pattern of "spherical" grains of radius r and study the behavior of the Minkowski functionals as a function of r. An example of the graining procedure is shown in Fig. 18 for the SC lattice with periodic boundary conditions and $L_0 = 4$. The thick solid line indicates the dimensions of the conventional unit cell, simply called the unit cell from now on.

Fig. 19 shows the Minkowski functionals $\tilde{V}$, $\tilde{S}$, $\tilde{B}$ and $\tilde{\chi}$ as a function of r for the SC (dotted curve), FCC (solid curve) and BCC (dashed curve) lattice without imperfections. The SC, FCC and BCC lattices with periodic boundaries consist of one unit cell of linear dimension $L_0 = 32$. Because of normalization (37) the curves for more than one unit cell will be the same as the ones shown in Fig. 19. Fig. 19 clearly shows that the behavior of the Minkowski functionals as a function of r differs for the various lattice types. The area $\tilde{S}$ reaches a maximum if r equals $L_0/2$, $L_0\sqrt{2}/4$, $L_0\sqrt{3}/4$, for the SC, FCC and BCC lattice, respectively. At this value for r the Euler characteristic $\tilde{\chi}$ starts to deviate from one because the "spheres" touch each other. For the SC lattice $\tilde{\chi}$ jumps to -2 independent of L_0 (result not shown). In the case of the FCC (BCC) lattice and for sufficiently large L_0 ($L_0 \geq 16$) the Euler characteristic jumps to a large negative (positive) value. For the SC, FCC and BCC lattice with $r = 0$ the Euler characteristic per unit cell equals 1, 4 and 2, respectively. This corresponds to the number of "spheres" per unit cell.

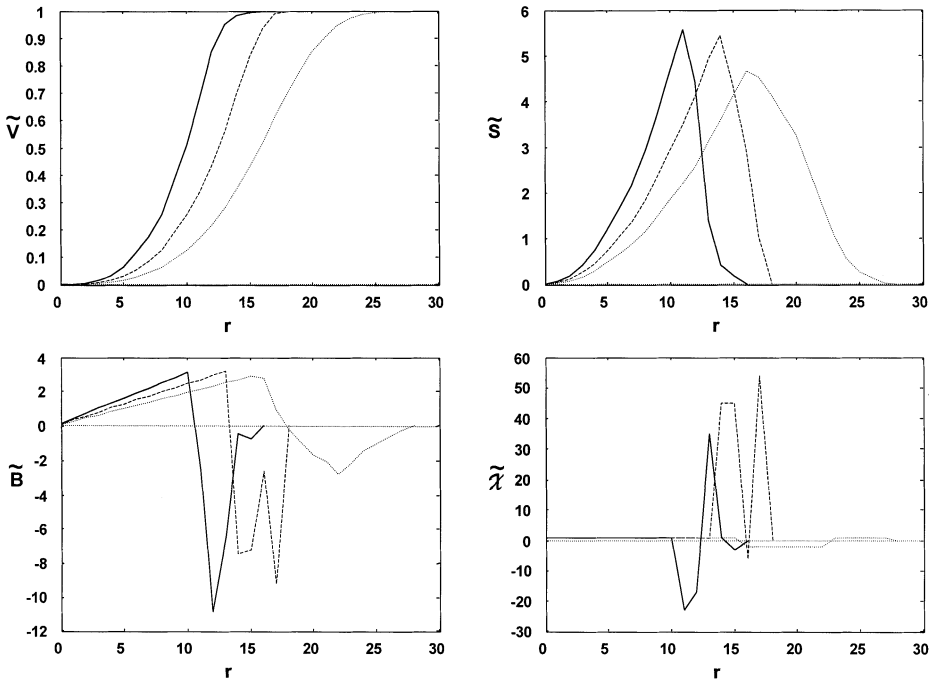

Fig. 19. Minkowski functionals as a function of r for the perfect SC (dotted curve), FCC (solid curve) and BCC (dashed curve) lattice with $M = 1$ and $L_0 = 32$ with periodic boundary conditions.

Crystal structures formed in materials are not perfect. Therefore, it is of interest to study the influence of defects on the curves shown in Fig. 19 for the BCC lattice. Imperfections in the crystal structure may be formed by the absence or by small displacements of some of the basic lattice points. Also the presence of impurities, creating extra lattice points, causes an imperfect crystal structure. In Fig. 20 we show the Minkowski functionals as a function of r for perfect and imperfect BCC lattice structures. The solid curve depicts the data for a perfect BCC lattice containing $M = 8$ unit cells of linear dimension $L_0 = 16$. The dashed curve shows the data for the same BCC lattice to which $\pm 30\%$ of defects have been added at randomly chosen positions. The dotted curve depicts the results of displacing $\pm 30\%$ randomly chosen basic lattice points over a random distance 0 or 1. Apart from some minor changes the three curves behave in the same way. Only if we move all the lattice points over a random distance 0 or 1 (dash–dotted lines), the curves for $\tilde{B}$ and $\tilde{\chi}$ differ qualitatively from the ones of the perfect BCC lattice. Therefore, we may conclude that the presence of small amounts of defects in the crystal structure does not alter the characteristic behavior of the Minkowski functionals as a function of r.

6.2. *Triply periodic minimal surfaces* [35]

A minimal surface in $\mathbb{R}^3$ is defined as a surface for which the mean curvature (see Section 5.4) is zero at each of its points. As a consequence, at every point of a minimal surface the two principal curvatures are equal, but opposite in sign. Hence the Gaussian curvature is always non-positive.

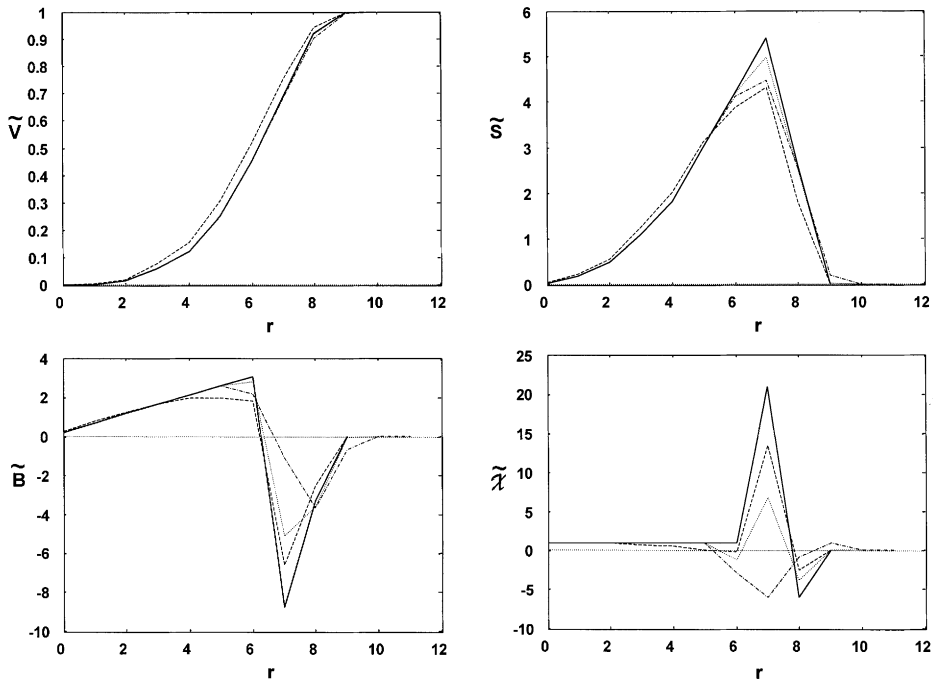

Fig. 20. Minkowski functionals as a function of r for BCC lattice structures with $M = 8$ and $L_0 = 16$ with periodic boundary conditions. Solid line: perfect BCC lattice; dashed line: BCC lattice to which $\pm$ 30% of impurities have been added at randomly chosen positions; dotted line: BCC lattice of which $\pm$ 30% of randomly chosen basic lattice points have been moved over a randomly chosen distance 0 or 1; dash–dotted line: BCC lattice of which all the basic lattice points have been moved over a randomly chosen distance 0 or 1.

For every closed circuit on the surface, the area is a minimum. We will consider the triply periodic minimal surfaces (TPMS), minimal surfaces that are periodic in three independent directions. During the last years these TPMS and similar interfaces have been elaborately discussed in literature since structures related to TPMS may form spontaneously in physico-chemical and in biological systems [2,36]. Examples may be found in various crystal structures [2,37,38], lipid-containing systems [39–42], microemulsions [43], block copolymers [44–57], skeletal elements in sea urchins [58,59] and cell membranes [60].

A TPMS is either free of self-intersections or may intersect itself in a more or less complicated way. Each TPMS without self-intersections is two-sided and subdivides $\mathbb{R}^3$ into two infinite, connected but disjunct regions. These two regions, or labyrinths, are not simply connected and they interpenetrate each other in a complicated way. The two labyrinths may differ in shape or they may be congruent, i.e. there exist symmetry operations mapping one labyrinth onto the other. In the latter case the surface is called a balance surface [61]. The symmetry of a balance surface is described by a group–subgroup pair $\mathscr{H}/\mathscr{I}$ of spacegroups, where $\mathscr{H}$ contains all isometries of $\mathbb{R}^3$ which map the surface onto itself. An isometry of $\mathscr{H}$ maps each side of the surface and each labyrinth either onto itself or onto the other side and the other labyrinth [61]. $\mathscr{I}$ contains only those isometries which map each side of the surface and each labyrinth onto itself. If the two sides of

a balance surface are "colored" so that they are symmetrically distinct, black–white space groups instead of the group-subgroup pairs with index 2 may be used to describe its symmetry [61]. In this case the surface is called oriented.

The periodic surfaces can be divided into equivalent regions bounded by a unit cell of space. There are two common choices of unit cells, the lattice fundamental region and the crystallographic cell [62]. The lattice fundamental region contains the smallest region of the surface that reproduces the complete surface upon translation of this unit cell alone. The crystallographic cell is the smallest cube generating space by the lattice and can contain many lattice fundamental regions. We give our data for the crystallographic cell, simply called the unit cell from now on, and consider the bicontinuous structure of total volume L^3 to be composed of several unit cells of typical length scale L_0. Then the Minkowski functionals for one elementary unit may be calculated from (38) and (39).

Here we only consider the P (primitive) [63] the D (diamond) [63] and the G (gyroid) [64] surfaces, which are TPMS free of self-intersections. The P, D and G surfaces, with group-subgroup pairs of space groups with index 2 $Im\bar{3}m/Pm\bar{3}m$, $Pn\bar{3}m/Fd\bar{3}m$ and $Ia\bar{3}d/I4_132$, respectively, divide space into two equal labyrinths related by a translation (for P and D) or an inversion (for G), thereby generating a bicontinuous geometry. The Bravais lattices for the P, D, and G surfaces are BCC, SC and BCC, respectively. For the oriented P, D and G surfaces the Bravais lattices are SC, FCC and BCC, respectively.

The oriented P, D and G surfaces may be approximated by the periodic nodal surfaces [65–67]

$$\cos x + \cos y + \cos z = 0 \,, \tag{43a}$$

$$\sin x \sin y \sin z + \sin x \cos y \cos z + \cos x \sin y \cos z + \cos x \cos y \sin z = 0 \,, \tag{43b}$$

$$\sin x \cos y + \sin y \cos z + \sin z \cos x = 0 \,. \tag{43c}$$

In Fig. 21a–c we show the nodal P (43a), D (43b) and G (43c) surfaces, in their unit cell. Tables 4–6, summarize the results for the Minkowski functionals of the thresholded nodal oriented P, D and G surfaces for several numbers of unit cells. As seen from Tables 4–6, the values calculated using the integral-geometry approach are in good agreement with the numbers found in literature [62,68,69]. Note that in contrast to many works in literature, we compute $\chi(\mathscr{P})$ and not $\chi(\partial\mathscr{P}) = 2\chi(\mathscr{P})$ (see also

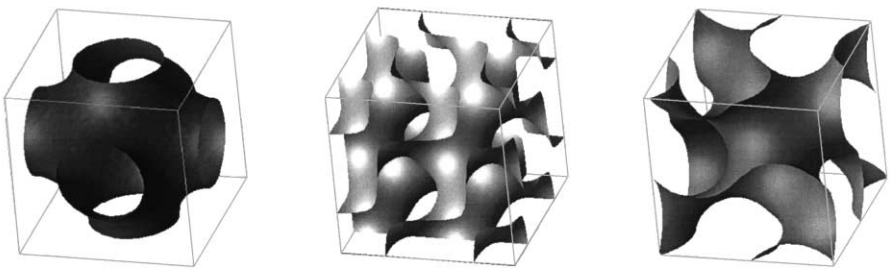

Fig. 21. Unit cube for the nodal primitive P surface (a), the nodal double diamond D surface (b) and the nodal gyroid G surface (c). The surfaces are generated from Eq. (43).

Table 4
Minkowski functionals of the P surface (at threshold $q = 0.5$) obtained from (43a) for $M = (L/L_0)^3$ unit cells, where L denotes the edge length of the total cube and L_0 the edge length of a unit cube. The values found in the literature [62,68,69] are given in parenthesis

L_0	L	M	$\bar{V}$	$\bar{S}$	$\bar{\chi}$
16	64	64	0.502	3.800	−2
32	64	8	0.501	3.715	−2
32	128	64	0.501	3.715	−2
64	64	1	0.501	3.671	−2
64	128	8	0.500	3.671	−2
128	128	1	0.500	3.675	−2
			(0.500)	(2.345)	(−2)

Table 5
Minkowski functionals of the D surface (at threshold $q = 0.5$) obtained from (43b) for $M = (L/L_0)^3$ unit cells, where L denotes the edge length of the total cube and L_0 the edge length of a unit cube. The values found in the literature [62,68,69] are given in parenthesis

L_0	L	M	$\bar{V}$	$\bar{S}$	$\bar{\chi}$
16	64	64	0.500	6.000	−8
32	64	8	0.500	6.000	−8
32	128	64	0.500	6.000	−8
64	64	1	0.500	6.000	−8
64	128	8	0.500	6.000	−8
128	128	1	0.500	6.000	−8
			(0.500)	(3.838)	(−8)

Table 6
Minkowski functionals properties of the G surface (at threshold $q = 0.5$) obtained from (43c) for $M = (L/L_0)^3$ unit cells, where L denotes the edge length of the total cube and L_0 the edge length of a unit cube. The values found in the literature [62,68,69] are given in parenthesis

L_0	L	M	$\bar{V}$	$\bar{S}$	$\bar{\chi}$
16	64	64	0.500	4.970	−4
32	64	8	0.500	4.900	−4
32	128	64	0.500	4.900	−4
64	64	1	0.500	4.857	−4
64	128	8	0.500	4.857	−4
128	128	1	0.500	4.847	−4
			(0.500)	(3.092)	(−4)

Section 5.4). Only the numbers for the area are about a factor of 1.6 larger than the numbers quoted in literature. This systematic error is due to the digitization of the picture. This operation transforms the smooth surface to a more stepwise surface which enlarges the covered area.

Table 7
Corrected digital volume and covered area of the P, D and G surfaces (at threshold $q = 0.5$) obtained from (43a) to (43c) for one unit cell with edge length $L_0 = 128$. The Euclidean values found in the literature [62,68,69] are given in parenthesis

TPMS	$\bar{V}'$	$\bar{S}'$
P	0.481 (0.500)	2.204 (2.345)
D	0.470 (0.500)	3.782 (3.839)
G	0.474 (0.500)	2.916 (3.092)

Table 8
Digital (HI) and corrected digital (HI') homogeneity index of the P, D, and G surfaces (at threshold $q = 0.5$) obtained from (43a) to (43c) for one unit cell with edge length $L_0 = 128$. The Euclidean values found in the literature [70] are given in the last column

TPMS	HI	HI'	Ref. [70]
P	1.4053	0.6527	0.7163
D	1.4658	0.7336	0.7498
G	1.5051	0.7023	0.7667

In Table 7 we show the results of using the method described in Section 5.6 to reduce this error. The results are for one unit cell and $L_0 = 128$. As seen from Table 7 the numbers for the volume and the covered area are now about a factor 0.94–0.98 smaller than the numbers quoted in literature [62,68,69]. Hence for the examples shown in this section the method described in Section 5.6 underestimates the Euclidean volume and covered area.

From Tables 4–7 the values for the non-oriented surfaces may be obtained using the following relationships [62]: (i) one unit cell of the oriented P, D and G surfaces contains one, eight and one unit cell(s) of the non-oriented P, D and G surfaces, respectively; (ii) the area numbers of the oriented surfaces must be multiplied by a factor of 2 in the case of the P and G surface and a factor of 1 in the case of the D surface to obtain the area numbers for the non-oriented surfaces.

A useful dimensionless measure of the surface of bicontinuous structures is the homogeneity index HI defined as [69]

$$HI = \sqrt{\frac{-\bar{S}^3}{4\pi\bar{\chi}}} \ . \tag{44}$$

A discussion of other dimensionless quantities can be found in [62]. For "homogeneous" minimal surfaces for which the Gaussian curvature is constant everywhere on the surface, $HI = 0.75$ [70]. The TPMS have homogeneity indices close to 0.75: $HI = 0.7163$ for the P-surface, $HI = 0.7498$ for the D-surface and $HI = 0.7667$ for the G-surface [70]. The values for HI for the TPMS mapped on a cubic grid, as calculated using the method described in Section 5.5 are given in the second column of Table 8. The results are for one unit cell of edge length $L_0 = 128$. The third column of Table 8 shows the results if we use the correction method described in Section 5.6 to calculate HI'. These values are much closer to the Euclidean ones found in the literature [70] (see last column of Table 8).

In summary: Integral-geometry MIA is a convenient tool to characterize the morphological properties of complex surfaces such as the TPMS. In particular, to study the topology of the TPMS, MIA does not require the use of labyrinth graphs or surface tilings [71].

6.3. Klein bottle

The Klein bottle is a well-known non-orientable (see Section 6.2) surface in algebraic topology. It is obtained if two holes cut in the sphere are closed up with Möbius bands (closed circular strip with a twist) or if two Möbius bands are pasted together along their boundaries [72]. The Klein bottle is a single-sided bottle without boundary. A real Klein bottle cannot exist in 3D since the surface has to pass through itself without a hole, but it can be immersed in 3D. The parametric equation is given by

$$x = \tfrac{1}{18}(3\sin 2t + 4)\sin s\sqrt{\sin^2 t + \tfrac{1}{4}\cos^2 t(4\cos^2 t - 3)^2}\,, \tag{45a}$$

$$y = -\cos^3 t \sin t + \tfrac{1}{18}(3\sin 2t + 4)\sin t\cos s\,, \tag{45b}$$

$$z = \cos^2 t + \tfrac{1}{36}(3\sin 2t + 4)(4\cos^2 t - 3)\cos t\cos s \tag{45c}$$

with $t = 0,\ldots,\pi$ and $s = 0,\ldots,2\pi$. Some pictures of a Klein bottle are given in Fig. 22. The surface of the Klein bottle looks rough and steplike due to the digitization process. The Klein bottle has

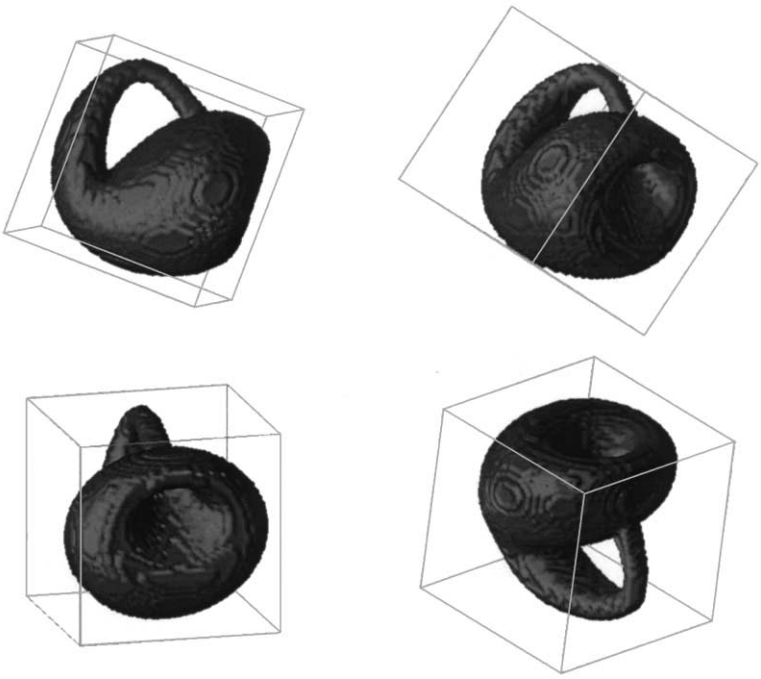

Fig. 22. Various orientations of the digitized Klein bottle.

Euler characteristic zero [72]. If we study the topology of the Klein bottle by means of MIA we also find $\chi = 0$. This demonstrates once more that MIA is a fast, reliable and convenient tool to study the topology of weird surfaces. In the following two sections we present examples that show that MIA does not loose these attractive properties when we analyze much more complex patterns.

7. Random point sets

We consider a collection of N points p_i, with positions generated from a uniformly uncorrelated random distribution, in a convex domain $\Omega \subset \mathbb{R}^d$. The mean density of points equals $\rho = N/|\Omega|$, where $|\Omega|$ denotes the volume of Ω. We attach to every point p_i (germ) a grain $A_i \in \mathscr{R}$. A configuration of the grains A_i gives rise to a set $\mathscr{A}_N \in \mathscr{R}$

$$\mathscr{A}_N = \bigcup_{i=1}^{N} g_i A_i \ , \tag{46}$$

where $g_i \in \mathscr{G}$, under the assumption that the translations are restricted to Ω. This random distribution of grains includes the Boolean model [25], a basic model in stereology and stochastic geometry [9,10].

We are interested in the mean values of the normalized Minkowski functionals of $\mathscr{A}_N$. In the bulk limit $N, \Omega \to \infty$, $\rho = N/|\Omega|$ fixed, the averages $\langle M_\nu/N\rangle_N$, $\nu = 0, \ldots, d$, with the notation $M_\nu \equiv M_\nu^{(d)}$, are known exactly [11,73,74] and are given by

$$\langle M_0/N\rangle_N = (1 - \mathrm{e}^{-\rho m_0})/\rho \ , \tag{47a}$$

$$\langle M_1/N\rangle_N = m_1 \mathrm{e}^{-\rho m_0} \ , \tag{47b}$$

$$\langle M_2/N\rangle_N = (m_2 - m_1^2\rho)\mathrm{e}^{-\rho m_0} \ , \tag{47c}$$

$$\langle M_3/N\rangle_N = (m_3 - 3m_1 m_2 \rho + m_1^3\rho^2)\mathrm{e}^{-\rho m_0} \ , \tag{47d}$$

where $\langle M_\nu\rangle_N$ denote the average of the Minkowski functionals of the ensemble with density ρ and m_ν denote the mean values of the Minkowski functionals of a single grain. In Appendix D we give a derivation of (47) which differs from the one given in [11] in that no use is made of the so-called Minkowski polynomials [74].

On a regular d-dimensional lattice it is more natural to work with hypercubes instead of digital approximations of the corresponding Euclidean shapes. This suggests the construction of a genuine discrete integral geometry, without making reference to Euclidean space. We therefore consider a collection of N pixels p_i in a hypercubic domain $\Omega \subset \mathbb{R}^d$ of volume $|\Omega| = L_x^d$. The positions of the pixels are generated from a uniformly uncorrelated random distribution. The mean density of pixels equals $\rho = N/|\Omega|$. We attach to every germ p_i a hypercubic grain C_i. In the bulk limit N, $\Omega \to \infty$ with ρ fixed, the averages of the morphological quantities of the ensemble of configurations of the hypercubic grains C_i are still given by (47) but the explicit expressions for M_ν and m_ν, $\nu = 0, \ldots, d$ are different from those in Euclidean space [75].

7.1. Two dimensions

In 2D Euclidean space and in the bulk limit (47) yields

$$\langle A(\rho)/N\rangle_N = \langle \tilde{A}(\rho)\rangle/\rho = (1 - \mathrm{e}^{-\rho a})/\rho \,, \tag{48a}$$

$$\langle U(\rho)/N\rangle_N = \langle \tilde{U}(\rho)\rangle/\rho^{1/2} = u\mathrm{e}^{-\rho a} \,, \tag{48b}$$

$$\langle \chi(\rho)/N\rangle_N = \langle \tilde{\chi}(\rho)\rangle = \left(1 - \frac{1}{4\pi}u^2\rho\right)\mathrm{e}^{-\rho a} \,, \tag{48c}$$

where we made use of (29b) and (37a) and where a and u denote the mean values of the area and perimeter of a single grain. The Euler characteristic of a single grain equals one. In the case that the grains are circular discs of radius r, we substitute in (48) $a = \pi r^2$ and $u = 2\pi r$. This leads to

$$\langle \tilde{A}\rangle = 1 - \mathrm{e}^{-n}, \quad \langle \tilde{U}\rangle = 2\pi\rho^{1/2}r\mathrm{e}^{-n}, \quad \langle \tilde{\chi}\rangle = (1 - n)\mathrm{e}^{-n} \tag{49}$$

with $n = \pi r^2\rho$.

As we are working on a square lattice anyway it might be more beneficial to use square grains (instead of discrete approximations to circular discs) to study the morphological properties of random point sets and to make no reference to Euclidean space at all. Then we can still use (47) but we need expressions for the normalized Minkowski functionals on a lattice, analogous to the Euclidean ones given in (29b). In analogy with Sections 5.1 and 5.2 on a square lattice the area of a square C_ε, parallel to a square C of edge length a at a distance ε is given by

$$\begin{aligned} A(C_\varepsilon) &= (a + 2\varepsilon)^2 = a^2 + 4a\varepsilon + 4\varepsilon^2 \\ &= A_c(C) + U_c(C)\varepsilon + 4\chi_c(C)\varepsilon^2 \,, \end{aligned} \tag{50}$$

where $A_c(C) = a^2$, $U_c(C) = 4a$ and $\chi_c(C) = 1$. Using Steiner's formula (20) and substituting for ω_d the volume of the unit cube in d dimensions (i.e. $\omega_d = 1$) we find that

$$M_0 = A_c, \quad M_1 = S_c/2, \quad M_2 = 4\chi_c \,. \tag{51}$$

Finally using (47) we obtain

$$\langle \tilde{A}_c\rangle = 1 - \mathrm{e}^{-n}, \quad \langle \tilde{U}_c\rangle = 4a\rho^{1/2}\mathrm{e}^{-n}, \quad \langle \tilde{\chi}_c\rangle = (1 - n)\mathrm{e}^{-n} \tag{52}$$

with $n = \rho a^2$.

We adopt the procedure outlined in Section 2.3 to compute the morphological properties of a uniform random distribution of points in a square of edge length L with periodic boundaries. First, we transform the point pattern into a pattern of disc-like grains of radius r and then investigate the behavior of the Minkowski functionals as a function of r.

The solid lines in Fig. 23 show $\tilde{A}$, $\tilde{U}$ and $\tilde{\chi}$ as a function of r for a single realization of $N = 10\,240$ pixels on a square lattice of linear size $L = 1024$, subject to periodic boundary conditions. For small r the disc-like grains are isolated. This gives rise to a small covered area, perimeter and to a positive Euler characteristic. For large r the discs cover almost completely the whole square leading to a large covered area, a small perimeter and a negative Euler characteristic which approaches zero in the case of the completely covered square. For intermediate r, the coverage has a net-like structure with a negative Euler characteristic and a large perimeter. The dotted lines in

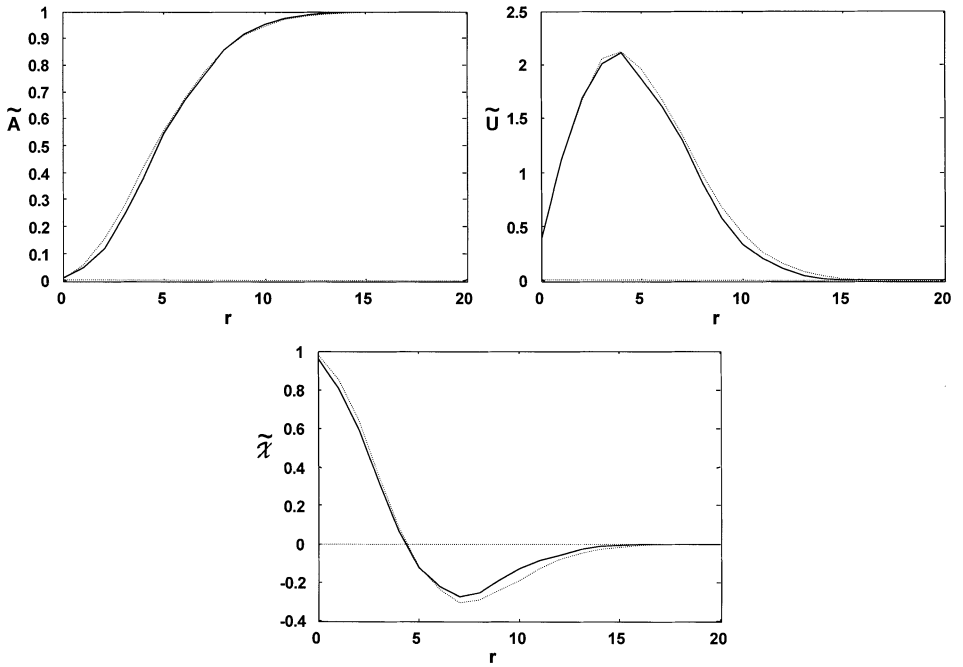

Fig. 23. Minkowski functionals as a function of r for random point sets with "disc-like" grains, using periodic boundary conditions. Solid lines: 10 240 points in a square of edge length 1024; dotted lines: fit to data, using the expressions given by (53).

Fig. 23 are the results obtained by fitting

$$\langle \tilde{A}_{\mathrm{F}} \rangle = 1 - \mathrm{e}^{-n}, \quad \langle \tilde{U}_{\mathrm{F}} \rangle = u\mathrm{e}^{-n}, \quad \langle \tilde{\chi}_{\mathrm{F}} \rangle = (1 - f_3 u^2 \rho/4\pi)\mathrm{e}^{-n}\,, \tag{53}$$

to data with $n = \pi\rho f_1 r^2$ and $u = 2\pi f_2 r$. The functional behavior of $\tilde{A}_{\mathrm{F}}$, $\tilde{U}_{\mathrm{F}}$ and $\tilde{\chi}_{\mathrm{F}}$ is chosen to be the same as for grains that are circular discs in Euclidean space. The fitting parameters f_1, f_2 and f_3 have been introduced to take into account that in practice we are working on a square lattice and are approximating circular discs by discrete structures. We find $f_1 = 0.22$, $f_2 = 0.66$ and $f_3 = 0.80$ for the dotted line by fitting the solid line.

If we use square grains instead of disc-like grains we obtain the results shown in Fig. 24 (solid line). The dotted lines are the results obtained from (52). As seen from Fig. 24 the agreement between the data and the theoretical result (52) is excellent. Note the absence in (52) of any adjustable parameter.

7.2. Three dimensions

In 3D and in the bulk limit we find [14]

$$\langle V(\rho)/N \rangle_N = \langle \tilde{V}(\rho) \rangle/\rho = (1 - \mathrm{e}^{-\rho v})/\rho\,, \tag{54a}$$

$$\langle S(\rho)/N \rangle_N = \langle \tilde{S}(\rho) \rangle/\rho^{2/3} = s\mathrm{e}^{-\rho v}\,, \tag{54b}$$

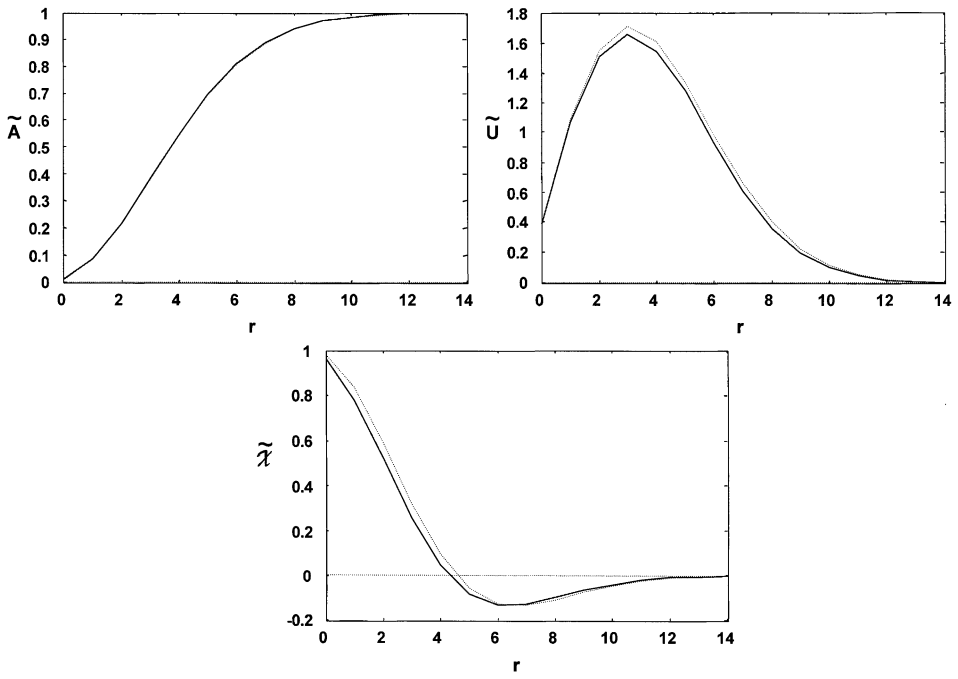

Fig. 24. Minkowski functionals as a function of r for a random point set with square grains, using periodic boundary conditions. Solid lines: 10 240 points in a square of edge length 1024; dotted lines: results obtained from discrete integral geometry (see (52)), without fitting.

$$\langle B(\rho)/N\rangle_N = \langle \tilde{B}(\rho)\rangle/2\rho^{1/3} = b\left(1 - \frac{\pi}{64}\frac{s^2}{b}\rho\right)e^{-\rho v}\,, \tag{54c}$$

$$\langle \chi(\rho)/N\rangle_N = \langle \tilde{\chi}(\rho)\rangle = \left(1 - \frac{1}{2}sb\rho + \frac{\pi}{384}s^3\rho^2\right)e^{-\rho v}\,, \tag{54d}$$

where use has been made of (29c) and (37b) for $d = 3$ and where $\langle \tilde{V}(\rho)\rangle$, $\langle \tilde{S}(\rho)\rangle$, $\langle \tilde{B}(\rho)\rangle$ and $\langle \tilde{\chi}(\rho)\rangle$ denote the mean values of the volume, area, mean breadth and Euler characteristic of the ensemble with density ρ. The mean values of the volume, area and mean breadth of a single grain are denoted by v, s and b, respectively. The Euler characteristic of a single grain equals one.

The mean values of the Minkowski functionals depend on the shape of the single grains. If the grains are spheres of radius r we substitute in (54) $v = 4\pi r^3/3$, $s = 4\pi r^2$ and $b = 2r$. This leads to

$$\langle \tilde{V}\rangle = 1 - e^{-n}\,, \tag{55a}$$

$$\langle \tilde{S}\rangle = 4\pi\rho^{2/3}r^2e^{-n}\,, \tag{55b}$$

$$\langle \tilde{B}\rangle = 4\rho^{1/3}r\left(1 - \frac{3\pi^2}{32}n\right)e^{-n}\,, \tag{55c}$$

$$\langle \tilde{\chi}\rangle = \left(1 - 3n + \frac{3\pi^2}{32}n^2\right)e^{-n} \tag{55d}$$

with $n = 4\pi r^3\rho/3$.

We now consider the case that the grains are cubes on a regular 3D lattice. In analogy to the 2D case we first compute the volume of the cube C_ε parallel to a cube C of edge length a at a distance ε

$$V(C_\varepsilon) = (a + 2\varepsilon)^3 \,, \tag{56a}$$

$$= V_c(C) + S_c(C)\varepsilon + 8B_c(C)\varepsilon^2 + 8\chi_c(C)\varepsilon^3 \,, \tag{56b}$$

where $V_c(C) = a^3$, $S_c(C) = 6a^2$, $B_c(C) = 3a/2$ and $\chi_c(C) = 1$. Then by using the Steiner formula (20) and substituting $\omega_d = 1$ we find that

$$M_0 = V_c, \quad M_1 = S_c/3, \quad M_2 = 8B_c/3, \quad M_3 = 8\chi_c \,. \tag{57}$$

Finally, using (47) we obtain

$$\langle \tilde{V}_c \rangle = 1 - \mathrm{e}^{-n} \,, \tag{58a}$$

$$\langle \tilde{S}_c \rangle = 6a^2\rho^{2/3}\mathrm{e}^{-n} \,, \tag{58b}$$

$$\langle \tilde{B}_c \rangle = 3a\rho^{1/3}(1 - n)\mathrm{e}^{-n} \,, \tag{58c}$$

$$\langle \tilde{\chi}_c \rangle = (1 - 3n + n^2)\mathrm{e}^{-n} \tag{58d}$$

with $n = \rho v = \rho a^3$. Note the absence in (58) of any adjustable parameter.

We will now study the Minkowski functionals for sets of points which are randomly positioned in a cube of edge length L subject to periodic boundaries. Again we follow the procedure described in Section 2.3: We transform the point pattern into a pattern of "spherical" grains of radius r and study the behavior of the Minkowski functionals as a function of r. Fig. 25 shows the Minkowski functionals $\tilde{V}$, $\tilde{S}$, $\tilde{B}$ and $\tilde{\chi}$ as a function of r for one single configuration of a random point set with fixed density $\rho = N/L^3 \approx 0.00049$ and various system sizes ($N = 1024$, $L = 128$: dotted line, $N = 128$, $L = 64$: solid line and $N = 16$, $L = 32$: dashed line). The curves for the various system sizes show only minor quantitative differences, as could be expected from (55). For small r the grains are isolated leading to a small covered volume and surface area and to a positive Euler characteristic. For large r the grains largely overlap and cover almost completely the whole cube. Only small cavities remain. This gives rise to a large covered volume, a small surface area and a positive Euler characteristic which approaches zero in the case of the completely covered cube. For intermediate r the coverage has a tunnel-like structure with a negative Euler characteristic and a large surface area.

In Fig. 26 we depict the Minkowski functionals as a function of r for two random point sets with $L = 128$ and different density. The solid (dashed) lines show the data for $N = 1024$ ($N = 512$). For both cases the behavior of the Minkowski functionals as a function of r is very similar: The curves show the same qualitative behavior (the grains have the same shape in both cases) and are only shifted with respect to each other. The dash–dotted ($N = 1024$) and dotted ($N = 512$) lines in Fig. 26 are the results obtained by fitting

$$\langle \tilde{V}_\mathrm{F} \rangle = 1 - \mathrm{e}^{-n} \,, \tag{59a}$$

$$\langle \tilde{S}_\mathrm{F} \rangle = s\rho^{2/3}\mathrm{e}^{-n} \,, \tag{59b}$$

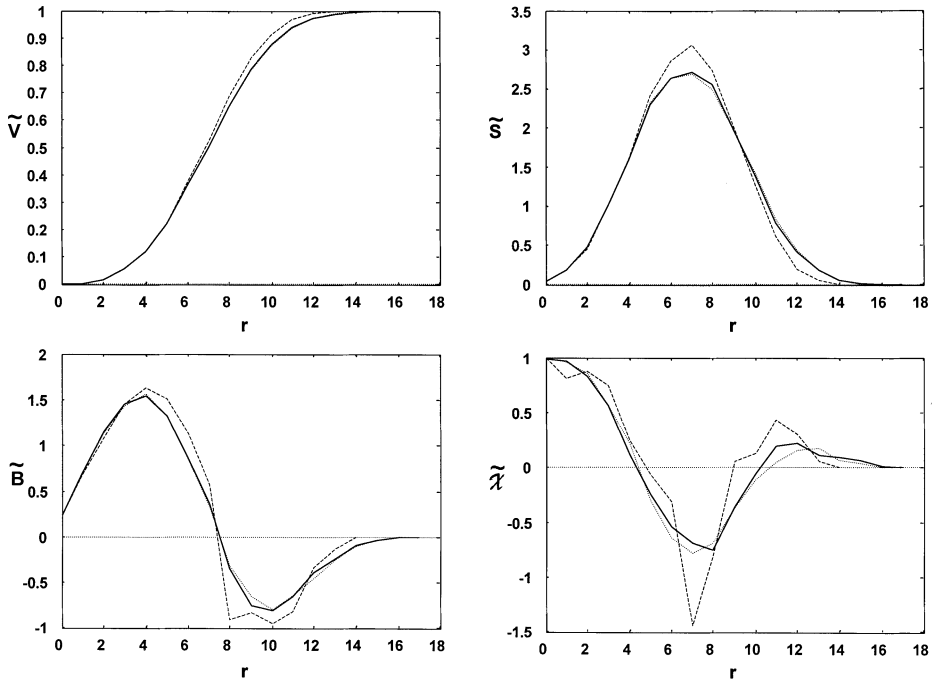

Fig. 25. Minkowski functionals as a function of r for random point sets with "spherical" grains, using periodic boundary conditions. Dotted line: 1024 points in a cubic box of edge length 128; solid line: 128 points in a cubic box of edge length 64; dashed line: 16 points in a cubic box of edge length 32.

$$\langle \tilde{B}_{\mathrm{F}} \rangle = 2\left(b - \frac{\pi \rho s^2}{64} \right) \rho^{1/3} \mathrm{e}^{-n}, \tag{59c}$$

$$\langle \tilde{\chi}_{\mathrm{F}} \rangle = \left(1 - \frac{\rho s b}{2} f_4 + \frac{\pi \rho^2 s^3}{384} f_5 \right) \mathrm{e}^{-n} \tag{59d}$$

to the data with $n = 4\pi\rho f_1 r^3/3$, $s = 4\pi f_2 r^2$ and $b = 2f_3 r$. The functional behavior of $\tilde{V}_{\mathrm{F}}$, $\tilde{S}_{\mathrm{F}}$, $\tilde{B}_{\mathrm{F}}$ and $\tilde{\chi}_{\mathrm{F}}$ is chosen to be the same as for perfect spherical grains in the Euclidean space. The fitting parameters $f_1, \ldots, f_5$ have been introduced to take into account that in practice we are working on a lattice and are approximating spheres by discrete structures. We find for $N = 512$ and 1024, $f_1 = 0.108$, $f_2 = 0.32$, $f_3 = 0.8$, $f_4 = 0.72$ and $f_5 = 0.77$ for the dash–dotted (dotted) line by fitting the solid (dashed) line.

In Fig. 27 we show the Minkowski functionals for the same random set of points (solid lines) as the one used for Fig. 26 ($L = 128$, $N = 1024$) but we now used cubic instead of "spherical" grains. The cubic grains have edge length $a = 2r + 1$, $r > 0$. The dotted lines are the results obtained from (58). As in two dimensions also in 3D there is excellent agreement between the numerical data and the theoretical result (58). Note that the agreement is remarkable as only one realization of a random point set was used in the simulation. The excellent agreement between the data and the theoretical result (58) suggests that it is more natural indeed to analyze polyhedral sets on regular lattices in terms of discrete integral geometry.

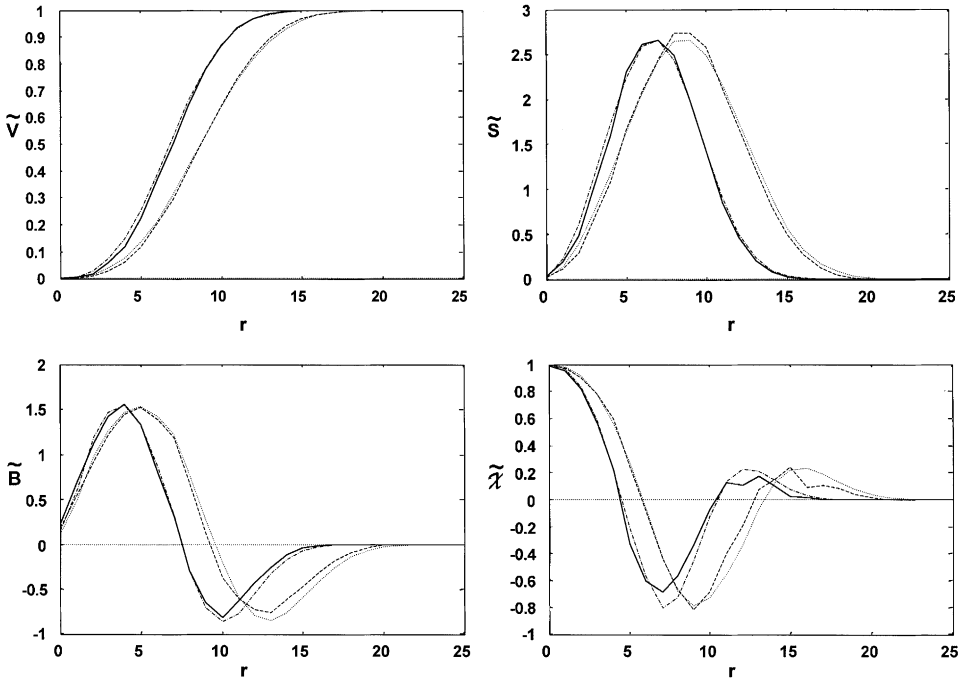

Fig. 26. Minkowski functionals as a function of r for random point sets with "spherical" grains, using periodic boundary conditions. Solid lines: 1024 points in a cubic box of edge length 128; dash–dotted lines: fit to 1024-point data, using the expressions given by (59); dashed lines: 512 points in a cubic box of edge length 128; dotted lines: fit to 512-point data, using the expressions given by (59).

7.3. Percolation

Consider a square lattice of linear dimension L of which a certain fraction of squares (sites) is colored black, whereas the others are colored white. We assume that the sites are colored randomly, that is each site is colored black or white independent of the color of its neighbors. We call p $(0 \leq p \leq 1)$ the probability of a site being colored black. Hence, the average number of black sites is given by pL^2 and the average number of white ones by $(1-p)L^2$. Black pixels can be grouped into clusters: Two black pixels belong to the same cluster if they are nearest neighbors or can be connected by a chain of black pixels that are nearest neighbors (note that a "cluster" is not the same as an "object", see Section 3.1). Percolation theory deals with the number and geometric properties of these clusters. The origin of the mathematical theory of percolation goes back to a publication by Broadbent and Hammersley [76]. Since percolation processes and their applications have been discussed by so many authors we can only make reference to a few books which give a general introduction to percolation theory, deal extensively with its mathematical aspects, give applications and/or give an extensive bibliography [77–81]. From percolation theory it is known that for infinite square lattices there exists a critical value p_c, the percolation threshold, such that all clusters are finite when $p < p_c$, but there exists an infinite cluster when $p > p_c$. The latter

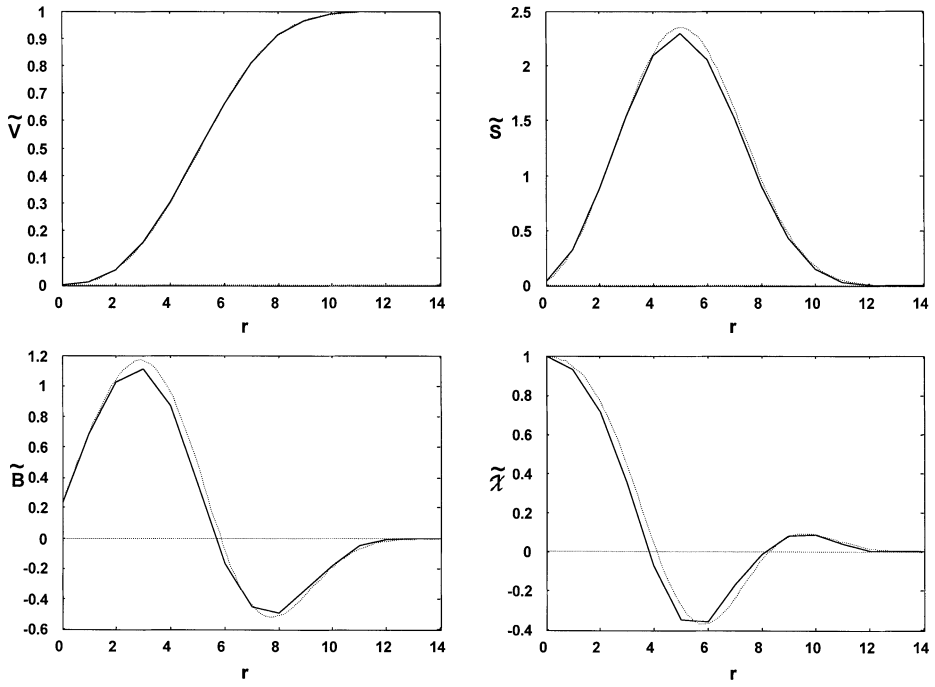

Fig. 27. Minkowski functionals as a function of r for a random point set with cubic grains, using periodic boundary conditions. Solid lines: 1024 points in a cubic box of edge length 128; dotted lines: results obtained from discrete integral geometry (see (58)), without fitting.

cluster is called a percolation cluster since it percolates through the system like water percolates through a porous stone.

There are two distinct types of percolation problems. An example of a site percolation problem (as the one described above) is shown in Fig. 28a. The clusters are encircled. Another type of percolation process is bond percolation, in which the edges rather than the sites are colored black or white at random. A cluster is then a group of sites connected by black bonds. An example of bond percolation is shown in Fig. 28b. It is well known that every bond model may be reformulated as a site model on a different lattice, but not vice versa.

One of the interesting problems in percolation theory is the determination of the value of the percolation threshold p_c. This value depends on the percolation problem studied and on the lattice type (including its dimensionality). The percolation threshold p_c, defined as the concentration at which an infinite cluster appears in the infinite lattice, for site percolation on the square lattice is not known exactly. Several authors have given (rigorous) upper and lower bounds [82–88]

$$0.556 < p_c < 0.679492 \,. \tag{60}$$

Computer evaluations of the percolation threshold give the estimate [89,90] $p_c = 0.5927460$. It is also known that $p_c = 1/2$ for site percolation on the infinite triangular lattice. For bond percolation on the infinite square lattice $p_c = 1/2$, as suggested by Sykes and Essam [91], and proven rigorously by Kesten [92]. For the bond problem on the triangular lattice and honeycomb lattice

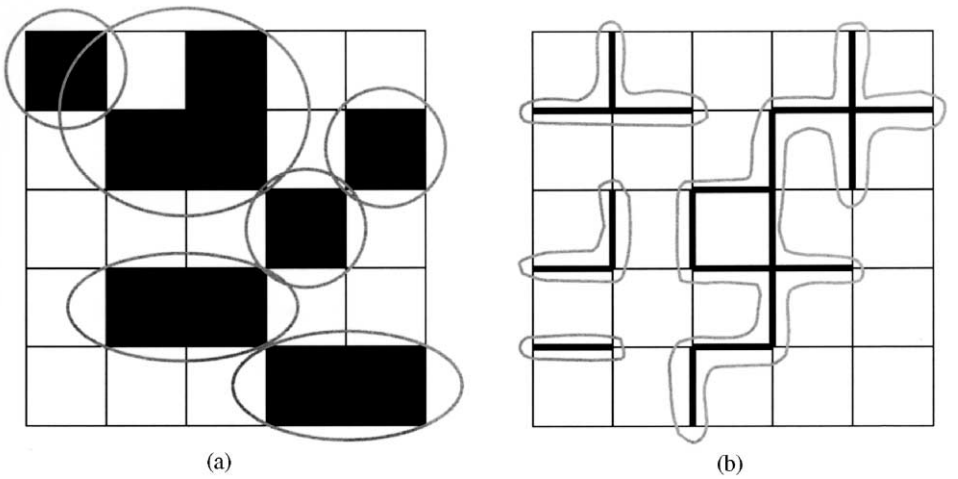

Fig. 28. Percolation problems on a square lattice: (a) site percolation problem (nearest neighbor), (b) bond percolation problem. The clusters are encircled.

Sykes and Essam proposed that $p_c = 2\sin(\pi/18)$, and $p_c = 1 - 2\sin(\pi/18)$, respectively [91]. Rigorous proofs of these conjectured values are given by Wierman [93].

In the remainder of this section we will consider only the site percolation problem on a square or cubic lattice. Clearly, this is yet another example of a random point (or pixel) set. We consider a square (cubic) lattice of which a certain fraction of squares (cubes), with positions generated from a uniformly uncorrelated random distribution, is colored black. The probability of a site being colored black is p ($0 \leq p \leq 1$). In Fig. 29 (30) we show the Euler characteristic $\tilde{\chi}$ as a function of p (diamonds) for a 2D (3D) square (cubic) lattice with periodic boundaries and linear dimension $L = 512$ ($L = 64$). In 2D (see Fig. 29), $\tilde{\chi}(p)$ is positive and increases with p for small p. At some value of p, $\tilde{\chi}(p)$ starts decreasing and becomes negative. $\tilde{\chi}(p) = 0$ at $p \approx 0.39$. For large p, $\tilde{\chi}(p)$ starts increasing again and becomes zero for the completely covered square (periodic boundaries). In 3D (see Fig. 30), the behavior of $\tilde{\chi}$ as a function of p is similar but $\tilde{\chi}(p)$ has one more change of sign: $\tilde{\chi} = 0$ at $p_1 \approx 0.16$ and $p_2 \approx 0.61$.

Intuitively, one would think one could use the Euler characteristic to define percolation [11,14,94–96]. Namely in 2D the Euler characteristic χ is defined as the number of connected components (objects) minus the number of holes. In the case of site percolation, one then expects χ to be positive and equal to p for small p while for large p one expects χ to be negative. The question then arises when one can relate the change of sign of χ to the percolation threshold.

Calculation of the Euler characteristic of a pattern of active (here considered to be black) pixels requires the consideration of both the nearest and next-nearest neighbors of the active pixels and the nearest neighbors of inactive (white) pixels only (see also Section 3.1). In 2D we may write

$$\tilde{\chi}^{\star}_{\mathrm{B}}(p) = N^{\star}_{\mathrm{B}}(p) - N_{\mathrm{W}}(p)\,, \tag{61}$$

where N_{W} ($N^{\star}_{\mathrm{B}}$) denotes the mean number of white (black) objects on the simple quadratic lattice with nearest (and next-nearest) neighbors. The distinction between both lattices (*Lat* and *Lat**) is

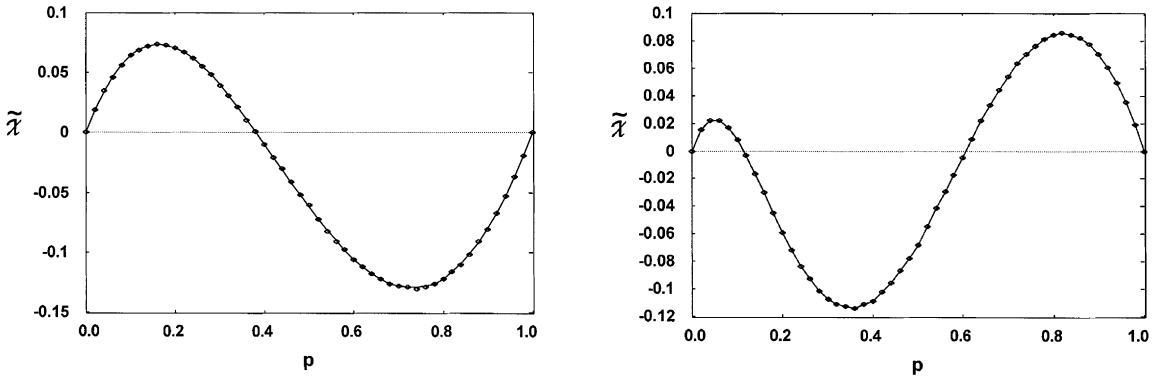

Fig. 29. Percolation on a 2D square lattice with periodic boundaries ($L = 512$). Diamonds: Euler characteristic as a function of p; solid line: matching polynomial.

Fig. 30. Percolation on a 3D cubic lattice with periodic boundaries ($L = 64$). Diamonds: Euler characteristic as a function of p. The solid line is a guide to the eyes.

denoted by the star. *Lat* and *Lat** form a matching pair of lattices [91]. Note that all Euler characteristics computed in this work are, in fact, calculated on *Lat** and should for reasons of consistency have been denoted by $\chi^\star$. However, for the sake of clarity we have omitted the $\star$ in all sections except this one. According to Sykes and Essam [91], at density p the mean number of black (white) clusters on the simple quadratic lattice with nearest neighbors $N_{\mathrm{B}}(p)$ [$N_{\mathrm{W}}(p)$] differs from the mean number of white (black) clusters on the simple quadratic lattice with nearest and next-nearest neighbors $N^\star_{\mathrm{W}}(p)$ [$N^\star_{\mathrm{B}}(p)$] by $\phi(p)$ [$-\phi^\star(p)$]. Or in other words

$$N_{\mathrm{B}}(p) = N^\star_{\mathrm{W}}(p) + \phi(p)\,, \tag{62a}$$

$$N_{\mathrm{W}}(p) = N^\star_{\mathrm{B}}(p) - \phi^\star(p)\,, \tag{62b}$$

where

$$\phi(p) = p - 2p^2 + p^4\,, \tag{63a}$$

$$\phi^\star(p) = p - 4p^2 + 4p^3 - p^4\,, \tag{63b}$$

are called the matching polynomials [91]. Property (62) is called cross-matching. From (61) and (62b) it follows that

$$\tilde{\chi}^\star_{\mathrm{B}}(p) = \phi^\star(p)\,, \tag{64}$$

i.e. in 2D the matching polynomial coincides with the Euler characteristic [94]. As can be seen from Fig. 29, where we plot the Euler characteristic (diamonds) and the matching polynomial $\phi^\star(p)$ (solid line) as a function of p, our numerical results are in perfect agreement with (64). Note that the value of p for which $\tilde{\chi}^\star_{\mathrm{B}}(p) = 0$ (i.e. $p \approx 0.39$) does not correspond to the percolation threshold $p^\star_{\mathrm{c}} \approx 0.41$ for site percolation on the square lattice with nearest and next-nearest neighbors. The property of cross-matching (62) leads to $p_{\mathrm{c}} + p^\star_{\mathrm{c}} = 1$ [91]. To determine p_{c} and $p^\star_{\mathrm{c}}$ a second relation is required.

For some cases Sykes and Essam calculated the exact values of percolation thresholds using the matching polynomials (see above) [91]. If $Lat = Lat^{\star}$ the lattice is called self-matching [91]. For self-matching lattices [91]

$$N_{\mathrm{B}}(p) = \phi(p) + N_{\mathrm{W}}(p)\ , \tag{65}$$

where

$$\phi(p) = p - 3p^2 + 2p^3\ . \tag{66}$$

The triangular lattice is an example of a self-matching lattice. For a self-matching lattice $p_{\mathrm{c}} = 1/2$ and hence, in this particular case, $\tilde{\chi}_{\mathrm{B}}(p_{\mathrm{c}}) = 0$.

8. Block copolymers

Block copolymers consist of a successive number of sequences of the same type of monomer, called blocks. The polymer block types, the composition and overall molecular size can be varied and precisely controlled [97]. AB block copolymers, for example, consist of a sequence of type A monomers covalently bonded to a chain of type B monomers.

In equilibrium AB block copolymers assemble into a variety of phases, creating domains of component A and component B. The type of domain structures that are formed is determined by three experimentally controllable factors: The overall degree of polymerization, the relative volume fraction of the A and B components, and the A–B segment–segment (Flory–Huggins) interaction parameter χ_{AB} [97]. The first two factors contribute to the entropic chain-conformational energy and the latter one to the enthalpic interaction energy. These two energies are important in the formation of interfaces in block copolymers. If the product of the overall degree of polymerization and χ_{AB} is large, narrow interfaces separate nearly pure A and B domains [97]. In this regime, the inter-material contact area is minimized under the constraint of fixed volume fraction [47]. These conditions lead to interfacial surfaces of constant mean curvature (CMC) [47]. A minimal surface, examples of which are described in Section 6.2, is a special kind of a CMC surface. The mean curvature of a minimal surface is identically zero everywhere on the surface. Such a surface minimizes the area without any volume constraint [47]. For diblock copolymers the following phases can be identified: A spherical micellar phase, a hexagonally packed cylinder phase, a lamellar phase, and a gyroidal phase [57]. Spheres and cylinders are surfaces with non-zero CMC, lamellae and gyroids are minimal surfaces. The final domain morphology determines the properties of the polymeric material and hence its end-use capabilities.

Usually, the morphology of polymer systems is studied by analyzing the structure factor obtained from scattering experiments, such as small-angle X-ray scattering (SAXS) and small-angle neutron scattering (SANS), and/or direct observation using transmission electron microscopy (TEM), scanning electron microscopy (SEM) or laser scanning confocal electron microscopy (LSCM).

Structure factors, which describe the scattering length distribution of the phase-separated structure of polymer blends, give information about the average domain size and in the case of an ordered lattice about the lattice type and the space group. To get an idea of the real 3D morphology from these data the modified Berk theory [98] has been used to analyze for example

the scattering data in bicontinuous phase-separated polymer blends and to generate the 3D morphology corresponding to the scattering data [53].

TEM and SEM micrographs are two dimensional and give information about the size, shape and connectivity of the domains. A characterization of the morphology of the underlying 3D structure might be obtained by making assumptions about the structure and comparison of the TEM or SEM images with computer generated 2D crystallographic projections of these assumed structures.

Experimentally, 3D images of the morphology of a real polymer blend can be obtained by LSCM. Similar data is also obtained from computer simulations of polymer systems. A method to estimate the mean and Gaussian curvature from 3D digital images by means of differential geometry is presented in [70]. Tools of integral and differential geometry have also been used to describe quantitatively the morphology of homopolymer blends at different spinodal decomposition stages [99].

In the following sections, we apply the method based on integral geometry and described in Section 5, to analyze 3D morphologies observed in computer simulations of various block copolymer systems.

8.1. Micellar lattices [*35*]

In "soft materials", which exhibit both temporal and spatial structural fluctuations over many length and time scales, the underlying lattice is formed under certain thermodynamic conditions and is far less rigid than the lattice of atomic crystals. The application of conventional crystallographic techniques to identify the mesostructures in these "soft" materials may be rather difficult. As an example we calculate the Minkowski functionals and the structure factor for computer-simulation data of a 50% aqueous solution of a triblock copolymer surfactant (ethylene oxide)$_{13}$(propylene oxide)$_{30}$(ethylene oxide)$_{13}$ [or (EO)$_{13}$(PO)$_{30}$(EO)$_{13}$]. The data are generated with a three-dimensional dynamic mean-field density functional method [100], a numerical method for the simulation of coarse-grained morphology dynamics in polymer liquids. The experimental [101] and simulated [102] phase diagram in the 50–70% surfactant concentration interval agree well and consist of four different phases: a micellar, an hexagonal, a bicontinuous and a lamellar phase. The orientation of the copolymers is always such that the hydrophilic ethylene oxide shields the more hydrophobic propylene oxide from contact with water. Fig. 31 shows the morphology of propylene oxide in a 50% aqueous solution of (EO)$_{13}$(PO)$_{30}$(EO)$_{13}$. The simulation box is a cube of edge length 16 (32) with periodic boundaries for the figure on the left (right). The polymer solution is micellar. Visual inspection of the pattern suggests that for a small system the micelles are organized in a BCC-like lattice. For the larger systems it is more difficult to identify the structure visually.

In order to study the Minkowski functionals as a function of r for these polymer systems we first threshold the cubic image. Then we determine the centers of the micelles in the black-and-white picture and use the same graining procedure for these centers (germs) as the one described above (see Fig. 2, left). In Fig. 32 we depict the Minkowski functionals as a function of r for the propylene oxide in the cubic simulation box of edge length 16 (solid line). For comparison we also show the Minkowski functionals for the perfect BCC lattice with $L_0 = 8$ and $M = 2$ (dashed line), for the same BCC lattice but all lattice points displaced over a randomly chosen distance 0 or

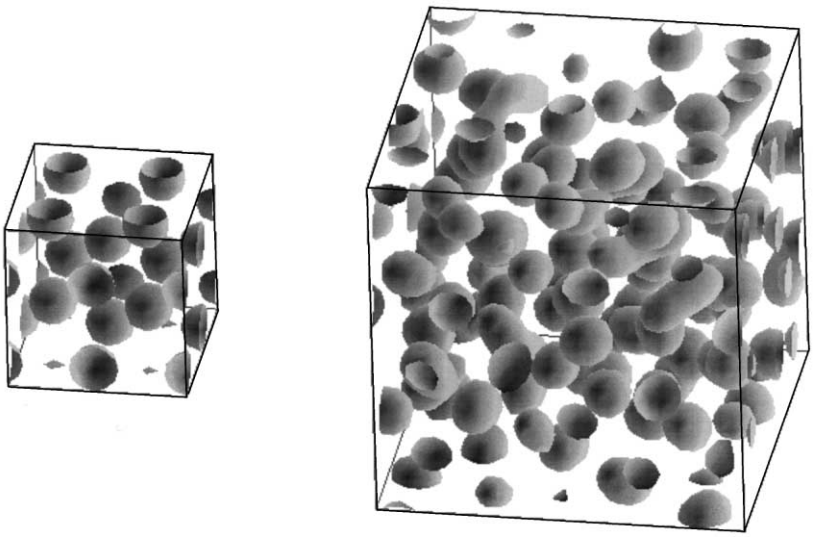

Fig. 31. Morphology of propylene oxide in an aqueous solution (50% polymer surfactant) of $(EO)_{13}(PO)_{30}(EO)_{13}$ [(ethylene oxide)$_{13}$(propylene oxide)$_{30}$(ethylene oxide)$_{13}$] Left: cubic simulation box of edge length 16; right: cubic simulation box of edge length 32. Periodic boundary conditions were used.

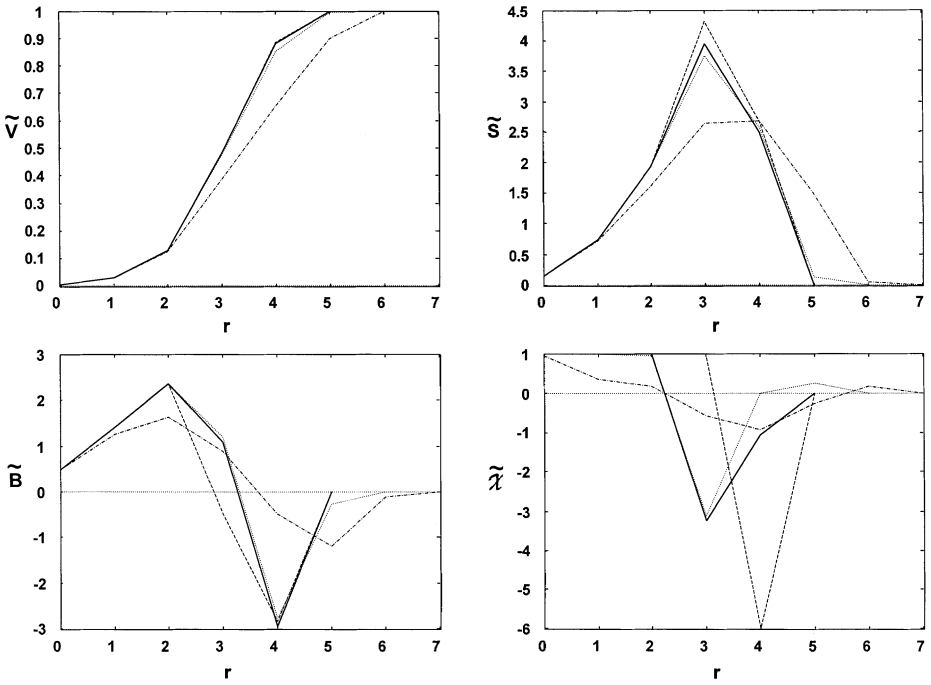

Fig. 32. Minkowski functionals as a function of r. Solid line: simulation data of a 50% aqueous solution of (ethylene oxide)$_{13}$(propylene oxide)$_{30}$(ethylene oxide)$_{13}$ in a cubic box of edge length 16; dashed line: perfect BCC lattice with $M = 2$ and $L_0 = 8$; dotted line: BCC lattice with $M = 2$, $L_0 = 8$ and all lattice points displaced over a randomly chosen distance 0 or 1; dash–dotted line: random set of 16 points in a cubic box of edge length 16. Periodic boundary conditions were used.

1 (dotted line) and for a random set of 16 points in a cubic box of edge length 16 (dash–dotted line). From Fig. 32 we may conclude that the micelles are organized in a BCC lattice structure with $L_0 = 8$ and $M = 2$ and of which the lattice points are somewhat displaced. The Euler characteristic per unit cell for the micellar phase equals two, which is also characteristic for a BCC lattice structure. From the Euler characteristic $\tilde{\chi}$ as a function of r we may see that the radius of the micelles has to be smaller than three lattice units. Otherwise the micelles glue together and $\tilde{\chi}$ differs from one. Fig. 33 demonstrates that it is much harder to draw a similar conclusion from the structure factor $\mathscr{S}(r)$ of the same system. The structure factor of the polymer solution exhibits additional, pronounced peaks, peaks that are absent in the case of a perfect BCC lattice, and also does not resemble the structure factor of a BCC lattice with random distortions.

Fig. 34 shows the Minkowski functionals as a function of r for the propylene oxide in the cubic simulation box of edge length 32 (solid line). The number of micelles, as derived from χ equals 100. For comparison we also depict the Minkowski functionals for a random set of 100 points in a cubic box of edge length 32 (dashed line), for the perfect BCC lattice with $L_0 = 8$ and $M = 4$ (dash–dotted line) and for the same BCC lattice but all lattice points displaced over a randomly chosen distance 0 or 1 (dotted line). From this figure we may conclude that in the bigger simulation box the micelles are no longer organized on a BCC lattice structure, neither that their distribution is random. Again, the latter conclusion is difficult to draw from the structure factor, as can be seen in Fig. 35, where we give $\mathscr{S}(r)$ for the polymer solution (solid line) and for a random set of 100 points in a cubic box of edge length 32 (dotted line). The data of $\mathscr{S}(r)$ suggests that the micelles are randomly distributed in the cube.

In summary, MIA of structures formed in soft materials such as polymer solutions provides information about the mesostructures that is hard to obtain by other methods.

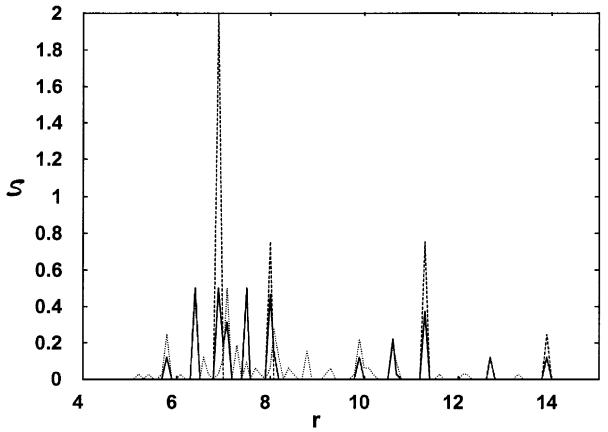

Fig. 33. Structure factor. Solid line: simulation data of a 50% aqueous solution of (ethylene oxide)$_{13}$(propylene oxide)$_{30}$(ethylene oxide)$_{13}$ in a cubic box of edge length 16; dashed line: perfect BCC lattice with $L_0 = 8$ and $M = 2$; dotted line: BCC lattice with $L_0 = 8$ and $M = 2$ and all lattice points displaced over a randomly chosen distance 0 or 1. Periodic boundary conditions were used.

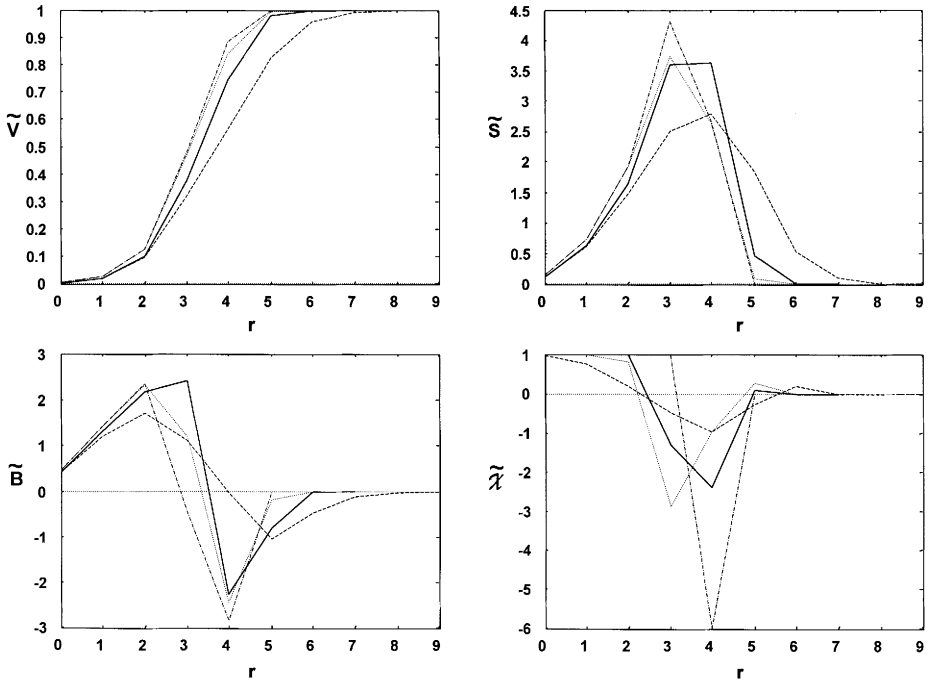

Fig. 34. Minkowski functionals as a function of r. Solid line: simulation data of a 50% aqueous solution of (ethylene oxide)$_{13}$(propylene oxide)$_{30}$(ethylene oxide)$_{13}$ in a cubic box of edge length 32; dashed line: random set of 100 points in a cubic box of edge length 32; dash–dotted line: perfect BCC lattice with $L_0 = 8$ and $M = 4$; dotted line: BCC lattice with $L_0 = 8$ and $M = 4$ and all lattice points displaced over a randomly chosen distance 0 or 1. Periodic boundary conditions were used.

8.2. *Vesicles and worm-like micelles*

Block copolymers are materials that are capable of forming mesoscale structures whose morphology can be tailored by controlled synthesis. Identification and quantification of the morphology of these mesoscale structures may be rather difficult. In this section we consider an example for which conventional crystallographic techniques do not work and for which MIA proves to be very valuable. We perform a MIA on computer-simulation data of the time evolution of a spherical droplet of the diblock copolymer AB_9 in water (W). The data are generated with a three-dimensional dynamic mean-field density functional method [100], a numerical method for the simulation of coarse-grained morphology dynamics in polymer liquids. The simulation box is a cube of edge length 32 with periodic boundaries. The initial spherical droplet has a radius of 10 lattice units.

Fig. 36 shows the morphologies of the B-block after 2000 time steps of diffusion as a function of the interaction exchange parameters $\chi_{AW} = \chi_{AB}$ and χ_{BW}. Depending on the values of χ_{AW} and χ_{BW} the spherical droplet remains a solid sphere, becomes a vesicle or a worm-like micelle. For $\chi_{AW} = 1.0$ and independent of the value of χ_{BW} the polymer droplet dissolves in water what results in a rather homogeneous polymer–water mixture.

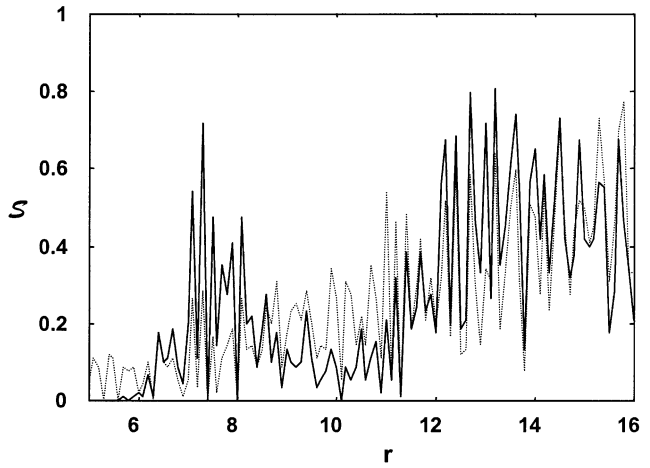

Fig. 35. Structure factor. Solid line: simulation data of a 50% aqueous solution of (ethylene oxide)$_{13}$(propylene oxide)$_{30}$(ethylene oxide)$_{13}$ in a cubic box of edge length 32; dotted line: random set of 100 points in a cubic box of edge length 32. Periodic boundary conditions were used.

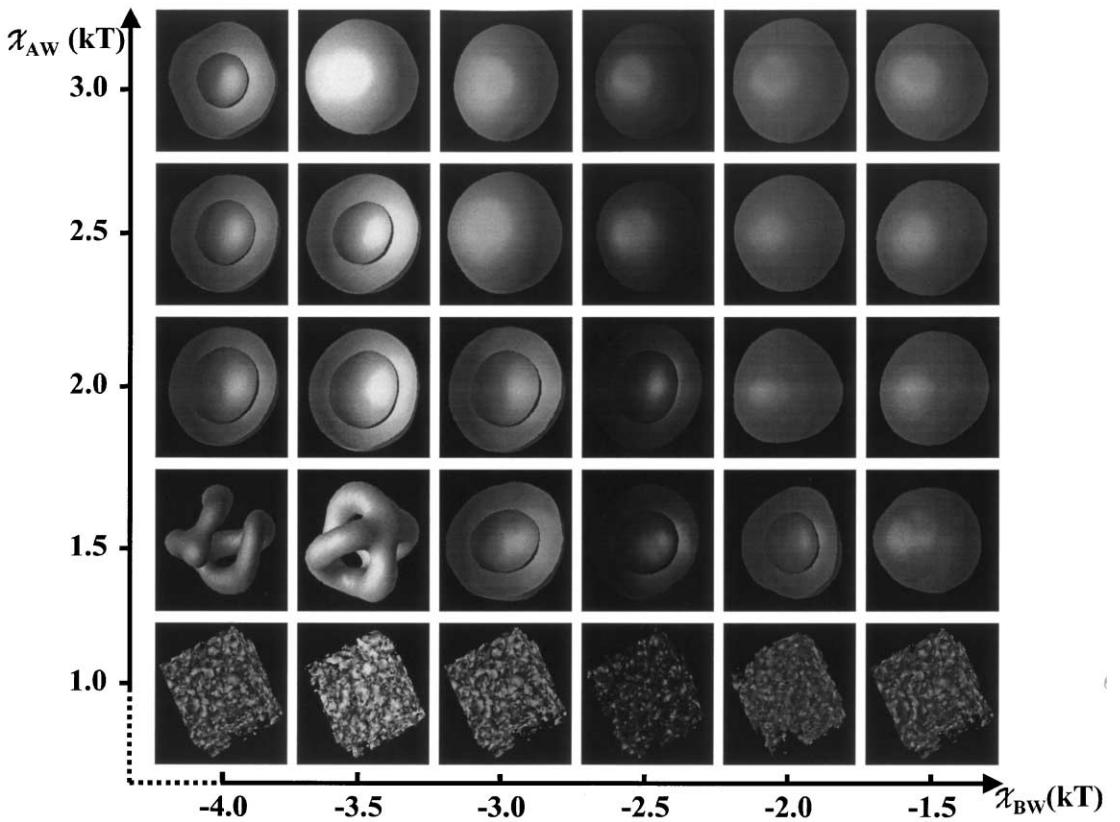

Fig. 36. Morphologies of the B-block at $t = 2000$ as a function of χ_{BW} and χ_{AW}. If the polymer forms a vesicle only half of it is shown.

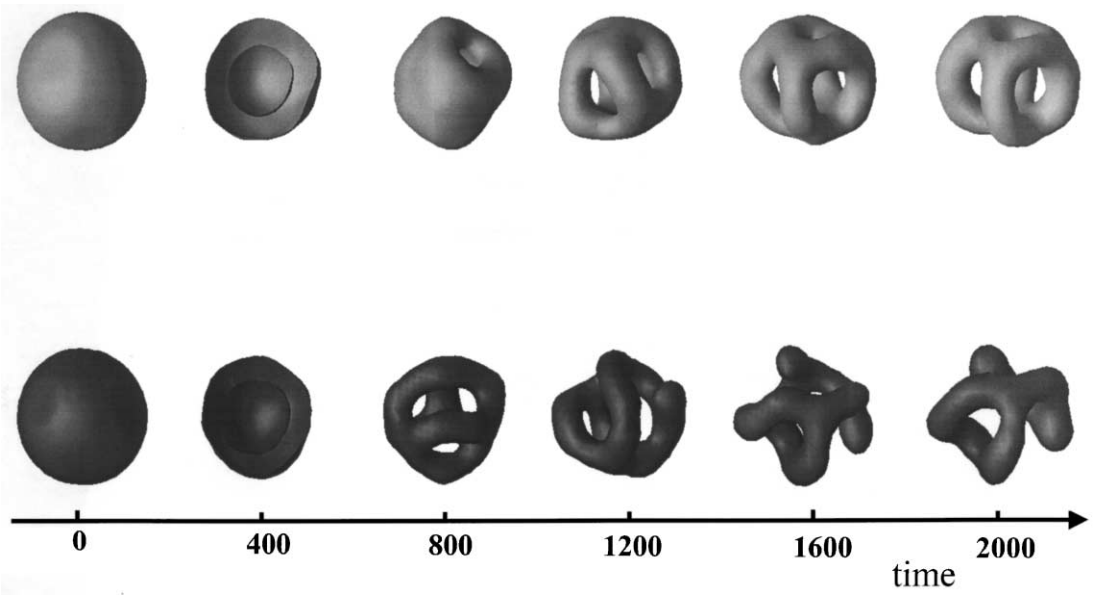

Fig. 37. Morphologies of the B-block as a function of time for $\chi_{AW} = 1.5$. Top: $\chi_{BW} = -3.5$; bottom: $\chi_{BW} = -4.0$. If the polymer forms a vesicle only half of it is shown.

The formation of the worm-like micelles as the dynamic result of diffuse phenomena is illustrated in Fig. 37 in terms of some snapshots of the B-block morphology. The time series at the top (bottom) of the figure is for $\chi_{AW} = 1.5$ and $\chi_{BW} = -3.5$ ($\chi_{BW} = -4.0$). For $\chi_{BW} = -3.5$ ($\chi_{BW} = -4.0$) and $0 < t < 600$ ($0 < t < 400$) the polymer forms a vesicle. A schematic picture of the polymer layers constituting the vesicle is shown in Fig. 38a. For $\chi_{BW} = -3.5$ and $600 < t < 2000$ the polymer organizes in structures that look like hollow spheres with several holes and the number of holes seems to increase with time. In the end the polymer forms a hollow sphere-like structure with many holes. For $\chi_{BW} = -4.0$ and $400 < t < 2000$ the polymer shows a behavior that is similar to that described for $\chi_{BW} = -3.5$ but now the number of holes decreases as a function of time. In the end the polymer forms a worm-like structure with one or more loops. In both cases the B-block is always shielded from contact with water by the A-block.

A quantitative description of the various polymer morphologies may be obtained from MIA. We calculate the Minkowski functionals as a function of time for the B-block for $\chi_{AW} = \chi_{AB} = 1.5$ and several choices of χ_{BW}. The results are shown in Fig. 39. For $t = 0$ and all χ_{BW} the B-block is concentrated in a solid sphere-like structure leading to an Euler characteristic of one. For $\chi_{BW} = -1.5$ (dotted line) the B-block remains organized in a solid sphere-like structure for all times. All Minkowski functionals are approximately constant. For $\chi_{BW} = -3.0$ (dash–dotted line) and $t > 200$ the polymer forms a vesicle, leading to a decrease of the covered volume and the integral mean curvature. The surface area increases and the Euler characteristic equals two. The same happens for $\chi_{BW} = -3.5$ (dashed line) [$\chi_{BW} = -4.0$ (solid line)] and $0 < t < 600$ [$0 < t < 400$]. For $\chi_{BW} = -3.5$ and intermediate t ($600 < t < 1500$) the polymer organizes in structures that look like hollow spheres with several holes. The number of holes increases with

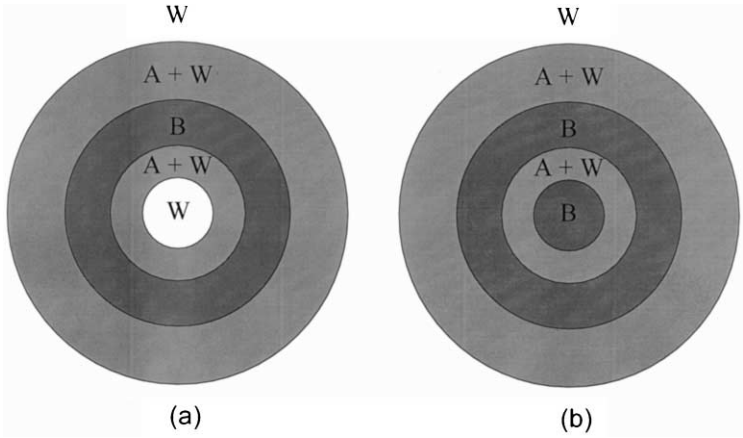

Fig. 38. Schematic picture of the AB_9 polymer vesicle (a) and double-layered micelle (b).

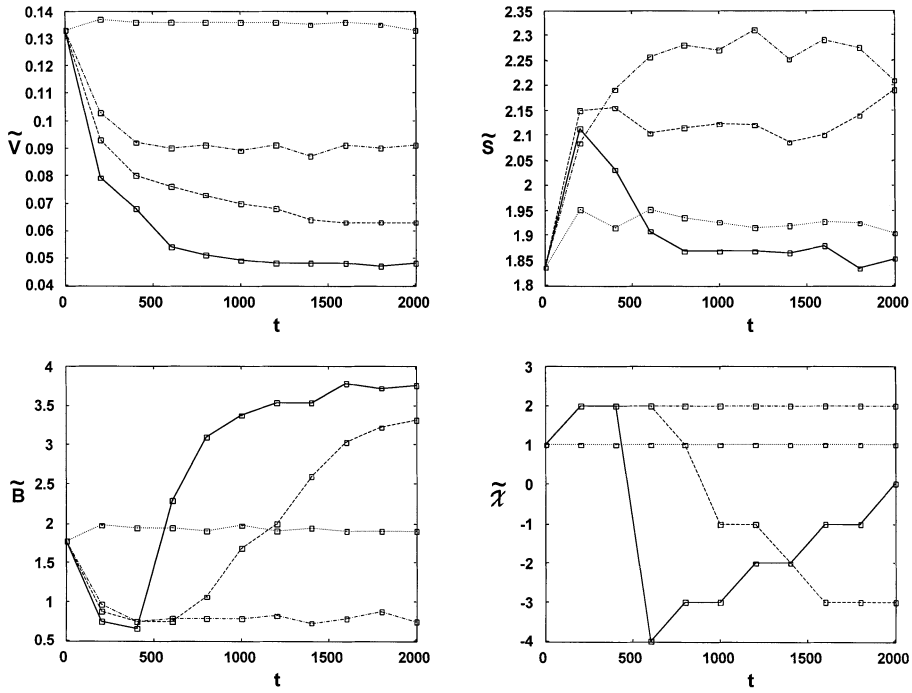

Fig. 39. Minkowski functionals as a function of t for $\chi_{AW} = 1.5$. Solid line: $\chi_{BW} = -4.0$; dashed line: $\chi_{BW} = -3.5$; dash–dotted line: $\chi_{BW} = -3.0$; dotted line: $\chi_{BW} = -1.5$.

time. The Euler characteristic is negative and decreases while the integral mean curvature increases. The volume further decreases and the surface area first decreases (for $t < 800$) and remains approximately constant afterwards. For $\chi_{BW} = -4.0$ and $400 < t < 1500$ the Minkowski functionals show behavior very similar to that described for $\chi_{BW} = -3.5$ except for the fact that the

number of holes (Euler characteristic) decreases (increases) with time. For $\chi_{BW} = -3.5$ and $\chi_{BW} = -4.0$ and large t ($t > 1500$) the polymer structures differ from each other. For $\chi_{BW} = -3.5$ the polymer forms a hollow sphere-like structure with many holes. The integral mean curvature is large and positive and the Euler characteristic is strongly negative. For $\chi_{BW} = -4.0$ the B-block forms a worm-like structure with one or more loops. This gives rise to a large integral mean curvature and an Euler characteristic that is zero or slightly negative. Given the behavior of the Euler characteristic as a function of time (see Fig. 39) we expect that for $t > 2000$ the polymer will organize in a worm-like structure without loops ($\chi = 1$).

To gain more insight into the formation mechanism of the polymer vesicle, we study the polymer morphology for $\chi_{BW} = -4$ and $\chi_{AW} = 1.5$ in more detail for $0 < t < 200$. In Fig. 40 we depict the Minkowski functionals as a function of t for the B-block. For $0 < t < 64$ the B-block is concentrated in a solid sphere-like structure leading to an Euler characteristic of one. All other Minkowski functionals are approximately constant. For $64 < t < 100$ cavities and tunnels are formed in the B-block morphology. The Euler characteristic fluctuates between positive and negative values. The surface area strongly increases. The integral mean curvature first decreases and becomes negative but increases and becomes positive again afterwards. Around $t = 100$ the polymer system seems to stabilize and the Euler characteristic becomes equal to three. The polymer is now organized in a double-layered micelle. A schematic picture of the latter is given in Fig. 38b. When time evolves the excess of B-block material in the core moves to the outer layer of B-block material and finally around $t = 180$ a vesicle is formed (see Fig. 38a for a schematic picture).

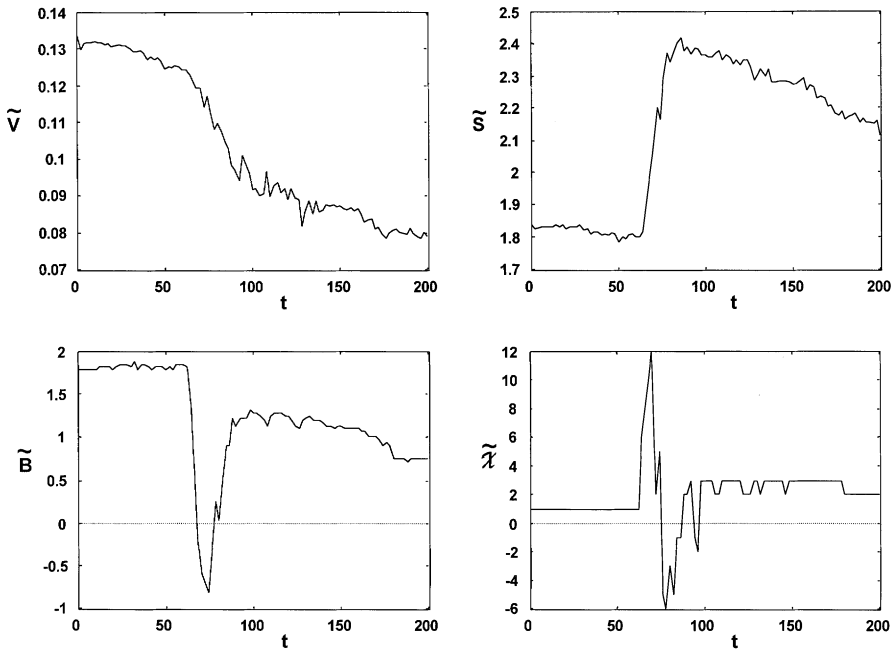

Fig. 40. Minkowski functionals as a function of t ($0 < t < 200$) for $\chi_{AW} = 1.5$, $\chi_{BW} = -4$.

In summary, MIA gives the morphological properties of complex structures formed in polymer solutions and provides detailed information about the structure of the material.

8.3. Complex surfaces

As already mentioned above, depending on the experimental conditions, complex domain structures may be formed in block copolymers. Since the morphology of the final domain structure determines the properties of the polymeric material, the study of the statics and dynamics of these complex structures is a key issue in polymer science. Several computer simulation techniques have been developed to simulate the formation of the domain structures. Once the domain structures are obtained the problem of characterization of the structures arises. Usually, the domain structures are characterized in terms of the average domain size which may be calculated from the first moment of the structure factor or the first zero in the radial distribution function [103,104]. As computer simulations are limited to rather small system sizes a structure factor analysis suffers from severe finite-size effects. Disregarding this problem, the average domain size alone cannot give a complete morphological characterization of the domain structure. For this purpose MIA is very useful [14,21,22,96,99,105].

In this section, we will use MIA to characterize the complex domain structures observed in computer simulation data of an AB binary polymer blend containing A–B-type block copolymer. Adding a small amount of block copolymer to a polymer blend leads to a variety of stable complex domain structures on the mesoscopic scale, such as irregular bicontinuous domains, hexagonally aligned cylinders, and cubic crystalline structures of spherical domains [106]. The domain structure formation in the polymer system is studied by the self-consistent field (SCF) dynamic density functional (DDF) method, a combination of the SCF path integral formalism of the polymer conformations and the mesoscopic transport equations [107–109], and the Ginzburg Landau (GL) method, a more phenomenological approach. For a quantitative comparison between the SCF-DDF and the GL method see [106].

Fig. 41 shows the 2D domain structures, obtained by the GL and SCF-DDF method, of an $A_{10}B_{10}$ polymer blend containing 20% volume fraction of $A_n - B_{20-n}$ block copolymer [106] at time $t = 100$ and 3000. In Fig. 41 a block copolymer with block ratio $f = 0.2$ (left) and 0.5 (right) is added, the block ratio being defined as the ratio of the length of block A to the total chain length of the block copolymer. The domain structures are obtained after a sudden temperature quench from a high-temperature equilibrium state [106]. Initially, (at $t = 0$) the polymer systems were homogeneous mixtures. The A–B segment–segment interaction parameter (so-called Flory–Huggins interaction parameter χ_{AB}) is set to 0.5. The simulation box is a square of edge length 128 subject to periodic boundaries.

The pictures in Fig. 41 suggest that for $f = 0.5$ the resulting domain structure (at $t = 3000$) is bicontinuous while for $f = 0.2$ it is globular. In order to study the dynamics of the domain structure formation in more detail we compute the Minkowski functionals as a function of time for all cases. The results are shown in Fig. 42 ($f = 0.2$, GL method: solid line; $f = 0.2$, SCF-DDF method: dashed line; $f = 0.5$, GL method: dotted line and $f = 0.5$, SCF-DDF method: dash–dotted line). Both methods give roughly the same results. The area A/L^2 is more or less constant as a function of time. The perimeter U/L decreases as a function of time. For $f = 0.2$, the Euler characteristic is positive and slightly decreases as a function of time. This means that for $f = 0.2$ the domain structure

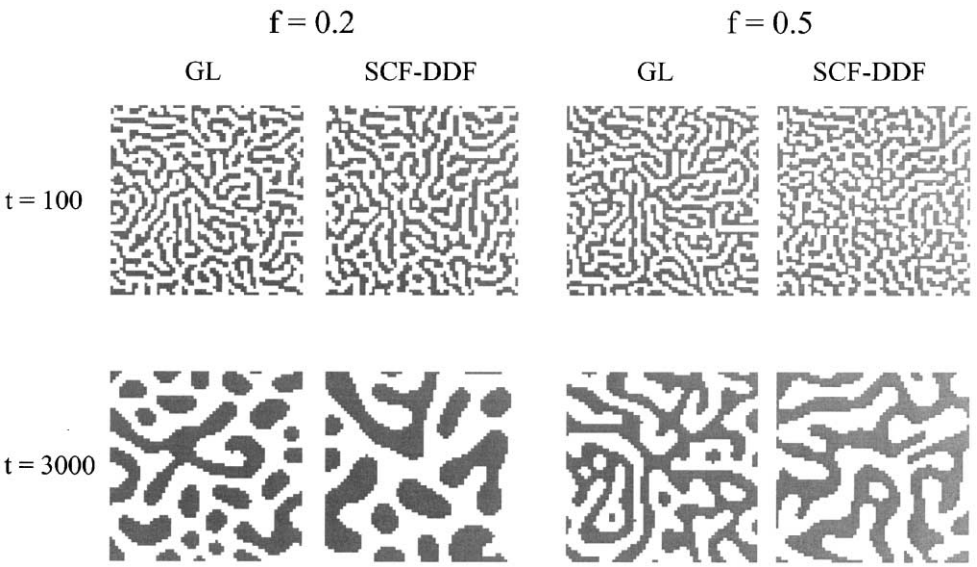

Fig. 41. Two-dimensional domain structures of an $A_{10}B_{10}$ polymer blend containing 20% volume fraction of $A_n - B_{20-n}$ block copolymer. Left: $A_4 - B_{16}, f = 0.2$; right: $A_{10} - B_{10}, f = 0.5$.

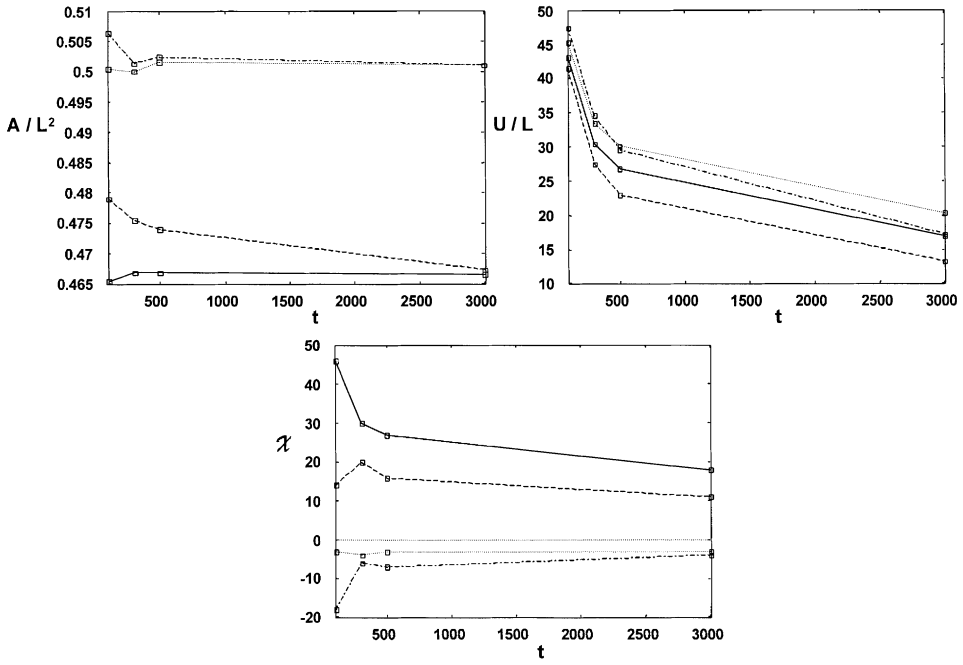

Fig. 42. Minkowski functionals as a function of t for simulation data of an $A_{10}B_{10}$ polymer blend containing 20% volume fraction of $A_n - B_{20-n}$ block copolymer in a square of edge length 128. Solid line: $f = 0.2$, GL method; dashed line: $f = 0.2$, SCF-DFF method; dotted line: $f = 0.5$, GL method; dash–dotted line: $f = 0.5$, SCF-DFF method.

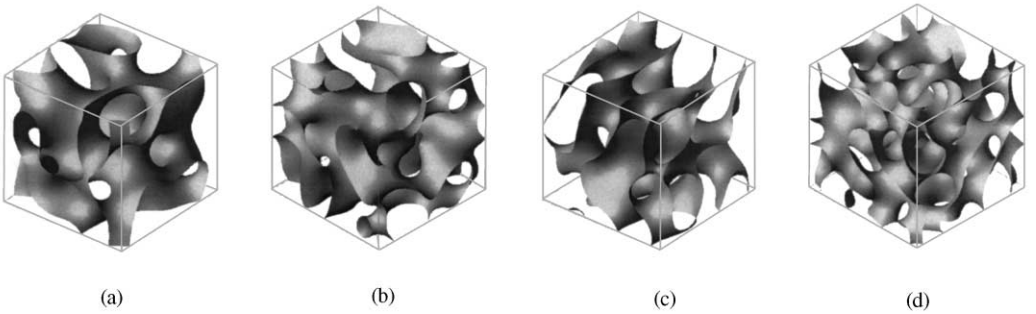

Fig. 43. Three-dimensional domain structures of an $A_{10}B_{10}$ polymer blend containing 20% volume fraction of $A_n - B_{20-n}$ block copolymer. (a) $A_4 - B_{16}$, $f = 0.2$, SCF-DDF method; (b) $A_4 - B_{16}$, $f = 0.2$, GL method; (c) $A_{10} - B_{10}$, $f = 0.5$, SCF-DDF method; (d) $A_{10} - B_{10}$, $f = 0.5$, GL method.

consists of separate objects and that the number of separate objects is slightly decreasing as a function of time. For $f = 0.5$, the Euler characteristic is always negative pointing to a bicontinuous domain structure. The resulting domain structure depends on the architecture of the block copolymer. For comparison, the results for the average domain size as a function of time can be found in [106].

In Fig. 43 we show the 3D domain structures, obtained by the SCF-DDF method ((a) and (c)) and the GL method ((b) and (d)), of an $A_{10}B_{10}$ polymer blend containing 20% volume fraction of $A_n - B_{20-n}$ block copolymer [106] at time $t = 1000$. Also for this example $\chi_{AB} = 0.5$. The simulation box is a cube of edge length 32 with periodic boundaries. In Figs. 43(a), (b) ((c), (d)) a block copolymer with block ratio $f = 0.2$ ($f = 0.5$) is added. In both cases, interconnected bicontinuous structures are observed. Initially (at $t = 0$) the polymer systems were homogeneous mixtures. In order to study the evolution of morphology of the domain structures in more detail we compute their Minkowski functionals as a function of time. The results are depicted in Fig. 44 ($f = 0.2$, GL method: solid line; $f = 0.2$, SCF-DDF method: dashed line; $f = 0.5$, GL method: dotted line and $f = 0.5$, SCF-DDF method: dash–dotted line). As in the case for the 2D system also for the 3D system both methods give roughly the same results. As a function of time the volume V/L^3 is more or less constant, the mean breadth B/L is also more or less constant but rather small and positive and the area S/L^2 decreases. The Euler characteristic is negative and increases as a function of time. Hence the domain structure is net-like for $f = 0.2$ as well as for $f = 0.5$. The fact that the 3D system behaves differently from the 2D system may have two reasons. First, finite-size effects play a more important role in 3D than in 2D systems and second, the percolation characteristics in 2D and 3D continuum systems are different. For the 2D continuum system, the percolation threshold $p_c = 0.5$, above which the Euler characteristic becomes negative and the system forms a percolating mesh structure. For the 3D system there exist two percolation thresholds $p_c \approx 0.16$ and $p_c' \approx 0.84$ [95]. For $p_c < p < p_c'$ the system forms a percolating mesh structure ($\chi < 0$). This suggests that in 2D it is rather easy to observe the morphological transition from a globular system to a bicontinuous one. Introduction of a slight asymmetry between the A and B phase is sufficient to observe the transition since a bicontinuous phase can only be obtained in the vicinity of the symmetric composition (percolation threshold $p_c = 0.5$). However, in

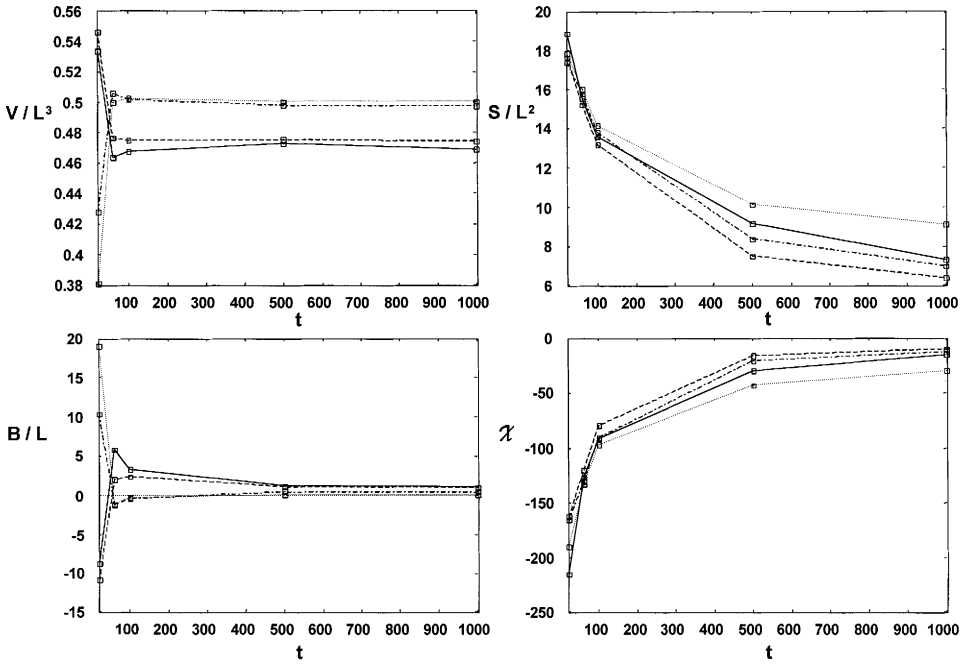

Fig. 44. Minkowski functionals as a function of t for simulation data of an $A_{10}B_{10}$ polymer blend containing 20% volume fraction of $A_n - B_{20-n}$ block copolymer in a cubic box of edge length 32. Solid line: $f = 0.2$, GL method; dashed line: $f = 0.2$, SCF-DFF method; dotted line: $f = 0.5$, GL method; dash–dotted line: $f = 0.5$, SCF-DFF method.

the 3D system the bicontinuous phase can be seen in a much larger region ($0.16 < p_c < 0.84$). Therefore, a slight asymmetry between the two phases is not enough to induce the morphological transition for a system with a nearly symmetric composition.

The Minkowski functionals for cases (b) and (d) are [105]

$$\text{(b):}\quad N = 8;\quad \bar{V} = 0.47;\quad \bar{S} = 3.65;\quad \bar{B} = 0.27;\quad \bar{\chi} = -1.88\,,$$

$$\text{(d):}\quad N = 8;\quad \bar{V} = 0.50;\quad \bar{S} = 4.55;\quad \bar{B} = 0.023;\quad \bar{\chi} = -3.75 \tag{67}$$

and are close to the values of oriented P and G surfaces (at threshold $q = 0.5$, one unit cell and $L_0 = 32$)

$$\text{P:}\quad \bar{V} = 0.50;\quad \bar{S} = 3.71;\quad \bar{B} = 0;\quad \bar{\chi} = -2\,,$$

$$\text{G:}\quad \bar{V} = 0.50;\quad \bar{S} = 4.90;\quad \bar{B} = 0;\quad \bar{\chi} = -4\,. \tag{68}$$

For cases (a) and (c) we find

$$\text{(a):}\quad N = 1;\quad \bar{V} = 0.47;\quad \bar{S} = 6.37;\quad \bar{B} = 1.00;\quad \bar{\chi} = -10.00\,,$$

$$\text{(c):}\quad N = 8;\quad \bar{V} = 0.50;\quad \bar{S} = 3.50;\quad \bar{B} = 0.13;\quad \bar{\chi} = -1.63 \tag{69}$$

which resemble the values of oriented D and P surfaces (at threshold $q = 0.5$, one unit cell and $L_0 = 32$)

$$\text{D:}\quad \bar{V} = 0.50;\quad \bar{S} = 6.00;\quad \bar{B} = 0;\quad \bar{\chi} = -8\,,$$

$$\text{P:}\quad \bar{V} = 0.50;\quad \bar{S} = 3.71;\quad \bar{B} = 0;\quad \bar{\chi} = -2\,. \tag{70}$$

These examples show that MIA can be used to characterize complex, computer generated surfaces with modest efforts.

9. Summary

Integral-geometry morphological image analysis characterizes patterns in terms of numerical quantities, called Minkowski functionals. These morphological descriptors have an intuitively clear geometrical and topological interpretation. Integral-geometry morphological image analysis yields information on structure in patterns. In most cases this information is complementary to the one obtained from two-point correlation functions.

As the examples presented in this review and many other applications mentioned in the introduction show, MIA is a very versatile and powerful method to study structure in (complex) patterns. For some problems, e.g. the characterization of complex surfaces, the same morphological descriptors can also be computed within the framework of differential geometry. In contrast to the differential geometry approach, the application of integral geometry does not require the surface to be regular, nor is there any need to introduce labyrinth graphs or surface tilings to compute derivatives.

A remarkable feature of MIA is the big contrast between the level of sophistication of the underlying mathematics and the ease with which MIA can be implemented and used. MIA is applied directly to the digitized representation of the patterns, it can be implemented with a few lines of computer code, is computationally inexpensive and is easy to use in practice. Therefore, we believe it should be part of one's toolbox for analyzing geometrical objects and patterns.

Acknowledgements

We are grateful to Prof. H. Wagner for very helpful advice and to Prof. J.Th.M. De Hosson for providing us with the SEM images and for helpful discussions. We would like to thank Dr. G.J.A. Sevink, Prof. J.G.E.M. Fraaije and Dr. T. Kawakatsu (work partially supported by the national project, which has been entrusted to the Japan Chemical Innovation Institute by the New Energy and Industrial Technology Development Organization (NEDO) under MITI's Program for the Scientific Technology Development for Industries that Creates New Industries) for providing us the simulation data of the Pluronic-water mixtures, of vesicles and worm-like micelles, and of the complex surfaces in $A_n - B_{20-n}$ block copolymers respectively. Part of this research has been financially supported by the Council for Chemical Sciences of the Netherlands (CW/NWO) and Unilever Research Laboratories.

Appendix A. Programming example

```
!
! Minkowski_functionals_2D computes the Minkowski functionals
! (area,perimeter,euler) for a 2D image, represented by the
! 1D array LATTICE(.). A pixel at (jx,jy) is active if LATTICE(jx+jy*Lx) = 1,
! otherwise LATTICE(jx+jy*Lx) = 0. Here 0 < jx < Lx and 0 < jy < Ly.
! The array TMP(.) is used as work space.
!
      subroutine minkowski_functionals_2D(Lx,Ly,lattice,tmp,
     &                                    area,perimeter,euler) ! 2D
      implicit integer (a-z)
      integer lattice(0:Lx*Ly - 1),tmp(0:(Lx+2)*(Ly+2) - 1)

      sur = 0
      cur = 0
      eul = 0

      tmp(0:(Lx+2)*(Ly+2) - 1) = 0 ! work space

      do jy = 0,Ly - 1
      do jx = 0,Lx - 1
        i = jx+Lx*jy
        if( lattice(i) > 0 ) then ! active pixel
          call minko_2D_free(Lx+2,Ly+2,jx+1,jy+1,tmp,s,c,e)
          tmp(jx+1+(Lx+2)*(jy+1)) = 1 ! add pixel to image
          sur = sur+s
          cur = cur+c
          eul = eul+e
        endif
      enddo
      enddo

      area = sur
      perimeter = cur
      euler = eul

      end

!
! Minkowski_functionals_3D computes the Minkowski functionals
! (volume,surface,integral mean curvature,euler) for a 3D image,
! represented by the 1D array LATTICE(.). A pixel at (jx,jy,jz) is
! active if LATTICE(jx+Lx*(jy+Ly*jz)) = 1, otherwise
```

```
!  LATTICE(jx+Lx*(jy+Ly*jz)) = 0.
!  Here 0 < jx < Lx, 0 < jy < Ly, and 0 < jz < Lz. The array TMP(.)
!  is used as work space.
!
      subroutine minkowski_functionals_3D(Lx,Ly,Lz,tmp,
     &                                    lattice,volume,surface,curvature,euler)
      implicit integer (a-z)
      integer lattice(0:Lx*Ly*Lz - 1),tmp(0:(Lx+2)*(Ly+2)*(Lz+2) - 1)

      vol = 0
      sur = 0
      cur = 0
      eul = 0

      tmp(0:(Lx+2)*(Ly+2)*(Lz+2) - 1) = 0 ! work space

      do jz = 0,Lz - 1
      do jy = 0,Ly - 1
      do jx = 0,Lx - 1
      i = jx+Lx*(jy+Ly*jz)
        if( lattice(i) > 0 ) then ! active pixel
          call minko_3D_free(Lx+2,Ly+2,Lz+2,jx+1,jy+1,jz+1,tmp,v,s,c,e)
          tmp(jx+1+(Lx+2)*(jy+1+(Ly+2)*(jz+1))) = 1 ! add pixel to image
          vol = vol+v
          sur = sur+s
          cur = cur+c
          eul = eul+e
        endif
      enddo
      enddo
      enddo

      volume = vol
      surface = sur
      curvature = cur
      euler = eul

      end

      subroutine minko_2D_free(Lx,Ly,jx,jy,
     &                         lattice,surface,perimeter,euler2D)
      implicit integer (a-z)
      integer lattice(0:LX*LY - 1)
      parameter(
```

```
&   surface_face = 1                ,    !(a*a, open face)
&   perimeter_face = -4             ,    !(-4*a, open face)
&   perimeter_edge = 2              ,    !(2*a, open line)
&   euler2D_face = 1                ,    !(open face)
&   euler2D_edge = -1               ,    !(open line)
&   euler2D_vertex = 1)                  !(vertices)

  nedges = 0
  nvert = 0

  do i0 = -1,1,2
    jxi = jx+i0
    jyi = jy+i0
    kc1 = 1 - lattice(jxi+Lx*jy)
    nedges = nedges+kc1 + 1 - lattice(jx+Lx*jyi)
    do j0 = -1,1,2
       k4 = Lx*(jy+j0)
       nvert = nvert+kc1*(1-lattice(jxi+k4))*(1-lattice(jx+k4))
    enddo ! j0
  enddo ! i0

  surface = surface_face
  perimeter = perimeter_face+perimeter_edge*nedges
  euler2D = euler2D_face+euler2D_edge*nedges+euler2D_vertex*nvert

  end

  subroutine minko_3D_free(Lx,Ly,Lz,jx,jy,jz, lattice,
&                 volume,surface,curvature,euler3D)

  implicit integer (a-z)
  integer lattice(0:LX*LY*Lz - 1)
  parameter(

&   volume_body = 1 ,     !(a*a*a, where a is lattice displacement)

&   surface_body = -6 , !(-6*a*a, open body)
&   surface_face = 2 ,  !(2*a*a, open face)

&   curv_body = 3 ,  !(3*a, open body)
&   curv_face = -2 ,  !(-2*a, open face)
&   curv_edge = 1 ,  !(a, open line)
&   euler3D_body = -1 ,  !(open body)
&   euler3D_face = 1 ,  !(open face)
```

```
&    euler3D_edge = -1 ,   !(open line)
&    euler3D_vertex = 1)   !(vertices)

   nfaces = 0
   nedges = 0
   nvert = 0


   do i0 = -1,1,2
     jxi = jx+i0
     jyi = jy+i0
     jzi = jz+i0
     kc1 = 1 - lattice(jxi+Lx*(jy+Ly*jz))
     kc2 = 1 - lattice(jx+Lx*(jyi+Ly*jz))
     kc3 = 1 - lattice(jx+Lx*(jy+Ly*jzi))
     nfaces = nfaces+kc1+kc2+kc3
     do j0 = -1,1,2
       jyj = jy+j0
       jzj = jz+j0
       k4 = Lx*(jyj+Ly*jz)
       k7 = Lx*(jy+Ly*jzj)
       kc7 = 1 - lattice(jx+k7)
       kc1kc4kc5 = kc1*(1 - lattice(jxi+k4))*(1 - lattice(jx+k4))
       nedges = nedges+kc1kc4kc5
&                      +kc2*(1 - lattice(jx+Lx*(jyi+Ly*jzj)))*kc7
&                      +kc1*(1 - lattice(jxi+k7))*kc7
   if(kc1kc4kc5.ne.0) then
     do k0 = -1,1,2
       jzk = jz+k0
       k9 = Lx*(jy+Ly*jzk)
       k10 = Lx*(jyj+Ly*jzk)
       nvert = nvert+(1 - lattice(jxi+k9))*(1 - lattice(jxi+k10))
&                   *(1 - lattice(jx+k10))*(1 - lattice(jx+k9))
     enddo ! k0
    endif ! kc1kc4kc5
   enddo ! j0
  enddo ! i0


   volume = volume_body
   surface = surface_body+surface_face*nfaces
   curvature = curv_body+curv_face*nfaces+curv_edge*nedges
   euler3D = euler3D_body+euler3D_face*nfaces
&            +euler3D_edge*nedges+euler3D_vertex*nvert
   end
```

Appendix B. Algorithm

We describe a procedure to determine how the number of open bodies of each type changes when one adds (removes) one active pixel (see Section 2.2) to (from) a given pattern.

Using this procedure it is easy to compute the Minkowski functionals for a given pattern, namely by adding the active pixels one by one to an initially empty picture (see Appendix A).

In 2D, the number $n_2(\mathscr{P})$ of open squares building up the objects in the $L_x \times L_y$ picture $\mathscr{P}(\boldsymbol{x}, q) = \mathscr{P}(i,j,q)$; $(i = 1,\ldots,L_x, j = 1,\ldots,L_y)$ increases (decreases) with one if one adds (removes) one active pixel at the position $\boldsymbol{x} = (i,j)$ to (from) the image. Therefore, if we add an active pixel,

$$\Delta n_2(\mathscr{P}) = 1 \ , \tag{B.1}$$

where we introduce the symbol Δ to indicate that we compute the difference. Similarly, the change in the number of open edges, $\Delta n_1(\mathscr{P})$ is given by

$$\Delta n_1(\mathscr{P}) = \sum_{\alpha = \pm 1} [\mathscr{Q}(i+\alpha,j,q) + \mathscr{Q}(i,j+\alpha,q)] \ , \tag{B.2}$$

where $\mathscr{Q}(\boldsymbol{x}, q) = 1 - \mathscr{P}(\boldsymbol{x}, q)$. For the change in the number of vertices, $n_0(\mathscr{P})$, we find

$$\Delta n_0(\mathscr{P}) = \sum_{\alpha,\beta = \pm 1} \mathscr{Q}(i+\alpha,j,q)\mathscr{Q}(i+\alpha,j+\beta,q)\mathscr{Q}(i,j+\beta,q) \ . \tag{B.3}$$

The change in the number of steps, $n_S(\mathscr{P})$, may be computed from

$$\Delta n_S(\mathscr{P}) = \sum_{\alpha,\beta = \pm 1} \mathscr{P}(i+\alpha,j+\beta,q)(\mathscr{Q}(i+\alpha,j,q) + \mathscr{Q}(i,j+\beta,q)) \ . \tag{B.4}$$

In 3D, the number $n_3(\mathscr{P})$ of open cubes building up the objects in the $L_x \times L_y \times L_z$ image $\mathscr{P}(\boldsymbol{x}, q) = \mathscr{P}(i,j,k,q)$; $(i = 1,\ldots,L_x, j = 1,\ldots,L_y, k = 1,\ldots,L_z)$ increases (decreases) with one if one adds (removes) one active pixel to (from) the image at the position $\mathbf{x} = (i,j,k)$, i.e. $\Delta n_3(\mathscr{P}) = 1$. The change in $n_2(\mathscr{P})$, the number of open faces, may be computed from

$$\Delta n_2(\mathscr{P}) = \sum_{\alpha = \pm 1} [\mathscr{Q}(i+\alpha,j,k,q) + \mathscr{Q}(i,j+\alpha,k,q) + \mathscr{Q}(i,j,k+\alpha,q)] \ . \tag{B.5}$$

The change in $n_1(\mathscr{P})$, the number of open edges, reads

$$\begin{aligned}\Delta n_1(\mathscr{P}) = \sum_{\alpha,\beta = \pm 1} [&\mathscr{Q}(i+\alpha,j,k,q)\mathscr{Q}(i+\alpha,j+\beta,k,q)\mathscr{Q}(i,j+\beta,k,q) \\ &+ \mathscr{Q}(i,j+\alpha,k,q)\mathscr{Q}(i,j+\alpha,k+\beta,q)\mathscr{Q}(i,j,k+\beta,q) \\ &+ \mathscr{Q}(i+\alpha,j,k,q)\mathscr{Q}(i+\alpha,j,k+\beta,q)\mathscr{Q}(i,j,k+\beta,q)] \ .\end{aligned} \tag{B.6}$$

For the change in $n_0(\mathscr{P})$, the number of vertices, we find

$$\Delta n_0(\mathscr{P}) = \sum_{\alpha,\beta,\gamma=\pm 1} \mathscr{Q}(i+\alpha,j,k,q)\mathscr{Q}(i+\alpha,j+\beta,k,q)\mathscr{Q}(i,j+\beta,k,q) \times \mathscr{Q}(i+\alpha,j,k+\gamma,q)\mathscr{Q}(i+\alpha,j+\beta,k+\gamma,q) \times \mathscr{Q}(i,j+\beta,k+\gamma,q)\mathscr{Q}(i,j,k+\gamma,q) \; . \tag{B.7}$$

The change in $n_S(\mathscr{P})$, the number of steps, is given by

$$\Delta n_S(\mathscr{P}) = \sum_{\alpha,\beta=\pm 1} [\mathscr{P}(i+\alpha,j+\beta,k,q)(\mathscr{Q}(i+\alpha,j,k,q) + \mathscr{Q}(i,j+\beta,k,q)) + \mathscr{P}(i+\alpha,j,k+\beta,q)(\mathscr{Q}(i+\alpha,j,k,q) + \mathscr{Q}(i,j,k+\beta,q)) + \mathscr{P}(i,j+\alpha,k+\beta,q)(\mathscr{Q}(i,j+\alpha,k,q) + \mathscr{Q}(i,j,k+\beta,q))] \; . \tag{B.8}$$

Appendix C. Minkowski functionals for elementary bodies

We derive the values of the Minkowski functionals for the open bodies building up a black-and-white image. A 2D image consists of square pixels. Each pixel is a closed square $Q \in \mathbb{R}^2$ of edge length a and is the union of its interior $\breve{Q}$, its four open edges $\breve{L}$, and its four vertices P (points are open as well as closed convex bodies). The parallel volume $v^{(2)}(Q_r)$ is given by

$$v^{(2)}(Q_r) = a^2 + 4ar + \pi r^2 \; , \tag{C.1}$$

which by making use of (21b) and (34) implies

$$W_0^{(2)}(Q) = W_0^{(2)}(\breve{Q}) = a^2, \quad W_1^{(2)}(Q) = -W_1^{(2)}(\breve{Q}) = 2a \; ,$$
$$W_2^{(2)}(Q) = W_2^{(2)}(\breve{Q}) = \pi \; , \tag{C.2}$$

and

$$A(Q) = A(\breve{Q}) = a^2, \quad U(Q) = -U(\breve{Q}) = 4a, \quad \chi(Q) = \chi(\breve{Q}) = 1 \; . \tag{C.3}$$

Next, we consider the closed edge $L \in \mathbb{R}^2$ of length a. The parallel volume $v^{(2)}(L_r)$ is obtained from

$$v^{(2)}(L_r) = 2ar + \pi r^2 \; , \tag{C.4}$$

which leads to

$$W_0^{(2)}(L) = -W_0^{(2)}(\breve{L}) = 0, \quad W_1^{(2)}(L) = W_1^{(2)}(\breve{L}) = a \; ,$$
$$W_2^{(2)}(L) = -W_2^{(2)}(\breve{L}) = \pi \tag{C.5}$$

and

$$A(L) = -A(\breve{L}) = 0, \quad U(L) = U(\breve{L}) = 2a, \quad \chi(L) = -\chi(\breve{L}) = 1 \; . \tag{C.6}$$

Finally, we consider the vertices $P \in \mathbb{R}^2$. Their parallel volume reads

$$v^{(2)}(P_r) = \pi r^2 \; . \tag{C.7}$$

Hence,

$$W_0^{(2)}(P) = W_0^{(2)}(\breve{P}) = 0, \quad W_1^{(2)}(P) = -W_1^{(2)}(\breve{P}) = 0 ,$$

$$W_2^{(2)}(P) = W_2^{(2)}(\breve{P}) = \pi \tag{C.8}$$

and

$$A(P) = A(\breve{P}) = 0, \quad U(P) = -U(\breve{P}) = 0, \quad \chi(P) = \chi(\breve{P}) = 1 . \tag{C.9}$$

A 3D image contains closed cubes C, each being the union of its interior $\breve{C}$, its six open faces $\breve{Q}$, its twelve open edges $\breve{L}$ and its eight vertices P.

For the closed cube $C \in \mathbb{R}^3$ of edge length a the parallel volume reads

$$v^{(3)}(C_r) = a^3 + 6a^2 r + 3a\pi r^2 + \frac{4\pi}{3} r^3 , \tag{C.10}$$

from which it follows that

$$W_0^{(3)}(C) = W_0^{(3)}(\breve{C}) = a^3, \quad W_1^{(3)}(C) = -W_1^{(3)}(\breve{C}) = 2a^2 ,$$

$$W_2^{(3)}(C) = W_2^{(3)}(\breve{C}) = \pi a, \quad W_3^{(3)}(C) = -W_3^{(3)}(\breve{C}) = \frac{4\pi}{3} , \tag{C.11}$$

and

$$V(C) = V(\breve{C}) = a^3, \quad S(C) = -S(\breve{C}) = 6a^2 ,$$

$$B(C) = B(\breve{C}) = \tfrac{3}{2}a, \quad \chi(C) = -\chi(\breve{C}) = 1 . \tag{C.12}$$

The parallel volume for the closed square $Q \in \mathbb{R}^3$ of edge length a is given by

$$v^{(3)}(Q_r) = 2a^2 r + 2\pi a r^2 + \frac{4\pi}{3} r^3 , \tag{C.13}$$

which implies

$$W_0^{(3)}(Q) = -W_0^{(3)}(\breve{Q}) = 0, \quad W_1^{(3)}(Q) = W_1^{(3)}(\breve{Q}) = \tfrac{2}{3}a^2 ,$$

$$W_2^{(3)}(Q) = -W_2^{(3)}(\breve{Q}) = \frac{2\pi a}{3}, \quad W_3^{(3)}(Q) = W_3^{(3)}(\breve{Q}) = \frac{4\pi}{3} \tag{C.14}$$

and

$$V(Q) = -V(\breve{Q}) = 0, \quad S(Q) = S(\breve{Q}) = 2a^2 ,$$
$$B(Q) = -B(\breve{Q}) = a, \quad \chi(Q) = \chi(\breve{Q}) = 1 . \tag{C.15}$$

For the closed line $L \in \mathbb{R}^3$ of length a the parallel volume can be obtained from

$$v^{(3)}(L_r) = \pi a r^2 + \frac{4\pi}{3} r^3 . \tag{C.16}$$

This yields for the Minkowski functionals

$$W_0^{(3)}(L) = W_0^{(3)}(\breve{L}) = 0, \quad W_1^{(3)}(L) = -W_1^{(3)}(\breve{L}) = 0 ,$$
$$W_2^{(3)}(L) = W_2^{(3)}(\breve{L}) = \frac{\pi a}{3}, \quad W_3^{(3)}(L) = -W_3^{(3)}(\breve{L}) = \frac{4\pi}{3} \tag{C.17}$$

and hence

$$V(L) = V(\breve{L}) = 0, \quad S(L) = -S(\breve{L}) = 0 ,$$
$$B(L) = B(\breve{L}) = \frac{a}{2}, \quad \chi(L) = -\chi(\breve{L}) = 1 . \tag{C.18}$$

Finally, for the vertices $P \in \mathbb{R}^3$ we have for the parallel volume

$$v^{(3)}(P_r) = \frac{4\pi}{3} r^3 , \tag{C.19}$$

which leads to

$$W_0^{(3)}(P) = -W_0^{(3)}(\breve{P}) = 0, \quad W_1^{(3)}(P) = W_1^{(3)}(\breve{P}) = 0 ,$$
$$W_2^{(3)}(P) = -W_2^{(3)}(\breve{P}) = 0, \quad W_3^{(3)}(P) = W_3^{(3)}(\breve{P}) = \frac{4\pi}{3} , \tag{C.20}$$

and

$$V(P) = -V(\breve{P}) = 0, \quad S(P) = S(\breve{P}) = 0 ,$$
$$B(P) = -B(\breve{P}) = 0, \quad \chi(P) = \chi(\breve{P}) = 1 . \tag{C.21}$$

Appendix D. Proof of (47)

The aim is to compute the mean value of $M_v^{(d)}(\mathscr{A}_N)$, i.e. the configurational average with respect to the product density element [11]

$$\mathrm{d}\mu(g_1, \ldots, g_N) = \frac{1}{|\Omega|^N} \prod_{i=1}^{N} \mathrm{d}g_i , \tag{D.1}$$

where $\int \mathrm{d}g_i = |\Omega|$ denotes the volume of Ω.

We first consider the configurational average of a single grain. We rewrite (46) as

$$\mathscr{A}_N = \mathscr{A}_{N-1} \cup g_N A_N \tag{D.2}$$

and make use of the properties of additivity and motion invariance of the Minkowski functionals, and of the kinematic formula (28). The configurational average for the single grain A_N reads

$$\begin{aligned}\int M_\nu^{(d)}(\mathscr{A}_N)\frac{\mathrm{d}g_N}{|\Omega|} &= M_\nu^{(d)}(\mathscr{A}_{N-1}) + M_\nu^{(d)}(A_N) - \int M_\nu^{(d)}(\mathscr{A}_{N-1}\cap g_N A_N)\frac{\mathrm{d}g_N}{|\Omega|} \\ &= M_\nu^{(d)}(\mathscr{A}_{N-1}) + M_\nu^{(d)}(A_N) - \frac{1}{|\Omega|}\sum_{\nu=0}^{\mu}\binom{\mu}{\nu} M_{\mu-\nu}^{(d)}(A_N) M_\mu^{(d)}(\mathscr{A}_{N-1})\,. \end{aligned} \tag{D.3}$$

At this point it is expedient to switch to a matrix notation. For $d = 3$ and with the notation $M_\nu \equiv M_\nu^{(d)}$, (D.3) reads

$$\int \boldsymbol{M}_N \frac{\mathrm{d}g_N}{|\Omega|} = \boldsymbol{Q}_N \boldsymbol{M}_{N-1} + \boldsymbol{R}_N\,, \tag{D.4}$$

where the matrices $\boldsymbol{M}_N$, $\boldsymbol{Q}_N$ and $\boldsymbol{R}_N$ are given by

$$\boldsymbol{M}_N = \begin{pmatrix} M_0(\mathscr{A}_N) \\ M_1(\mathscr{A}_N) \\ M_2(\mathscr{A}_N) \\ M_3(\mathscr{A}_N) \end{pmatrix}, \quad \boldsymbol{R}_N = \begin{pmatrix} M_0(A_N) \\ M_1(A_N) \\ M_2(A_N) \\ M_3(A_N) \end{pmatrix}, \tag{D.5a}$$

$$\boldsymbol{Q}_N = \begin{pmatrix} \alpha_N & 0 & 0 & 0 \\ \beta_N & \alpha_N & 0 & 0 \\ \gamma_N & 2\beta_N & \alpha_N & 0 \\ \delta_N & 3\gamma_N & 3\beta_N & \alpha_N \end{pmatrix} \tag{D.5b}$$

with

$$\begin{aligned} &\alpha_N = 1 - \frac{M_0(A_N)}{|\Omega|}, \quad \beta_N = -\frac{M_1(A_N)}{|\Omega|}\,, \\ &\gamma_N = -\frac{M_2(A_N)}{|\Omega|}, \quad \delta_N = -\frac{M_3(A_N)}{|\Omega|}\,. \end{aligned} \tag{D.6}$$

Repeating the steps that lead to (D.4) the configurational average over two grains A_N and A_{N-1} reads

$$\begin{aligned}\iint \boldsymbol{M}_N \frac{\mathrm{d}g_N\,\mathrm{d}g_{N-1}}{|\Omega|^2} &= \int \boldsymbol{Q}_N \boldsymbol{M}_{N-1}\frac{\mathrm{d}g_{N-1}}{|\Omega|} + \boldsymbol{R}_N \\ &= \boldsymbol{Q}_N \boldsymbol{Q}_{N-1}\boldsymbol{M}_{N-2} + \boldsymbol{M}_N \boldsymbol{R}_{N-1} + \boldsymbol{R}_N \end{aligned} \tag{D.7}$$

and the average over all possible configurations can be written as

$$\int \ldots \int \boldsymbol{M}_N \frac{\mathrm{d}g_N \ldots \mathrm{d}g_1}{|\Omega|^N} = \boldsymbol{Q}_N \ldots \boldsymbol{Q}_2 \boldsymbol{R}_1 + \boldsymbol{Q}_N \ldots \boldsymbol{Q}_3 \boldsymbol{R}_2 + \cdots + \boldsymbol{Q}_N \boldsymbol{R}_{N-1} + \boldsymbol{R}_N \,. \tag{D.8}$$

Exact result (D.8) is of little practical value unless we make additional assumptions about the properties of the individual grains. If all grains are identical we have $\boldsymbol{Q} = \boldsymbol{Q}_i$ and $\boldsymbol{R} = \boldsymbol{R}_i$ for $i = 1, \ldots, N$. Likewise if the distribution of size and shape of the grains is the same for all grains, averaging (D.8) over this distribution also yields $\boldsymbol{Q} = \overline{\boldsymbol{Q}_i}$ and $\boldsymbol{R} = \overline{\boldsymbol{R}_i}$ for all i. Evidently, the latter case contains the former. Hence averaging (D.8) over the size and shape of the grains yields

$$\langle \boldsymbol{M} \rangle_N \equiv \int \ldots \int \boldsymbol{M}_N \frac{\mathrm{d}g_N \ldots \mathrm{d}g_1}{|\Omega|^N} = (\boldsymbol{1} + \boldsymbol{Q} + \cdots + \boldsymbol{Q}^{N-1})\boldsymbol{R} \,. \tag{D.9}$$

By mathematical induction it can be shown that

$$\boldsymbol{1} + \boldsymbol{Q} + \cdots + \boldsymbol{Q}^{N-1} = \begin{pmatrix} a_{N-1} & 0 & 0 & 0 \\ b_{N-1} & a_{N-1} & 0 & 0 \\ c_{N-1} & 2b_{N-1} & a_{N-1} & 0 \\ d_{N-1} & 3c_{N-1} & 3b_{N-1} & a_{N-1} \end{pmatrix}, \tag{D.10}$$

where

$$\begin{aligned} a_{N-1} &= \frac{1-\alpha^N}{1-\alpha^N}, \quad b_{N-1} = \beta \frac{\partial a_{N-1}}{\partial \alpha}, \\ c_{N-1} &= \beta^2 \frac{\partial^2 a_{N-1}}{\partial \alpha^2} + \gamma \frac{\partial a_{N-1}}{\partial \alpha}, \\ d_{N-1} &= \beta^3 \frac{\partial^3 a_{N-1}}{\partial \alpha^3} + 3\beta\gamma \frac{\partial^2 a_{N-1}}{\partial \alpha^2} + \gamma \frac{\partial a_{N-1}}{\partial \alpha} \end{aligned} \tag{D.11}$$

and

$$\begin{aligned} \alpha &= 1 - \frac{m_0}{|\Omega|}, \quad \beta = -\frac{m_1}{|\Omega|}, \\ \gamma &= -\frac{m_2}{|\Omega|}, \quad \delta = -\frac{m_3}{|\Omega|} \end{aligned} \tag{D.12}$$

and where $m_v \equiv \overline{M_v(A_i)}$ denote the averages over size and shape of the Minkowski functional for a single grain A_i.

With expressions (D.10)–(D.12) we obtain from (D.9)

$$\langle M_0 \rangle_N = m_0 a_{N-1} \,, \tag{D.13a}$$

$$\langle M_1 \rangle_N = -\frac{m_1 m_0}{|\Omega|} \frac{\partial a_{N-1}}{\partial \alpha} + m_1 a_{N-1} \,, \tag{D.13b}$$

$$\langle M_2\rangle_N = \frac{m_1^2 m_0}{|\Omega|^2}\frac{\partial^2 a_{N-1}}{\partial\alpha^2} - \frac{1}{|\Omega|}(2m_1^2 + m_0 m_2)\frac{\partial a_{N-1}}{\partial\alpha} + m_2 a_{N-1}\ , \tag{D.13c}$$

$$\langle M_3\rangle_N = -\frac{m_1^3 m_0}{|\Omega|^3}\frac{\partial^3 a_{N-1}}{\partial\alpha^3} + \frac{m_1}{|\Omega|^2}(m_1^2 + 3m_2 m_0)\frac{\partial^2 a_{N-1}}{\partial\alpha^2} - \frac{1}{|\Omega|}(6m_1 m_2 + m_0 m_3)\frac{\partial a_{N-1}}{\partial\alpha} + m_3 a_{N-1}\ , \tag{D.13d}$$

where $\langle M_\nu\rangle_N$ denote the mean values of the Minkowski functionals of the ensemble with density ρ.

The expressions in (D.13) may be further simplified by putting

$$z \equiv (1-\alpha)a_{N-1} = 1 - \alpha^N\ . \tag{D.14}$$

We find

$$\frac{\partial z}{\partial\alpha} = (1-\alpha)\frac{\partial a_{N-1}}{\alpha} - a_{N-1} = -N\alpha^{N-1}\ , \tag{D.15a}$$

$$\frac{\partial^2 z}{\partial\alpha^2} = (1-\alpha)\frac{\partial^2 a_{N-1}}{\alpha^2} - 2\frac{\partial a_{N-1}}{\partial\alpha} = -N(N-1)\alpha^{N-2}\ , \tag{D.15b}$$

$$\frac{\partial^3 z}{\partial\alpha^3} = (1-\alpha)\frac{\partial^3 a_{N-1}}{\alpha^3} - 3\frac{\partial^2 a_{N-1}}{\partial\alpha^2} = -N(N-1)(N-2)\alpha^{N-3}\ . \tag{D.15c}$$

Substituting (D.14), (D.15) and $m_0/|\Omega| = 1-\alpha$, in (D.13) finally gives

$$\langle M_0\rangle_N = |\Omega|(1-\alpha^N)\ , \tag{D.16a}$$

$$\langle M_1\rangle_N = m_1 N\alpha^{N-1}\ , \tag{D.16b}$$

$$\langle M_2\rangle_N = -\frac{m_1^2}{|\Omega|}N(N-1)\alpha^{N-2} + m_2 N\alpha^{N-1}\ , \tag{D.16c}$$

$$\langle M_3\rangle_N = \frac{m_1^3}{|\Omega|^2}N(N-1)(N-2)\alpha^{N-3} - 3\frac{m_1 m_2}{|\Omega|}N(N-1)\alpha^{N-2} + m_3 N\alpha^{N-1}\ . \tag{D.16d}$$

In the bulk limit $N, \Omega\to\infty$ with $\rho = N/|\Omega|$ fixed, we have

$$\lim_{N\to\infty}\alpha^N = \lim_{N\to\infty}\left(1 - \frac{m_0}{|\Omega|}\right)^N = \mathrm{e}^{-\rho m_0} \tag{D.17}$$

and

$$\langle M_0/N\rangle_N = (1-\mathrm{e}^{-\rho m_0})/\rho\ , \tag{D.18a}$$

$$\langle M_1/N\rangle_N = m_1\mathrm{e}^{-\rho m_0}\ , \tag{D.18b}$$

$$\langle M_2/N\rangle_N = (m_2 - m_1^2\rho)\mathrm{e}^{-\rho m_0}\ , \tag{D.18c}$$

$$\langle M_3/N\rangle_N = (m_1^3\rho^2 - 3m_1 m_2\rho + m_3)\mathrm{e}^{-\rho m_0}\ . \tag{D.18d}$$

Note that the expressions in (D.18) are valid for any dimension d.

References

[1] P. Ball, The Self-Made Tapestry: Pattern Formation in Nature, Oxford University Press, Oxford, 1998. *
[2] S. Hyde, S. Andersson, K. Larsson, Z. Blum, T. Landh, S. Lidin, B.W. Ninham, The Language of Shape; The Role of Curvature in Condensed Matter: Physics, Chemistry and Biology, Elsevier, Amsterdam, 1997. *
[3] J.C. Russ, The Image Processing Handbook, CRC Press, Florida, 1995. *
[4] K.R. Castleman, Digital Image Processing, Prentice-Hall, Englewood Cliffs, 1996. *
[5] R.C. Gonzalez, R.E. Woods, Digital Image Processing, Addison-Wesley, Reading, MA, 1993. *
[6] A. Rosenfeld, A.C. Kak, Digital Picture Processing, Academic Press, New York, 1982. *
[7] C.R. Giardina, E.R. Dougherty, Morphological Methods in Image and Signal Processing, Prentice-Hall, Englewood Cliffs, 1988. ***
[8] H. Hadwiger, Vorlesungen über Inhalt, Oberfläche und Isoperimetrie, Springer, Berlin, 1957. ***
[9] L.A. Santaló, Integral Geometry and Geometric Probability, Addison-Wesley, Reading, MA, 1976. **
[10] D. Stoyan, W.S. Kendall, J. Mecke, Stochastic Geometry and its Applications, Akademie Verlag, Berlin, 1989. **
[11] K.R. Mecke, H. Wagner, Euler characteristic and related measures for random geometric sets, J. Stat. Phys. 64 (1991) 843–850. *
[12] K.R. Mecke, A morphological model for complex fluids, J. Phys.: Condens. Matter 8 (1996) 9663–9667.
[13] K.R. Mecke, Morphological thermodynamics of composite media, Fluid Phase Equilibria 150–151 (1998) 591–598.
[14] K.R. Mecke, Integral geometry in statistical physics, Int. J. Mod. Phys. B 12 (1998) 861–899. ***
[15] A.L. Mellot, The topology of large-scale structure in the universe, Phys. Rep. 193 (1990) 1–39.
[16] K.R. Mecke, T. Buchert, H. Wagner, Robust morphological measures for large-scale structure in the Universe, Astron. Astrophys. 288 (1994) 697–704.
[17] N.G. Makarenko, L.M. Karimova, A.G. Terekhov, A.V. Kardashev, Minkowksi functionals and comparison of discrete samples in seisomology, Phys. Solid Earth 36 (2000) 305–309.
[18] J.S. Kole, K. Michielsen, H. De Raedt, Morphological image analysis of quantum motion in billiards, Phys. Rev. E 63 (2001) 016201.
[19] C.N. Likos, K.R. Mecke, H. Wagner, Statistical morphology of random interfaces in microemulsions, J. Chem. Phys. 102 (1995) 9350–9361.
[20] K.R. Mecke, Morphological characterization of patterns in reaction–diffusion systems, Phys. Rev. E 53 (1996) 4794–4800.
[21] K.R. Mecke, V. Sofonea, Morphology of spinodal decomposition, Phys. Rev. E 56 (1997) R3761–R3764.
[22] V. Sofonea, K.R. Mecke, Morphological characterization of spinodal decomposition kinetics, Eur. Phys. J. B 8 (1999) 99–112.
[23] S. Herminghaus, K. Jacobs, K. Mecke, J. Bischof, A. Fery, M. Ibn-Elhaj, S. Schlagowski, Spinodal dewetting in liquid crystal and liquid metal films, Science 282 (1998) 916–919.
[24] K. Jacobs, S. Herminghaus, K.R. Mecke, Thin liquid polymer films rupture via defects, Langmuir 14 (1998) 965–969.
[25] G. Matheron, Random Sets and Integral Geometry, Wiley, New York, 1975. *
[26] J. Serra, Image Analysis and Mathemathical Morphology, Academic Press, London, 1982. *
[27] M. Gervautz, W. Purgathofer, A simple method for color quantization: Octree quantization, in: A.S. Glassner (Ed.), Graphics Gems, Academic Press, Boston, 1990.
[28] D.J. Taylor, B.D. Fabes, Laser processing of sol–gel coatings, J. Non-Cryst. Solids 147–148 (1992) 457–462.
[29] D.J. Shaw, T.A. King, Densification of sol–gel silica glass by laser irradiation, in: J.D. Mackenzie, D.R. Ulrich (Eds.), Sol–Gel Optics, Proceedings of SPIE, Vol. 1328, 1990, pp. 474–481.
[30] J.Th.M. De Hosson, D.H.J. Teeuw, Nano-ceramic coatings produced by laser treatment, Surf. Eng. 15 (1999) 235–241.
[31] J.Th.M. de Hosson, M. de Haas, D.H.J. Teeuw, High resolution scanning electron microscopy observations of nano-ceramics, in: D.G. Rickerby et al. (Eds.), Impact of Electron Scanning Probe Microscopy on Materials Research, Kluwer Academic Publishers, 1999, pp. 109–134.

[32] J.Th.M. De Hosson, Laser synthesis and properties of ceramic coatings, in: N.B. Dahotre, T.S. Sudarshan (Eds.), Intermetallic and Ceramic Coatings, Marcel Dekker, New York, 1999, pp. 307–441.
[33] D.H.J. Teeuw, M. de Haas, J.Th.M. De Hosson, Residual stress fields in sol–gel derived thin TiO_2 layers, J. Mater. Res. 14 (1999) 1896–1904.
[34] A.P. Gast, W.B. Russel, Simple ordering in complex fluids, Colloidal particles suspended in solution provide intriguing models for studying phase transitions, Phys. Today 51 (1998) 24–30.
[35] K. Michielsen, H. De Raedt, J.G.E.M. Fraaije, Morphological characterization of spatial patterns, Prog. Theor. Phys. 138 (Suppl.) (2000) 543–548.
[36] J. Klinowski, A.L. Mackay, H. Terrones, Curved surfaces in chemical structure, Philos. Trans. Roy. Soc. Lond. A 354 (1996) 1975–1987.
[37] H.G. von Schnering, R. Nesper, How nature adapts chemical structures to curved surfaces, Angew. Chem. 26 (1987) 1059–1080.
[38] A.L. Mackay, Equipotential surfaces in periodic charge distributions, Angew. Chem. Int. Edn. Engl. 27 (1988) 849–850.
[39] V. Luzzati, A. Tardieu, T. Gulik-Krzywicki, E. Rivas, F. Reiss-Husson, Structure of the cubic phases of lipid–water systems, Nature 220 (1968) 485–488.
[40] W. Longley, T.J. McIntosh, A bicontinuous tetrahedral structure in a liquid-crystalline lipid, Nature 304 (1983) 612–614.
[41] K. Larsson, Two cubic phases in monoolein-water system, Nature 304 (1983) 664–664.
[42] P. Mariani, V. Luzzati, H. Delacroix, Cubic phases of lipid-containing systems, J. Mol. Biol. 204 (1999) 165–189.
[43] A. Ciach, Phase diagram and structure of the bicontinuous phase in a three-dimensional lattice model for oil–water–surfactant models, J. Chem. Phys. 96 (1992) 1399–1408.
[44] E.L. Thomas, D.B. Alward, D.J. Kinning, D.C. Martin, D.L. Handlin Jr, L.J. Fetters, Ordered bicontinuous double-diamond structure of star block copolymers: a new equilibrium microdomain morphology, Macromolecules 19 (1986) 2197–2202.
[45] H. Hasegawa, H. Tanaka, K. Yamasaki, T. Hashimoto, Bicontinuous microdomain morphology of block copolymers. 1. Tetrapod-network structure of polystyrene-polyisopropene diblock polymers, Macromolecules 20 (1987) 1651–1662.
[46] D.M. Anderson, E.L. Thomas, Microdomain morphology of star copolymers in the strong-segregation limit, Macromolecules 21 (1988) 3221–3230.
[47] E.L. Thomas, D.M. Anderson, C.S. Henkee, D. Hoffman, Periodic area-minimizing surfaces in block copolymers, Nature 334 (1988) 598–601.
[48] Y. Mogi, K. Mori, Y. Matsushita, I. Noda, Tricontinuous morphology of triblock copolymers of the ABC type, Macromolecules 25 (1992) 5412–5415.
[49] Y. Matsushita, M. Tamura, I. Noda, Tricontinuous double-diamond structure formed by a styrene-isopropene-2-vinylpyridine triblock copolymer, Macromolecules 27 (1994) 3680–3682.
[50] M.F. Schulz, F.S. Bates, K. Almdal, K. Mortensen, Epitaxial relationship for hexagonal-to-cubic phase transition in a block copolymer mixture, Phys. Rev. Lett. 73 (1994) 86–89.
[51] D.A. Hajduk, P.E. Harper, S.M. Gruner, C.C. Honeker, G. Kim, E.L. Thomas, L.J. Fetters, The gyroid: a new equilibrium morphology in weakly segregated diblock copolymers, Macromolecules 27 (1994) 4063–4075.
[52] D.A. Hajduk, P.E. Harper, S.M. Gruner, C.C. Honeker, E.L. Thomas, L.J. Fetters, A reevaluation of bicontinuous cubic phases in starblock copolymers, Macromolecules 28 (1995) 2570–2573.
[53] H. Jinnai, T. Hashimoto, D. Lee, S.-H. Chen, Morphological characterization of bicontinuous phase-separated polymer blends and one-phase microemulsions, Macromolecules 30 (1997) 130–136.
[54] S. Sakurai, H. Irie, H. Umeda, S. Nomura, H.H. Lee, J.K. Kim, Gyroid structures and morphological control in binary blends on polystyrene-block-polyisopropene diblock copolymers, Macromolecules 31 (1998) 336–343.
[55] M.W. Hamersky, M.A. Hillmeyer, M. Tirrell, F.S. Bates, T.P. Lodge, E.D. von Meerwall, Block copolymer self-diffusion in the gyroid and cylinder morphologies, Macromolecules 31 (1998) 5363–5370.
[56] M.E. Vigild, K. Almdal, K. Mortensen, I.W. Hamley, J.P.A. Fairclough, A.J. Ryan, Transformations to and from the gyroid phase in a diblock copolymer, Macromolecules 31 (1998) 5702–5716.

[57] F.S. Bates, G.H. Fredrickson, Block copolymers-designer soft materials. Advances in synthetic chemistry and statistical theory provide unparalleled control over molecular scale morphology in this class of macromolecules, Phys. Today 52 (1999) 32–38.
[58] G. Donnay, D.L. Pawson, X-ray diffraction studies of echinoderm plates, Science 166 (1969) 1147–1150.
[59] H.-U. Nissen, Crystal orientation and plate structure in echinoid skeletal units, Science 166 (1969) 1150–1152.
[60] K. Larsson, Cubic lipid–water phases: structures and biomembrane aspects, J. Phys. Chem. 93 (1989) 7304–7314.
[61] W. Fischer, E. Koch, On 3-periodic minimal surfaces, Z. Kristallogr. 179 (1987) 31–52.
[62] K. Grosse-Brauckmann, On gyroid interfaces, J. Colloid Interface Sci. 187 (1997) 418–428. *
[63] H.A. Schwarz, Gesammelte Mathematische Abhandlungen, Springer, Berlin, 1890.
[64] A.H. Schoen, Infinite periodic minimal surfaces without self-intersections, NASA Technical NOTE No. D-5541, 1970.
[65] A.L. Mackay, Crystallographic surfaces, Proc. Roy. Soc. Lond. A 442 (1993) 47–59.
[66] C.A. Lambert, L.H. Radzilowski, E.L. Thomas, Triply periodic level surfaces as models for cubic tricontinuous block copolymer morphologies, Philos. Trans. Roy. Soc. Lond. A 354 (1996) 2009–2023.
[67] A. Ciach, R. Hołyst, Periodic surfaces and cubic phases in mixtures of oil, water, and surfactant, J. Chem. Phys. 110 (1999) 3207–3214.
[68] W.T. Góźdź, R. Hołyst, Triply periodic surfaces and multiply continuous structures from the Landau model of microemulsions, Phys. Rev. E 54 (1996) 5012–5027.
[69] S.T. Hyde, Swelling and structure. Analysis of the topology and geometry of lamellar and sponge lyotropic mesophases, Langmuir 13 (1997) 842–851.
[70] Y. Nishikawa, H. Jinnai, T. Koga, T. Hashimoto, S.T. Hyde, Measurements of interfacial curvatures of bicontinuous structure from three-dimensional digital images. 1. A parallel surface method, Langmuir 14 (1998) 1242–1249.
[71] W. Fischer, E. Koch, Genera of minimal balance surfaces, Acta Crystallogr. A 45 (1989) 726–732. *
[72] P.S. Aleksandrov, Combinatorial topology, Vol. 1, Graylock, Rochester NY, 1956.
[73] P. Davy, Projected thick sections through multi-dimensional particle aggregates, J. Appl. Probab. 13 (1976) 714–722.
[74] H.G. Kellerer, Minkowski functionals of Poisson processes, Z. Wahr. Verw. Gebiete 67 (1984) 63–84.
[75] K. Michielsen, H. De Raedt, Morphological Image Analysis, Comput. Phys. Commun. 132 (2000) 94–103.
[76] S.R. Broadbent, J.M. Hammersley, Percolation processes, Proc. Cambridge Phil. Soc. 53 (1957) 629–641.
[77] D. Stauffer, A. Aharony, Introduction to Percolation Theory, Taylor&Francis, London, 1991. *
[78] H. Kesten, Percolation Theory for Mathematicians, Birkhäuser, Boston, MA, 1982.
[79] G. Deutscher, R. Zallen, J. Adler, Percolation Structures and Processes, A. Hilger, Bristol, 1983.
[80] M. Sahimi, Applications of Percolation Theory, Taylor&Francis, London, 1994.
[81] G. Grimmett, Percolation, Springer, Berlin, 1999.
[82] J.M. Hammersley, Percolation processes. Lower bounds for the critical probability, Ann. Math. Stat. 28 (1957) 790–795.
[83] T.E. Harris, A lower bound for the critical probability in a certain percolation process, Proc. Cambridge Philos. Soc. 56 (1960) 13–20.
[84] B. Tóth, A lower bound for the critical probability of the square lattice site percolation, Z. Wahr. Verw. Gebiete 69 (1985) 19–22.
[85] S.A. Zuev, Bounds for the percolation threshold for a square lattice, Theor. Probab. Appl. 32 (1987) 551–553.
[86] M.V. Menshikov, K.D. Pelikh, Percolation with several defect types. An estimate of critical probability for a square lattice, Math Notes Acad. Sci. USSR 46 (1989) 778–785.
[87] J.C. Wierman, Substitution method critical probability bounds for the square lattice site percolation model, Combin. Probab. Comput. 4 (1995) 181–188.
[88] J. van den Berg, A. Ermakov, A new lower bound for the critical probability of site percolation on the square lattice, Random Structures and Algorithms 8 (1996) 199–212.
[89] R.M. Ziff, B. Sapoval, The efficient determination of the percolation threshold by a frontier-generating walk in a gradient, J. Phys. A 19 (1986) L1169–L1172.
[90] R.M. Ziff, Spanning probability in 2D percolation, Phys. Rev. Lett. 69 (1992) 2670–2673.

[91] M.F. Sykes, J.M. Essam, Exact critical percolation probabilities for site and bond percolation problems in two dimensions, J. Math. Phys. 5 (1964) 1117–1127.
[92] H. Kesten, The critical probability of bond percolation on the square lattice equals 1/2, Commun. Math. Phys. 74 (1980) 41–59.
[93] J.C. Wierman, Bond percolation on honeycomb and triangular lattices, Adv. Appl. Probab. 13 (1981) 293–313.
[94] B.L. Okun, Euler characteristic in percolation theory, J. Stat. Phys. 59 (1990) 523–527.
[95] H. Tomita, C. Murakami, Percolation pattern in continuous media and its topology, in: R. Takaki (Ed.), Research of Pattern Formation, KTK Scientific Publishers, Tokyo, 1994, pp. 197–203.
[96] A. Aksimentiev, R. Hołyst, K. Moorthi, Kinetics of the droplet formation at the early and intermediate stages of the spinodal decomposition in homopolymer blends, Macromol. Theory Simul. 9 (2000) 661–674.
[97] F.S. Bates, G.H. Fredrickson, Block copolymer thermodynamics: theory and experiment, Annu. Rev. Phys. Chem. 41 (1990) 525–557.
[98] S.-H. Shen, D. Lee, S.-L. Chang, Visualization of 3D microstructure of bicontinuous microemulsions by combined SANS experiments and simulations, J. Mol. Struct. 296 (1993) 259–264.
[99] A. Aksimentiev, K. Moorthi, R. Hołyst, Scaling properties of the morphological measures at the early and intermediate stages of the spinodal decomposition in homopolymer blends, J. Chem. Phys. 112 (2000) 6049–6062.
[100] J.G.E.M. Fraaije, B.A.C. van Vlimmeren, N.M. Maurits, M. Postma, O.A. Evers, C. Hoffmann, P. Altevogt, G. Goldbeck-Wood, The dynamic mean-field density functional method and its application to the mesoscopic dynamics of quenched block copolymer melts, J. Chem. Phys. 106 (1997) 4260–4269.
[101] P. Alexandridis, U. Olsson, B. Lindmann, Self-assembly of amphiphilic block copolymers: the $(EO)_{13}(PO)_{30}(EO)_{13}$-water-p-xylene system, Macromolecules 28 (1995) 7700–7710.
[102] B.A.C. van Vlimmeren, N.M. Maurits, A.V. Zvelindovsky, G.J.A. Sevink, J.G.E.M. Fraaije, Simulation of 3D mesoscale structure formation in concentrated aqueous solution of the triblock polymer surfactants $(\text{ethylene oxide})_{13}(\text{propylene cxide})_{30}(\text{ethylene oxide})_{13}$ and $(\text{ethylene oxide})_{19}(\text{propylene oxide})_{33}(\text{ethylene oxide})_{19}$, Application of dynamic mean-field density functional theory, Macromolecules 32 (1999) 646–656.
[103] H.E. Stanley, Introduction to Phase Transitions and Critical Phenomena, Clarendon Press, Oxford, 1971.
[104] M.P. Allen, D.J. Tildesley, Computer Simulation of Liquids, Oxford University Press, Oxford, 1993.
[105] K. Michielsen, H. De Raedt, T. Kawakatsu, Morphological image analysis, in: D.P. Landau et al. (Eds.), Computer Simulation Studies in Condensed-Matter Physics XIII, Springer Proceedings in Physics, Springer, Berlin, in press.
[106] T. Kawakatsu, R. Hasegawa, M. Doi, Dynamic density functional approach to phase separation dynamics of polymer systems, Int. J. Mod. Phys. C 10 (2000) 1531–1540.
[107] J.G.E.M. Fraaije, Dynamic density functional theory for microphase separation kinetics of block copolymer melts, J. Chem. Phys. 99 (1993) 9202–9212.
[108] R. Hasegawa, M. Doi, Adsorption dynamics. Extension of self-consistent field theory to dynamical problems, Macromolecules 30 (1997) 3086–3089.
[109] T. Kawakatsu, Effects of changes in the chain conformation on the kinetics of order-disorder transitions in block-copolymer melts, Phys. Rev. E 56 (1997) 3240–3250.